Fermilab FERMILAB-THESIS-2000-33

CHARGED K/π PRODUCTION RATIOS WITH Σ, π AND PROTONS ON CARBON AND COPPER TARGETS

by

Suat Özkorucuklu

An Abstract

Of a thesis submitted in partial fulfillment of the
requirements for the Doctor of Philosophy
degree in Physics in the
Graduate College of The
University of Iowa

July 2001

Thesis supervisors: Professor Yasar Onel
Professor Edward McCliment

ABSTRACT

We have measured charged K/π production ratios using the data taken by the SELEX (E781) experiment during the 1996-97 fixed target run at Fermi National Accelerator Laboratory. The results of this study is important for resolving uncertainties in determining the neutrino beam fluxes since neutrino beams are produced mostly by charged kaons and pions decays. Additionally, SELEX had three different type of beam particles (p, π, Σ) and two different productions targets (C, Cu) which make it possible to study production differences by different beam particles and the leading particle effect in production of kaons and pions, and A dependence.

Abstract approved: _____
Thesis supervisor

_____
Title and department

_____
Date

_____
Thesis supervisor

_____
Title and department

_____
Date

Graduate College
The University of Iowa
Iowa City, Iowa

CERTIFICATE OF APPROVAL

PH.D. THESIS

This is to certify that the Ph.D. thesis of

Suat Özkorucuklu

has been approved by the Examining Committee for the thesis requirement for the Doctor of Philosophy degree in Physics at the July 2001 graduation.

Thesis committee: _____
Thesis supervisor

_____
Thesis supervisor

_____
Member

_____
Member

_____
Member

CHARGED K/π PRODUCTION RATIOS WITH Σ, π AND PROTONS ON CARBON AND COPPER TARGETS

by

Suat Özkorucuklu

A thesis submitted in partial fulfillment of the
requirements for the Doctor of Philosophy
degree in Physics in the
Graduate College of The
University of Iowa

July 2001

Thesis supervisors: Professor Yasar Onel
Professor Edward McCliment

To my kids Hami Suha and Taha Furkan Özkorucuklu

ACKNOWLEDGEMENTS

I would like to thank to my advisors Prof. Dr. Yasar Önel and Prof. Dr. Edward McCliment for their guidance and support during the my graduate career. Special thanks to Dr. Peter Cooper for his support and guidance throughout my analysis and Dr. Soon Yung Jun for his constant interest on my studies. I would like to thank to Dr. Aldo Penzo all the valuable discussions we had. Also, I thank the SELEX(E781) collaborators who helped to make this experiment successful and my friends and colleagues at the University of Iowa, especially Dr. Kenneth Day Nelson for his endless encouragements. Finally, I thank Süleyman Demirel University for the scholarship they provided for my Ph.D Studies and my family for supporting me every step.

TABLE OF CONTENTS

Page

LIST OF TABLES v

LIST OF FIGURES vi

CHAPTER

I INTRODUCTION 1

1.1 Motivations 1
1.1.1 Neutrino Beam Flux 1
1.1.2 Fragmentation and Leading Particle Effect 2
1.1.3 A Dependence 4

II THE SELEX EXPERIMENT 5

2.1 The Physics Programs in SELEX 5
2.1.1 Charm Physics Program 5
2.1.2 Non-Charm Physics Program 6
2.2 Experimental Setup 7
2.2.1 The Beam Spectrometer 10
2.2.2 The Vertex Spectrometer 16
2.2.3 The M1 Spectrometer 17
2.2.4 The M2 Spectrometer 22
2.2.5 The M3 Spectrometer 26

III THE TRIGGER, DATA ACQUISITION AND OFFLINE ANALYSIS 29

3.1 The Trigger System 29
3.1.1 The Hardware Trigger Levels 31
3.1.2 The Software Trigger 33
3.1.3 Trigger Synchronization 34
3.1.4 The Trigger Types 34
3.2 The Data Acquisition System 35
3.3 The Off-line Data Processing 37

IV DATA COLLECTION AND ANALYSIS 43

4.1 The Data Collection 43
4.2 The Analysis Steps 44
4.3 The Correction to Data Sample and Error Analysis 49
4.3.1 Particle Identification Corrections 49

4.3.2 Acceptance Corrections 54
4.3.3 Corrections for the Particle Decays 57
4.3.4 Corrections for the Target Size 58
4.4 Systematic Error Analysis 58
4.4.1 Systematic Error in the Efficiency and Acceptance Correction 59
4.4.2 Systematic Error in Momentum Determination 59
4.4.3 Systematic Error in Beam Particle Identification 59
4.4.4 Systematic Error in Binning 60
4.5 Charged Particle Ratios for Σ^-, π^- and p Beams 60

V CONCLUSION 73

A THE M1 AND M3 MULTI-WIRE PROPORTIONAL CHAMBERS . 83
1.1 The M1 Multi-Wire Proportional Chambers (M1WPC) 83
1.2 The M3 Multi-Wire Proportional Chambers (M3WPC) 88
1.3 The Electronics for the M1PWCs and M3PWCs 89
1.4 Efficiency of the M1PWC and M3PWC 93

REFERENCES 97

LIST OF TABLES

Table		Page
1	Quark Content of the Beam and Secondary Particles	3
2	The Charm Target Properties	16
3	The Trigger Primitives	31
4	A Sample Initial Plane List File	38
5	A Sample RECON Package Table	40
6	A Sample SOAP Control File	41
7	A Sample KUMAC File Used for Analysis	42
8	The Modified Reconstruction (RECON) List	50
9	The Contamination of the Beam Particles	60
10	Comparison of Experiments	74
11	Comparison of π^+/π^- Ratios for Different Beam Particles	75
12	Comparison of K^+/K^- Ratios for Different Beam Particles	78
13	Comparison of $\overline{p}/p$ Ratios for Different Beam Particles	78

LIST OF FIGURES

Figure		Page
1	The Layout of SELEX Experiment	9
2	The Layout of the Beam and Vertex Spectrometers	11
3	The Hyperon Magnet Schematics	13
4	Σ^-/π^- Separation with the Beam TRD	14
5	The Layout Inside the RF Cage	15
6	The Momentum Distribution of the Positive and Negative Beams	15
7	The Primary and Secondary Vertex Resolutions and Targets	18
8	The M1 Spectrometer Layout	19
9	The M1PWC Anode Wire Orientations	20
10	The M2 Spectrometer Layout	23
11	ETRD Separation for π (Left) and Both π and e (Right)	24
12	Demonstration of the Cherenkov Light in the RICH	25
13	A Single RICH Event Display	27
14	RICH Ring Radius and Difference Versus Momentum	28
15	The Schematics of SELEX Trigger System	30
16	The Detectors Used in T_1 Trigger Levels	32
17	Schematic View of the SELEX Data Acquisition System	36
18	Stored Beam Track Ntuple Variables	46
19	Stored Secondary Track Ntuple Variables	47
20	Stored Particle Identification and Track Type Ntuple Variables	48
21	RECON Constructed Masses Without RICH Identification	51

22 RICH Particle Identification for $\Lambda^0 \to p\pi^-$ 53
23 RICH Particle Identification for $K_s \to \pi^+\pi^-$ 55
24 RICH Particle Identification for $\Phi \to K^+K^-$ 56
25 Acceptance Correction for Positive and Negative Tracks 57
26 π^+/π^-, K^+/K^- and $\overline{p}/p$ Ratios Versus Momentum for Σ^- Beam 61
27 π^+/π^-, K^+/K^- and $\overline{p}/p$ Ratios Versus x_F for Σ^- Beam 62
28 π^+/π^-, K^+/K^- and $\overline{p}/p$ Ratios Versus p_t^2 for Σ^- Beam 63
29 $K^\pm/\pi^\pm$ Versus x_F and p_t^2 for Σ^- Beam 64
30 π^+/π^-, K^+/K^- and $\overline{p}/p$ Ratios Versus Momentum for π^- Beam 65
31 π^+/π^-, K^+/K^- and $\overline{p}/p$ Ratios Versus x_F for π^- Beam 66
32 π^+/π^-, K^+/K^- and $\overline{p}/p$ Ratios Versus p_t^2 for π^- Beam 67
33 $K^\pm/\pi^\pm$ Versus x_F and p_t^2 for π^- Beam 68
34 π^+/π^-, K^+/K^- and $\overline{p}/p$ Ratios Versus Momentum for p Beam 69
35 π^+/π^-, K^+/K^- and $\overline{p}/p$ Ratios Versus x_F for p Beam 70
36 π^+/π^-, K^+/K^- and $\overline{p}/p$ Ratios Versus p_t^2 for p Beam 71
37 $K^\pm/\pi^\pm$ Versus x_F and p_t^2 for p Beam 72
38 Comparison of Σ^- and π^- Beams 76
39 Comparison of Σ^- and p Beams 77
40 π^+/π^- and K^+/K^- Ratios versus x_F for Σ^- Beam 80
41 π^+/π^- and K^+/K^- Ratios versus x_F for π^- Beam 81
42 Comparison of C and Cu Targets 82
43 The Schematics View the MWPC 84
44 The Plane Orientation of M1PWC and M3PWCs Planes. 86
45 The Mylar Ctrips(garlands) in Multiwire Proportional Chamber. 87
46 The Block Diagram of the PWC Readout System 92

47 Plateau Curves Obtained With a Sr^{90} Source for M1PWC 95

CHAPTER I
INTRODUCTION

1.1 Motivations

We have measured charged particle production ratios in a wide momentum range using the data sample from the SELEX (Segmented Large x_F Baryon Spectrometer) experiment. The SELEX spectrometer had very good mass resolution based on precise tracking [1] and extensive particle identification. SELEX used different types of particle detectors for tracking including high resolution silicon strip detectors, multi-wire proportional chambers and drift chambers. The particle identification was done with transition radiation detectors for beam particle tagging, a ring imaging Cherenkov counter for identifying e, π, K, p, an electron transition radiation detectors for separating electrons from hadrons and three lead glass detectors to identify photons and electrons. These made SELEX an excellent choice for performing charged particle production ratio measurements which is important for the following types of studies.

1.1.1 Neutrino Beam Flux

Measurement of the neutrino cross section requires knowledge of the incident neutrino beam flux because the neutrino beam results from decay of charged pions and kaons. The pions and kaons are produced by a primary beam of protons that impinges on a beryllium target and decay principally via two-body processes [2] :

$$\pi^{\pm} \rightarrow \mu^{\pm} + \nu_{\mu}(\overline{\nu_{\mu}}),$$
$$K^{\pm} \rightarrow \mu^{\pm} + \nu_{\mu}(\overline{\nu_{\mu}}).$$

In general the momentum spectrum of pions and kaons produced by proton-nucleus collisions is broad and would result in a wide range of neutrino energies. In order to obtain neutrinos of well defined energies, it is necessary to have a mono-energetic secondary beam.

Only pions and kaons contribute to the neutrino flux, and decay probabilities and neutrino energy spectra differ for the two. To know the neutrino flux, it is necessary to measure the fraction of pions and kaons in the beam along with total secondary beam intensity.

The relative number of the electron neutrinos (ν_e) and (ν_μ) is determined by the K^+/π^+ ratio. More precisely, in ν_μ beams $\nu_\mu \rightarrow \nu_e$ oscillations are usually investigated by searching for an excess of the ν_e induced events with respect to the rate expected from ν_e contamination in the beam. The present uncertainty in the K/π production ratio is one of the dominant sources of the systematic error on $\nu_\mu \rightarrow \nu_e$ oscillation searches.

There are several experiments for this kind of measurement with a proton beam on a Be target [3, 4, 5]. However, SELEX can study not only production with protons, but also pion and sigma beams as well and on two different targets, Carbon and Copper.

1.1.2 Fragmentation and Leading Particle Effect

Colored quarks and gluons can be regarded as free during the hard collisions, but subsequently color forces will organize them into colorless hadrons; this is called "fragmentation or hadronization". Typically it involves the creation of additional quark-anti quark pairs by the color force field. Fragmentation is governed by the soft non-perturbative process that cannot be calculated from scratch. In the past few years, there has been much activity, particularly in trying to explain the longitudinal

momentum x_F distribution of fast hadrons at low p_t^2 in terms of the quark structure and fragmentation functions. These efforts have resulted in a variety of different models, such as the quark fragmentation model [6] and the quark recombination model [7]. Since SELEX had three different particles in the beam and two different types of target, it is possible to study the difference in hadronization with these beam particles.

Another outcome of having Σ, π and p beams is that one can study the leading particle effect, an enhancement that is observed when a hadron shares the same type of quark with the incoming beam that produces it. We should see an enhancement in production of π^- over π^+ with Σ^- beam so the ratio of π^+/π^- should be less then 1 and should decrease with higher momentum. Similarly, K^+/K^- production ratio with Σ^- beam should have a similar behavior. Table 1 shows the quark content of the beam and the secondary particles and the shared quark between them. The leading particle effect in the charged particle production ratios should be observed for entries in the table that share a quark with the incoming beam.

	Secondary Particles			
Beam	π^- $(\overline{u}d)$	K^- $(\overline{u}s)$	π^+ $(u\overline{d})$	K^+ $(u\overline{s})$
π^- $(\overline{u}d)$	$\overline{u}d$	$\overline{u}$	-	-
Σ^- (dds)	d	s	-	-
p (uud)	d	-	u	u

Table 1: Quark Content of the Beam and Secondary Particles

1.1.3 A Dependence

The effects of the atomic weight (A) of a heavy nucleus on the production of particles at high energies are referred to as "A dependence" and the experimental study of particle production in p-A collisions probes the propagation of hadrons through nuclear matter. By studying the A dependence one can obtain information about the time development and early formation of those states. The most common functional form used to express the A dependence of a cross section is a simple power law $\sigma(A) = A^{\alpha}\sigma(A = 1)$ [8].

The charged particle production ratios are also crucial to the experimental search for fundamental new physics such as the formation of quark and gluon matter in the high density overlap region in relativistic heavy ion collisions [9].

The SELEX experiment had two different types of production targets, which allowed us to study of A dependence.

CHAPTER II
THE SELEX EXPERIMENT

SELEX (Segmented Large x_F Baryon Spectrometer) was proposed in 1984 as a third generation fixed target experiment [10]. It was designed as a multi-stage spectrometer with high acceptance for forward interactions and decays. It took data in the 1996-97 fixed target run period with 600 GeV/c Σ^-,π^- and 540 GeV/c proton beams. In this chapter we will briefly give an overview of the physics programs of the experiment followed by an overview the SELEX apparatus setup.

2.1 The Physics Programs in SELEX

The main goal of SELEX was to obtain a large sample of charm baryon decay using a variety of incident beam particles and targets. However, with the setup of SELEX, it was possible to study non-charm physics topics. Thus, the physics program of the SELEX experiment can be categorized into two main areas: charm and non-charm physics programs. These programs will be briefly explained in the following section.

2.1.1 Charm Physics Program

Many of the baryons in the second level of the SU(4) multiplets have been observed, but are not well measured. A comparison of meson and baryon spectroscopy will lead to a deeper understanding of the heavy charm quarks influence on the excitation spectra, thus testing the predictions of the Heavy Quark Effective Theory (HQET). The widths of excited states are needed as input to the HQET as well as the mass splitting of states; however,there is little experimental data available [11].

Production of heavy quarks can be described by the perturbative QCD, but hadronization of heavy quarks is a non-perturbative process and one needs experimental input to test theoretical models. The SELEX experiment investigated charm hadroproduction using three different beam particles: Σ^-, π^- and p, which made the SELEX a unique experiment. The experiment was designed to detect decays in the wide momentum range ($x_F > 0.1$ to 1.0), where x_F is approximately the fraction of the beam momentum carried by the charm particle. The study of the large x_F region is especially valuable, because that is the region where charm and anti-charm particle production differs the most [12]. The SELEX experiment also investigated the x_F and p_t^2 distributions of charm and anti-charm production asymmetries [12, 13].

Having a large sample of charm decays allowed SELEX to do precision measurements of charm lifetimes [14]. For control of systematic errors it is important that the lifetimes of all stable charm particles be measured in the same apparatus. These lifetimes provide a valuable input to test the Heavy Quark Expansion calculations where the decay rate is expanded as a power of series in terms of $(1/M_Q)^n$ (M_Q is the mass of heavy quark) [15].

Another important topic was to study of new decay modes and their relative branching ratios. Theoretical calculation of branching ratios of explicit decays of heavy quarks is still one of the most challenging areas of hadron physics. The SELEX experiment was the first experiment to observe the Cabibbo suppressed decay $\Xi_c^+ \to pK^-\pi^+$ [16].

2.1.2 Non-Charm Physics Program

The hadronic total cross section is one of the most fundamental measurements of the strength of hadronic interactions. SELEX measured Σ^- and π^- total cross sections on beryllium, copper, carbon and polyethylene targets and this was the

highest energy Σ^--p total cross section measurement [17].

The charge radius provides information about the internal structure of hadrons. This measurement is important to verify models which describe confinement of quarks inside the hadron. Different theoretical calculations of charge radii give quite different answers and experimental input can clarify the situation [18]. Charge radii of π^-, Σ^-, p were measured in the SELEX experiment by studying π^--e [19] Σ^--e [20] and p-e [21] scattering.

Hadronization is expected to play a major role in hyperon polarizations where an unpolarized proton beam incident on an unpolarized target produces polarized hyperons. SELEX measured production polarization of Σ^+ [22] and Λ^0 [23] as a function of x_F and p_t^2.

The charged particle production ratios were also investigated in the SELEX experiment. This study was motivated for reasons explained in Section 1.1.

2.2 Experimental Setup

SELEX was a five stage spectrometer and located in the Proton Center (PC) at Fermi National Accelerator Laboratory. Four dipole magnets (Hyperon, M1, M2, and M3 magnets) defined the five spectrometers, and they were called the Beam, Vertex, M1, M2 and M3 spectrometers. For this analysis, only some of these detectors were necessary: the beam silicon strip detectors for beam particle tracking and momentum calculation, and beam transition radiation detector for identification of the beam particles. The vertex silicon strip detectors were used for primary and secondary vertex identification and the large area silicon strip detectors, the M1 and M2 multi-wire proportional chambers were used for tracking of charged particles. Particle identification was done using the ring imaging Cherenkov counter and electron radiation transition detector.

Each spectrometer, except for the Vertex spectrometer, contained a bending magnet and the associated tracking and particle identification detectors. The layout of the experiment is shown in Figure 1 where the hyperon beam came from the left. The beam spectrometer was upstream and the vertex spectrometer was downstream of the charm targets, respectively. The M1- low momentum spectrometer was placed after the M1 magnet, the M2- high momentum spectrometer was placed after the M2 magnet and the hyperon decay spectrometer was placed after the M3 magnet.

The origin of the SELEX coordinate system was the middle of the downstream surface of the most downstream target. The z-axis is along the beam direction, the y-axis is vertically up and the x-axis completes a right-handed coordinate system. Most detectors measured tracks in x, y projections, or in u, v projections, which form some angle with respect to x, y axis.

The particle tracking was done with silicon strip detectors, multi-wire proportional chambers, drift chambers, and 3 analyzing magnets. The magnetic fields for each magnet were measured with a flip-coil apparatus that determined B_x, B_y and B_z components on a 1-inch grid with a precision of 0.1%. These maps were used to propagate the particle tracks inside the magnets and thus determined their momenta.

The beam silicon strip detector planes with hit resolution $\sigma \sim 6\,\mu$m were used to measure beam track parameters. The vertex silicon strip detector was the heart of the SELEX tracking system. The vertex silicon strip detector was capable of $4\,\mu$m transverse position resolution at 600 GeV/c and the vertex separation L between primary and secondary vertices was measured with precision $\sigma_L \approx 0.5$mm.

The downstream tracking system included 26 multi-wire proportional wire chamber planes with hit spatial resolution $\sigma \sim 0.6 - 1\,$mm. It also included three vector

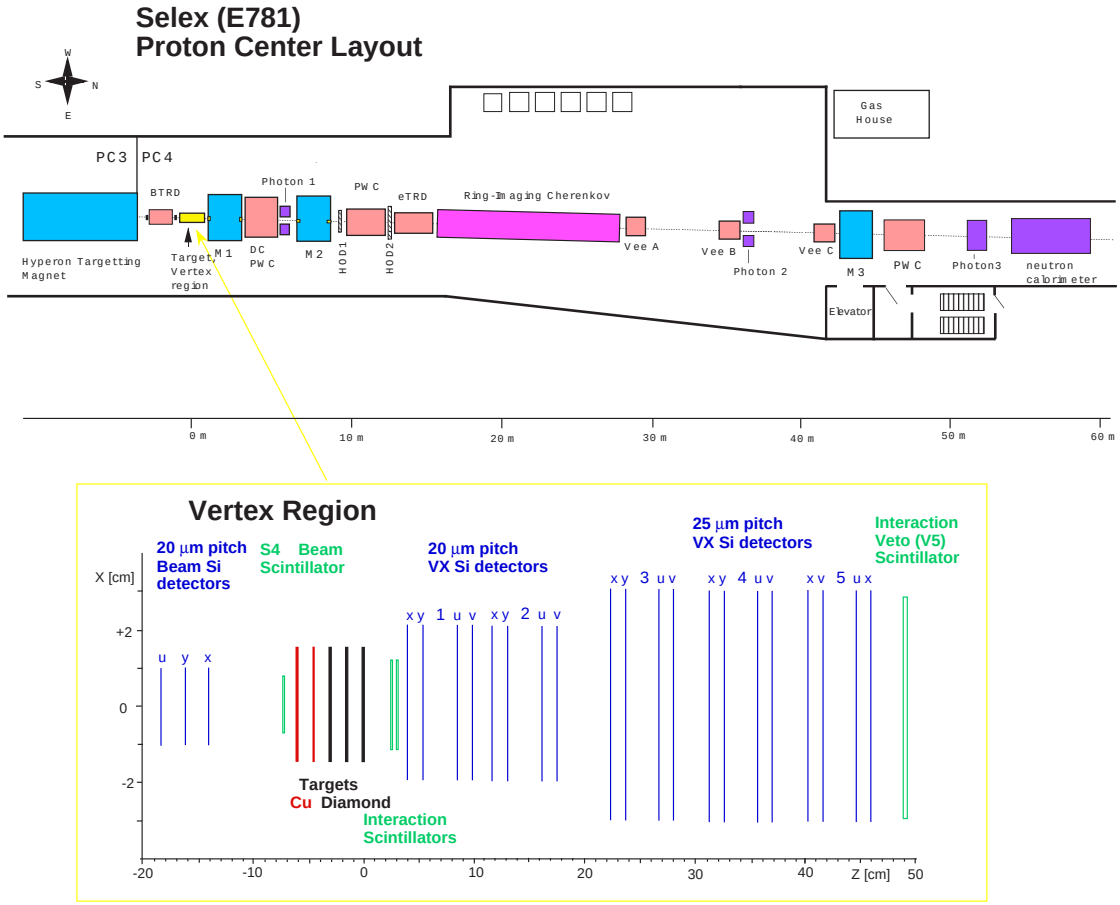

Figure 1: The Layout of SELEX Experiment

drift chambers each having 8 sensitive planes with hit resolution $\sigma \sim 100\,\mu$m. Finally, there were 18 large area silicon strip detectors with hit resolution $\sigma \sim 14\,\mu$m to measure very high-momentum tracks.

The SELEX particle identification system included: the beam transition radiation detector to identify the beam particles ($\Sigma^-/\pi^-, p/\pi^+$), and the ring imaging Cherenkov counter to identify the secondary particles such as electrons, muons, pions, kaons, protons and even hyperons, the electron transition radiation detector to separate electrons from the hadrons, and three lead glass detectors to identify and measure the energy of the photons and electrons. The main particle identification detector used for this study was the ring imaging Cherenkov counter and it was capable of K/π separation up to 165 GeV/c and K/p separation up to 320 GeV/c.

We will discuss the 5 spectrometer in some details in the following sections.

2.2.1 The Beam Spectrometer

The Beam Spectrometer consisted of the hyperon production target [24], the hyperon production magnet [25], scintillator counters, the beam transition radiation detector (BTRD) [26], the beam silicon strip detectors (BSSD) [27], and the hardware scatter trigger detector (HST) [28]. The layout of the beam spectrometer is shown in Figure 2.

The proton beam came from the left and hit the hyperon production target just inside the aperture of the Hyperon magnet. The momentum selected hyperons pass through the the Hyperon magnet and enter the beam spectrometer. The first detector in the beam spectrometer was the first station of a hardware scatter trigger silicon detector (HST). After passing the first station of HST, the beam passed through the beam transition radiation detector which distinguished pions from baryons. Downstream of the beam transition radiation detector the beam passed through the second

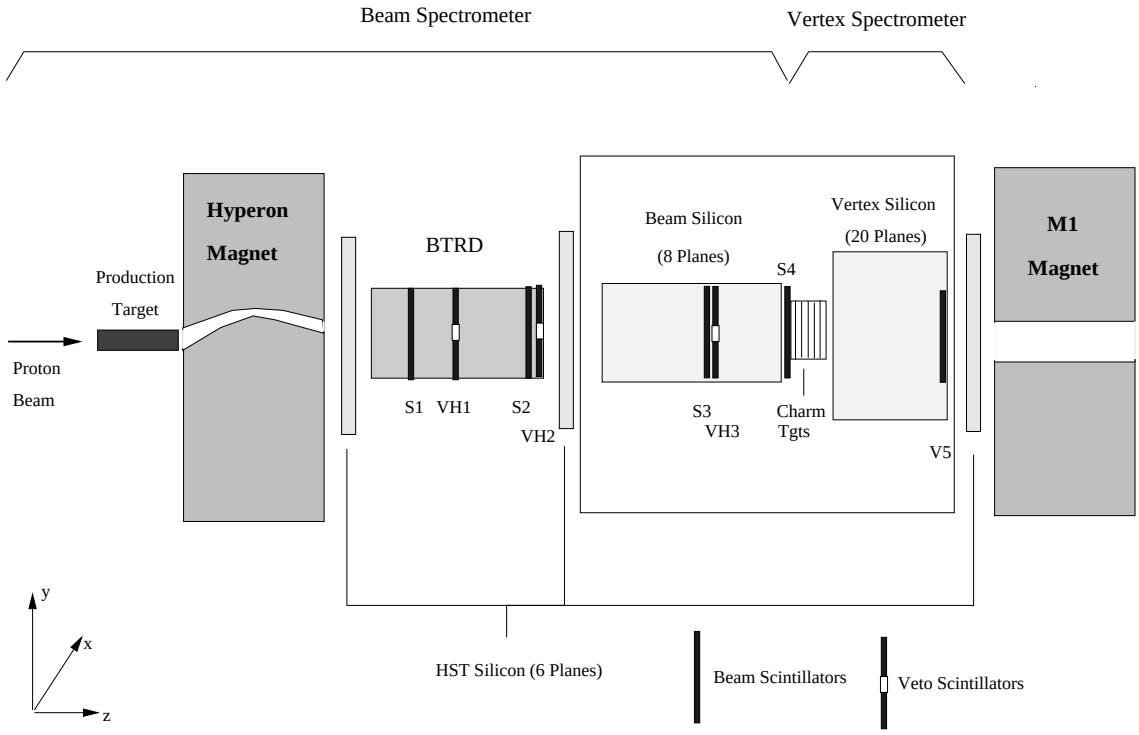

Figure 2: The Layout of the Beam and Vertex Spectrometers

station of hardware scattering trigger silicon detector and the beam silicon strip detectors. The the beam silicon strip detectors, together with the Hyperon magnet provided the trajectory and momentum of beam track, and the beam transition radiation detector supplied particle identification.

2.2.1.1 The Hyperon Production

The Tevatron at Fermilab supplied an 800 GeV/c proton beam to the Proton Center (PC) beam-line. The protons were focused on a $1 \times 2 \times 400 mm^3$ Beryllium (Be) production target. The production target was 0.98% of an interaction length and was located at the entrance of the 7.5 m long hyperon magnet (Figure 3). The gap of hyperon magnet was filled with layers of tungsten and lead, so that only particles with the right momentum could pass through the Hyperon channel. The 3.5 Tesla

hyperon magnet turned the beam through 11 $mrad$ so that the resulting beam had a radius of curvature of 619 m.

Under normal conditions, the Tevatron delivered 7×10^{11} $protons/second$ during a 20 second burst once per minute. Once the beam left the hyperon magnet, it passed through the beam transition radiation detectors. In the target region, the 600 GeV/c the Lortentz factor for π^- was $\gamma_{\pi^-} = 4676$ and for Σ^- was $\gamma_{\Sigma^-} = 543$ since π^- mass is much smaller than Σ^- mass. Thus, when Σ^- and π^- had momentum, the π^- emitted more transition radiation than Σ^- which in turn activated more planes. Figure 4 displays a typical distribution of the number of beam transition radiation detector modules activated for negative runs. The cut generally used for Σ^- was that number of the beam transition radiation detector modules activated should be less then 4 and for π^- number of modules activated should be more then 7. These cuts gave an identification efficiency of 89.5% for Σ^- and 91.5% for π^- [29].

2.2.1.2 The HST Detector

Upstream and downstream of the beam transition radiation detector four 50 μm-pitch silicon strip detector planes formed the upstream portion of the hardware scattering trigger [28]. Together with the downstream portion the hardware scattering trigger was used to identify the beam track which triggered an interaction in one of the charm targets (Figure 2). A fast processor defined a beam track from hits on these planes and detected scattering processes with the information coming from 2 additional planes downstream of the vertex silicon strip detector. The hardware scattering trigger silicon detectors employed short 80 ns gates, so that only hits from the particular beam particle that triggered the event were read out.

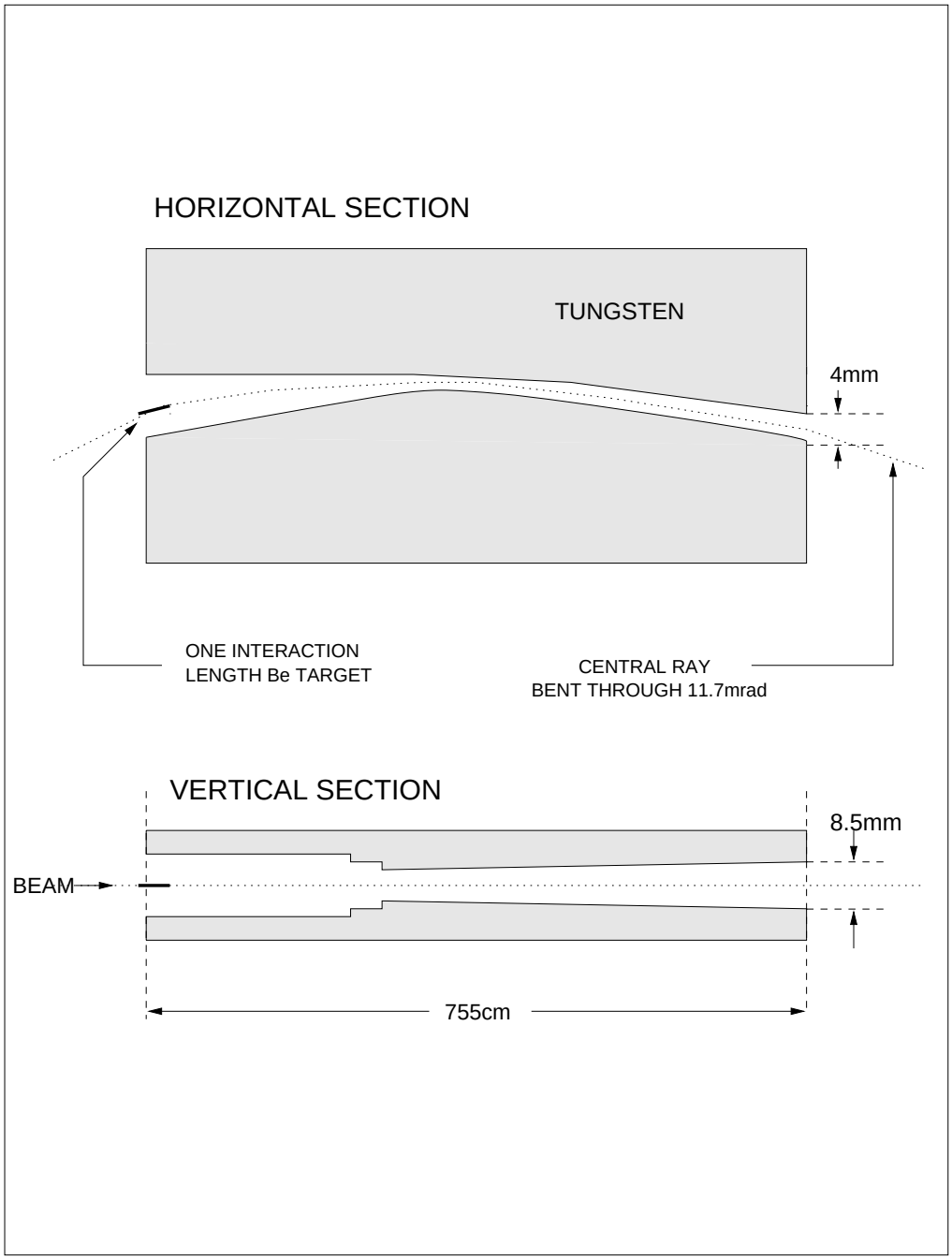

Figure 3: The Hyperon Magnet Schematics

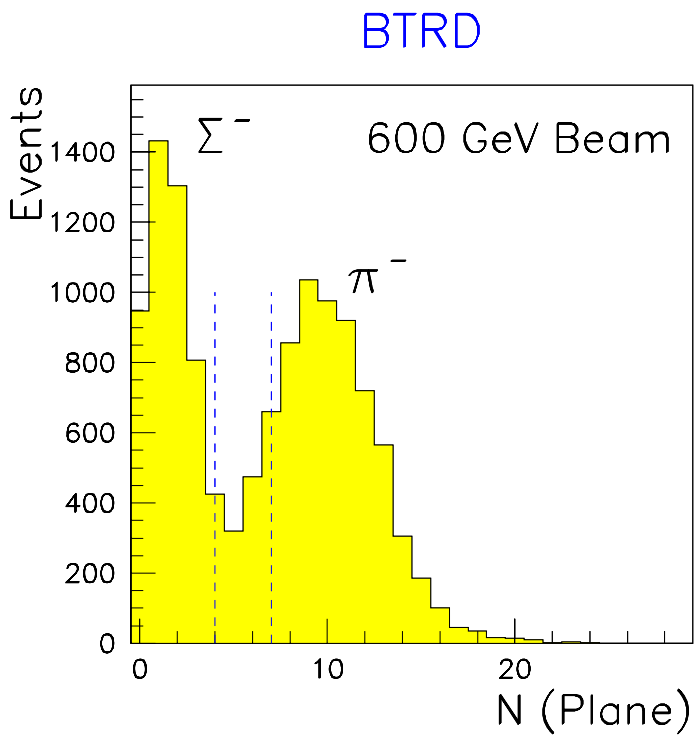

Figure 4: Σ^-/π^- Separation with the Beam TRD

2.2.1.3 The Beam Silicon Strip Detector

The beam silicon, vertex silicon, charm targets and trigger scintillator were enclosed in a light-tight aluminum box for RF shielding (Figure 5). The beam silicon strip detector consisted of 8 planes of 20μm pitch silicon strip detectors (SSD) with each detector having an active region $2 \times 2cm^2$. The beam silicon strip detectors determined the position of beam tracks in the target with about 4 μm resolution. The beam momentum was determined by extrapolating the beam track measured in the silicon detectors upstream to a known position of the hyperon production target. The hit efficiency for a single detector was more than 98% with an overall tracking efficiency of more than 95%. The typical momentum distribution for negative and positive beam particles is shown in Figure 6.

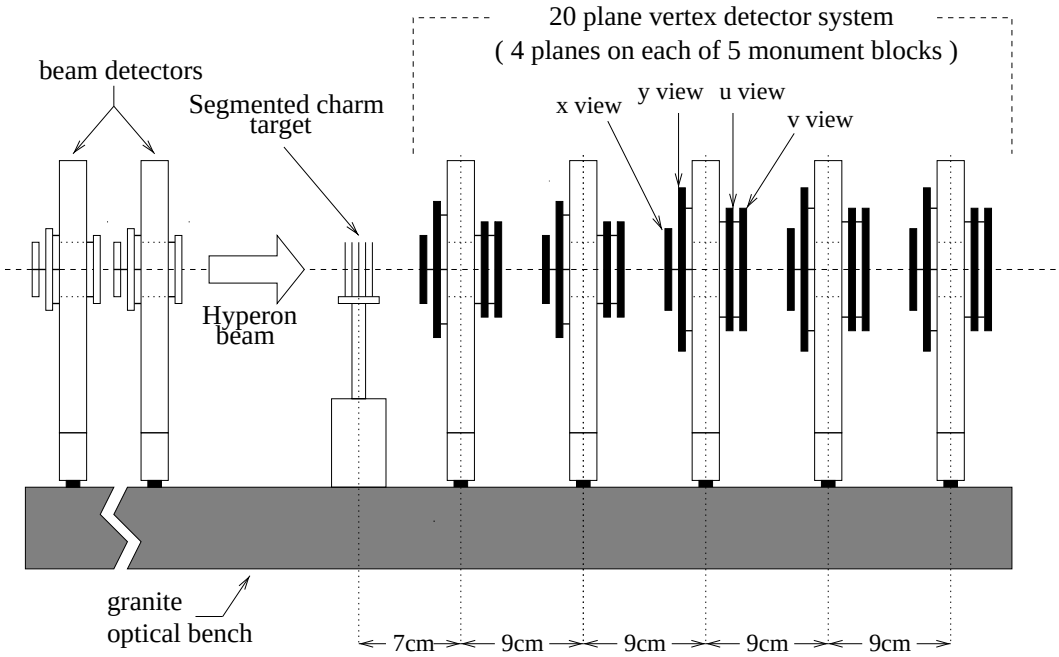

Figure 5: The Layout Inside the RF Cage

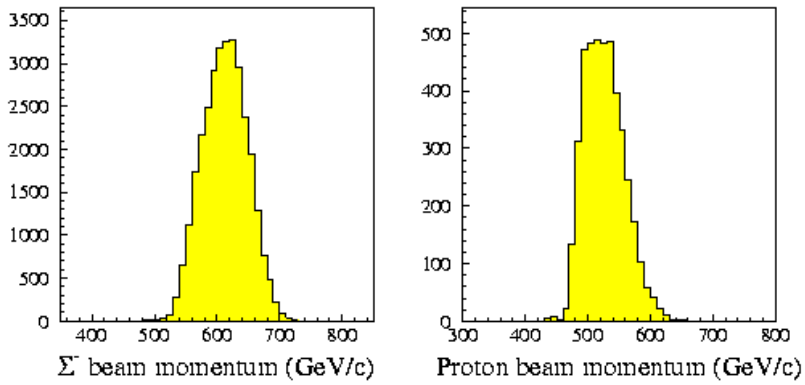

Figure 6: The Momentum Distribution of the Positive and Negative Beams

2.2.2 The Vertex Spectrometer

The Vertex Spectrometer consisted of the charm targets, an interaction counter and the vertex silicon detector [30] as shown in Figure 5. The vertex detector was the heart of tracking system of SELEX and was designed for high resolution tracking.

2.2.2.1 The Charm Targets

The charm target consisted of 2 copper blocks and 3 diamond blocks. Table 2 shows the thickness, z-positions and other properties of the 5 charm targets. The targets were separated along the beam line to allow a determination of the target in which the interaction occurred. The targets were removed from the beam line remotely to allow alignment data to be taken using non-interacting beam tracks. The bottom histograms in Figure 7 shows the constructed primary vertex position and the shaded rectangles shows the physical position of the targets.

Target	Material	Thickness [mm]	z [cm]	Atomic number A	Density [g/cm^3]	Inter length [%]
1	copper	1.6	-6.13	63.5	8.96	1.06
2	copper	1.1	-4.62	63.5	8.96	0.76
3	diamond	2.2	-3.10	12	3.20	0.82
4	diamond	2.2	-1.61	12	3.20	0.82
5	diamond	2.2	-0.11	12	3.20	0.82

Table 2: The Charm Target Properties

2.2.2.2 The Vertex Silicon Strip Detector

Immediately downstream of the charm targets, an interaction counter and 20 planes of the vertex silicon detector used for charged particle tracking were placed. The vertex silicon detectors consisted of 20 single sided, 300 μm thin detectors. The upstream 8 planes had an active area of $5.12 \times 5.00\ cm^2$ with 2560 strip at a pitch of 20 μm. The downstream mosaic detector consisted of three $8.3 \times 3.2 cm^2$ each with 25 μm pitch. The single hit efficiency of vertex silicon strip detector was more than 98% and the overall tracking efficiency was more than 95%. The vertex silicon strip detector was capable of 4 μm transverse position resolution at 600 GeV/c. The resolution for primary and secondary vertices was $270 \mu m$ and $560 \mu m$ [1], respectively (Figure 7).

2.2.3 The M1 Spectrometer

The M1 spectrometer was designed to track particles in a momentum range of $2.5 - 15 GeV/c$. It consisted of the M1 magnet which transverse momentum p_t kick 0.73 GeV/c, M1 multi-wire proportional chambers (PWC) [31], drift chambers (DC) [32], and large area silicon detectors (LASD) [33]. The layout of the M1 spectrometer is shown in Figure 8. The M1 multi-wire proportional and drift chambers were used to track low momentum or "soft" particles, while the high momentum or "stiff" particles were tracked using the high precision large area silicon strip detectors.

2.2.3.1 The Large Area Silicon Detector

The Large Angle Silicon Detectors were located downstream of the vertex area with the purpose of covering the beam region of the downstream wire and drift chambers to improve the track resolution and allow precise momentum measurements. The average resolution of the LASDs was 15 μm and their efficiencies ranged from

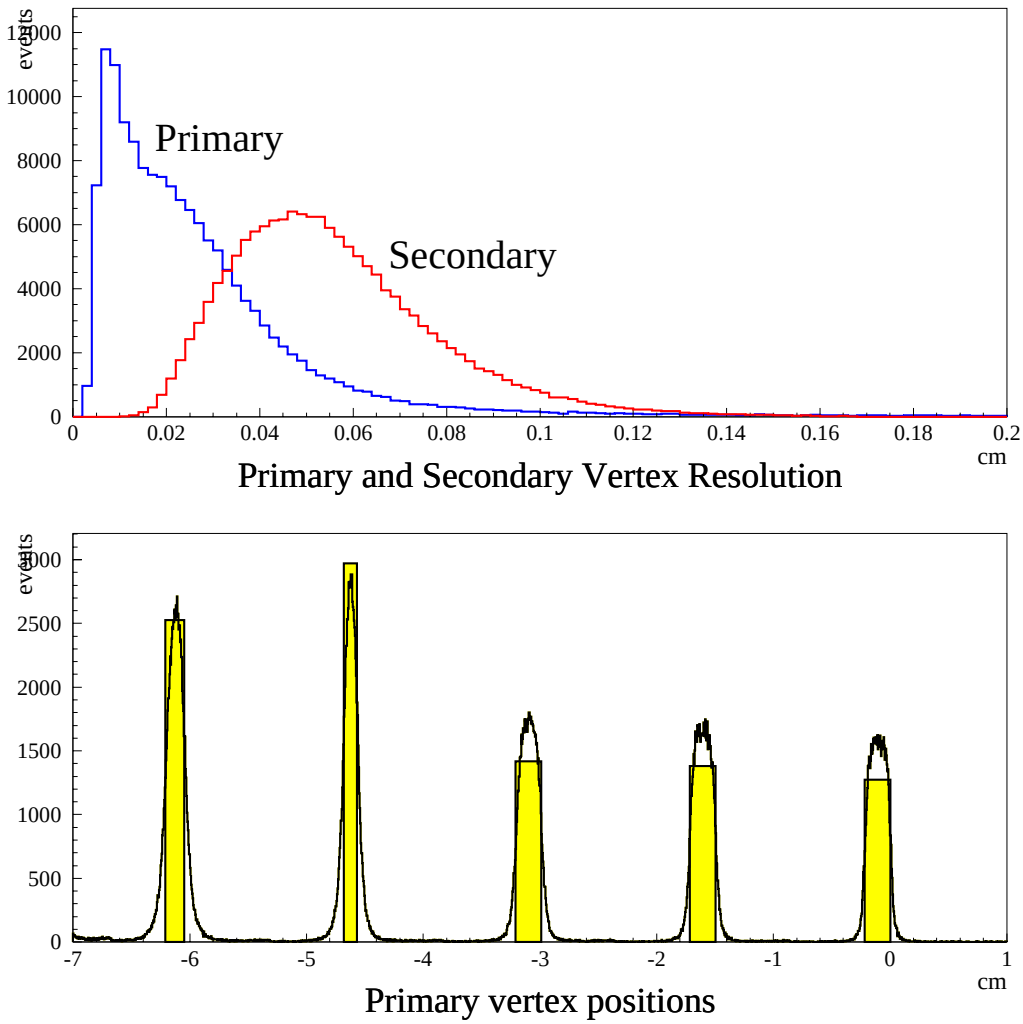

Figure 7: The Primary and Secondary Vertex Resolutions and Targets

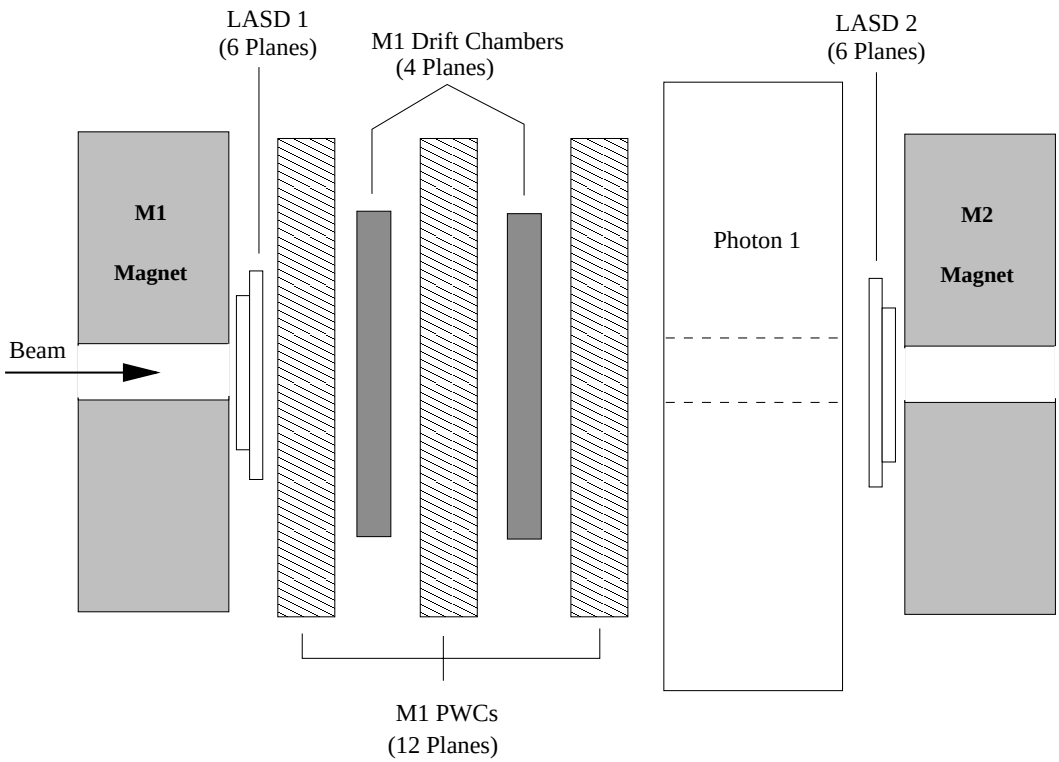

Figure 8: The M1 Spectrometer Layout

91% to 99% [33]. The detectors are divided in three groups and placed in the downstream end plate of the M1 magnet starting at z-position of 638.28cm and in both plates of the M2 magnet at z-positions of 1110.9 cm and 1331.88 cm, respectively. Each group consisted of two single-sided silicon detectors and two double-sided silicon detectors to determine two points for each of the three projections (x, y, and u). Both types of silicon were 300 μm thick with the single sided having an active area of 6.35×6.35 cm and the double-sided 5.26×6.64 cm with total of 2540 strips. The double-sided detectors were employed to reduce the overall radiation length.

2.2.3.2 M1 Wire Chambers

The M1 proportional wire chambers (PWCs)allowed acceptance for the "softer" particles i.e. those with momentum less than $15 GeV/c$. These multi-wire proportional

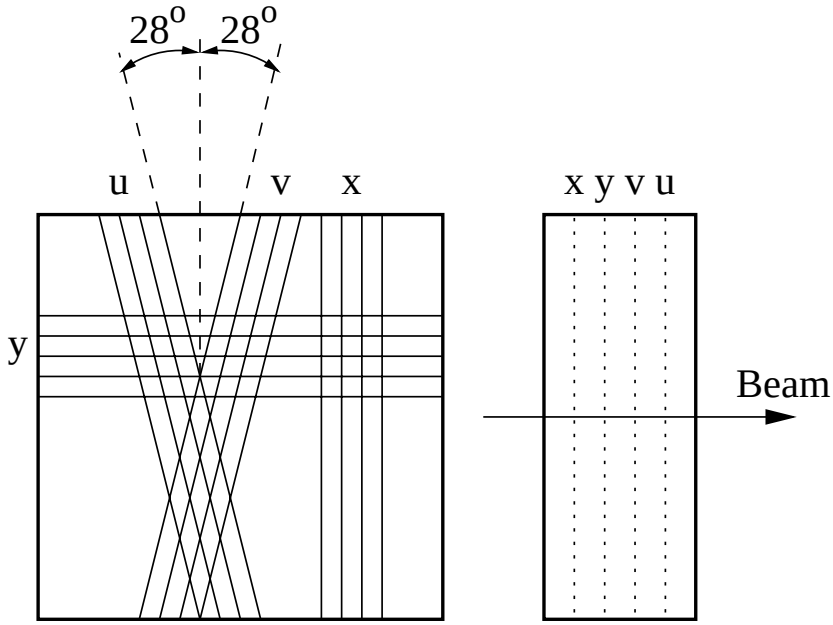

Figure 9: The M1PWC Anode Wire Orientations

chambers covered an area $2000 \times 2000 mm^2$ with 640 gold plated tungsten wires with 3mm spacing, giving a resolution of $0.6\, mm(d/\sqrt{12})$. There were four different anode plane orientations (x, y, v and u) in each multi-wire proportional chamber vertical, horizontal and slanted planes with an angle of $\pm 28.070\ ^o$ with respect to the vertical direction (Figure 9). The separation between two anode wire planes was 12 ± 0.05 mm. The chamber was filled with gas mixture of 75% argon, 24.5% isobutane, and 0.5% freon. The gas would ionize when a charged particle passed through it. The ionized gas consists of electrons and positively charged ions. The positive ions would drift in the electric field to the cathode and the electrons would drift to anode. When the electrons are close to an anode wire, a process of avalanche formation occurs greatly increasing the signal collected by the wire.

A more detail information about M1 and M3 multi-wire proportional chambers

and their read out system is given in Appendix A. These chambers were a major contribution of the University of Iowa and my hardware responsibility throughout the experiment was to maintain them.

2.2.3.3 The M1 Drift Chambers

The two M1 drift chambers were designed to improve the angular resolution of tracking in the horizontal bending plane of M1 magnet. They were sandwiched in between the M1 PWCs. The drift chambers exploit the measurable time between the passage of a particle and the arrival of the signal at the anode wires. If the drift velocity of particle in the drift chamber is known and a trigger is available to signal the arrival of the particle, the distance from the anode wire to the origin of the particles trajectory can be calculated to enhance the resolution of the detector.

2.2.3.4 The Photon Detector(s)

The photon detection system of the SELEX spectrometer was a significant part of the setup. The photon system consisted of three electromagnetic calorimeters, so called the Photon1, Photon2, and Photon 3. The Photon1 detector was located after the M1 multi-wire proportional chambers, the Photon 2 was located after the ring imaging Cherenkov counter in M2 spectrometer, and Photon 3 was located in M3 spectrometer after the M3 multi-wire proportional chambers.

High energy electrons lose their energy almost exclusively by bremsstrahlung. The result of the bremsstrahlung losses inside the lead glass lead to photons which were collected by the photo-multiplier tubes. The integrated energy collected by the tubes could then be used to estimate the energy of the incident particle.

All three calorimeters were matrixes of total absorption counters made of transparent lead-glass. The advantage of using lead glass is the radiation hardness of the glass. The lateral dimensions of the glass block were comparable to the width of

electromagnetic showers in this medium, so the calorimeters were able to measure simultaneously the coordinates (with an accuracy of 1.5 mm), and energy (to a few percent) of a large number of gammas and to reconstruct the masses and momenta of the particles decaying into gammas.

2.2.4 The M2 Spectrometer

The M2 spectrometer consisted of the M2 magnet, the H1 and H2 Hodoscopes [34], the M2 multi-wire proportional chambers [35], the electron transition radiation detectors (eTRD) [26] and the Vector Drift Chambers [36]. The M2 spectrometer was designed to track, and identify the "stiff" particles (momentum larger than 15 GeV/c) from the interaction in one of the charm targets. The M2 magnet was operated at a field strength of 1.54 T which corresponds to a p_t kick of 0.845 GeV/c. The first detector in the M2 spectrometer was the third LASD station. It was located at the exit to the M2 magnet and consisted of 2 single-sided and 2 double-sided silicon detectors.

2.2.4.1 The H1 and H2 Hodoscopes

Two scintillation counter hodoscopes locate in the M2 spectrometer provide a fast response on the charge multiplicity of the particles through the spectrometer. This information was used by the trigger in deciding whether to trigger on an event. The hodoscopes consist of three regions covering the negative-charge, central and positive-charge regions of the M2 spectrometer. The H1 had a coverage area of $60.0 \times 30.5\ cm^2$ at z position 890.0 cm and H2 located at z 1292.1 cm with coverage area of $119,0 \times 40.6\ cm^2$.

2.2.4.2 The M2 Wire Chambers

The M2 proportional wire chambers (14 planes in 7 modules) were located downstream of the M2 magnet and used to measure coordinates and momenta of the

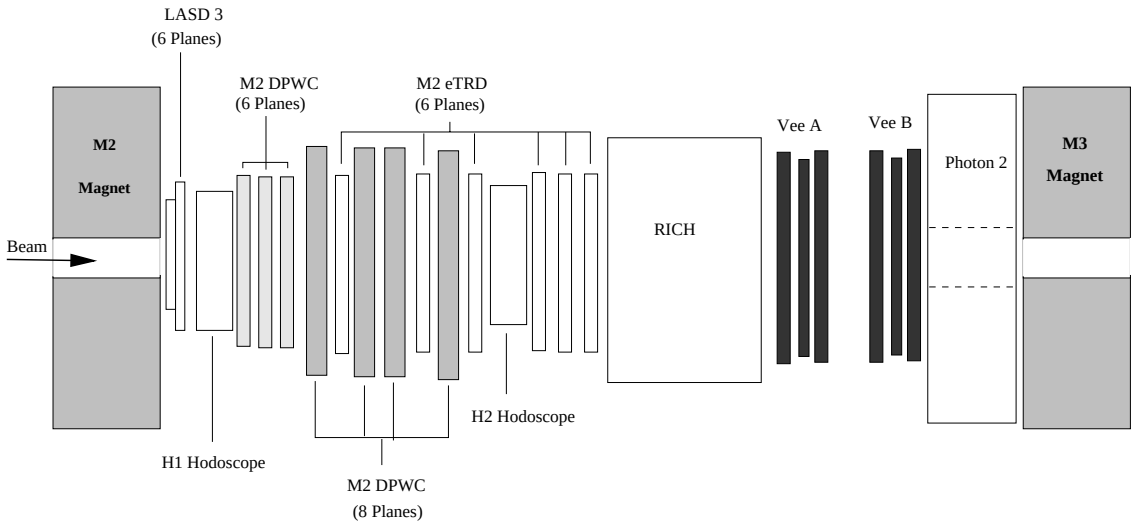

Figure 10: The M2 Spectrometer Layout

charged particles. The 4 downstream chambers have a $60 \times 100\,\mathrm{cm}^2$ aperture. Each chamber has 2 sensitive planes in 2 orthogonal projections. The chambers had greater than 95% hit detection efficiency with 0.6 mm spatial resolution [35].

2.2.4.3 The Electron TRD Detectors

The electron Transition Radiation Detectors were interleaved within the other detectors in M2 spectrometer. The electron transition radiation detectors were specifically designed to give good electron identification.

The electron transition radiation detectors consisted of 6 modules, each a combination of 200 polypropylene foils and a proportional wire chamber. This foils were 17 μm thick and separated by 0.5 mm gaps. The chambers had 4 mm effective wire spacing with coverage area of 103×63 cm^2. A charged particle identified as an electron if the sum of the cluster along the track in the 6 planes was greater than three

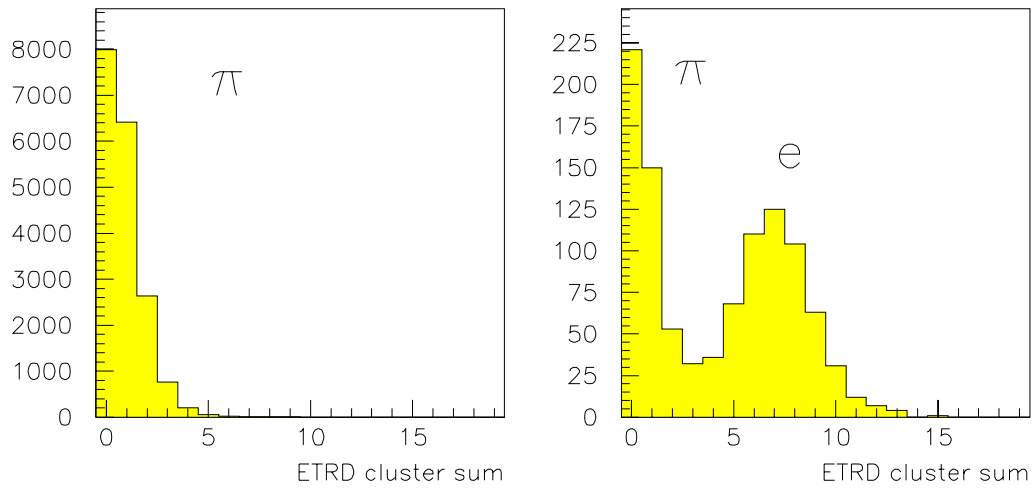

Figure 11: ETRD Separation for π (Left) and Both π and e (Right)

(Figure 11). The electron transition radiation detectors were found to be 95% efficient in momentum less than 20 GeV/c and 91% efficient for typical electron momenta during the run.

2.2.4.4 The RICH Detector

The main particle identification detector for SELEX was the Ring-Imaging Cherenkov Detector (RICH) [37]. When a charged particle travels in a dielectric medium of index of refraction $n > 1$ with a speed greater than the speed of light in that medium (i.e. $v > c/n$) it emits electromagnetic radiation which forms a coherent wavefront - similar to the sonic shock wave created by supersonic aircraft- of conical shape. The angle of emission for Cherenkov light is given by

$$\cos\Theta_c = \frac{1}{n(\omega)\sqrt{1-\frac{1}{\gamma^2}}} = \frac{Emc}{n(\omega)p^2}$$

where ω is the frequency of the emitted radiation and $\gamma = E/mc^2$ is the relativistic Lorentz factor. The Cherenkov effect therefore provides a means for distinguishing

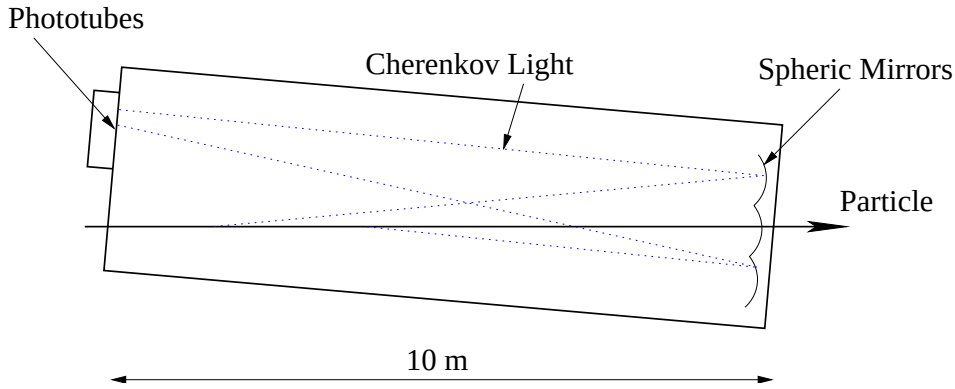

Figure 12: Demonstration of the Cherenkov Light in the RICH

two particles with the same momentum but different masses. The reflection of the Cherenkov radiation from a spherical mirror onto o the photo-tubes is demonstrated in Figure 12.

The RICH had a 10 meter long Neon filled cylindrical vessel with a diameter of 2.34 m. The downstream end of the vessel consisted a matrix of 16 hexagonally shaped spherical mirrors of total area $2.4m \times 1.2m$ with focal length of 10m. The mirrors reflected the Cherenkov photons back to an array of 2848 photo-multiplier tubes position at the upstream entrance of the vessel. For a fixed $\cos\Theta_c$ the image of the Cherenkov light is a circle, which means particles with different masses produced circles of the different radius. Figure 13 is a single event display which demonstrates this.

If the momentum of the particle was known, then the particle was identified with varying levels of certainty using their known mass values. A single track resolution of 2 σ_r gives a $\pi - K$ separation up to about 165 GeV/c and $p - k$ separation up to 320

GeV/c [38]. Figure 14 shows the expected ring radii for various particles types as a function of momentum. The two horizontal lines on the lower plot show the achieved resolutions for single track and multi-track events, respectively.

2.2.4.5 The Vector Drift Chambers

Most of the detectors in the SELEX spectrometer provided position information. The vector drift chambers on the other hand, were designed to provide short track segments of charged particles in addition to the usual position information. Two of the three vector drift chambers (VDC) were located after the ring imaging Cherenkov counter. These detectors consisted of a fine cell region centered around the beam line and a coarse cell region away from the beam. The VDCs were designed to track downstream decay products by providing high resolution, short track segments within each station. Each station consisted of three axes (x,y,u/v) with active region of $1.16 \times 1.16\ m^2$.

2.2.5 The M3 Spectrometer

To enhance the acceptance for decays of long-lived hyperon states like Λ, the M3 magnet with a field strength of 1.3T providing a p_t kick of 0.72 GeV/c was installed 42 m downstream of the charm targets as part of M3 spectrometer. The M3 spectrometer consisted of two multi-wire proportional chambers, the third vector drift chamber, the photon 3 detector, and the neutron calorimeter. This spectrometer was not used in this analysis.

Event Display

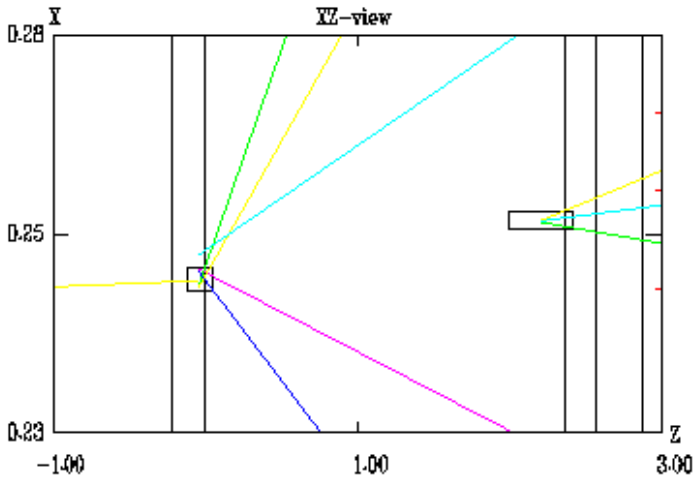

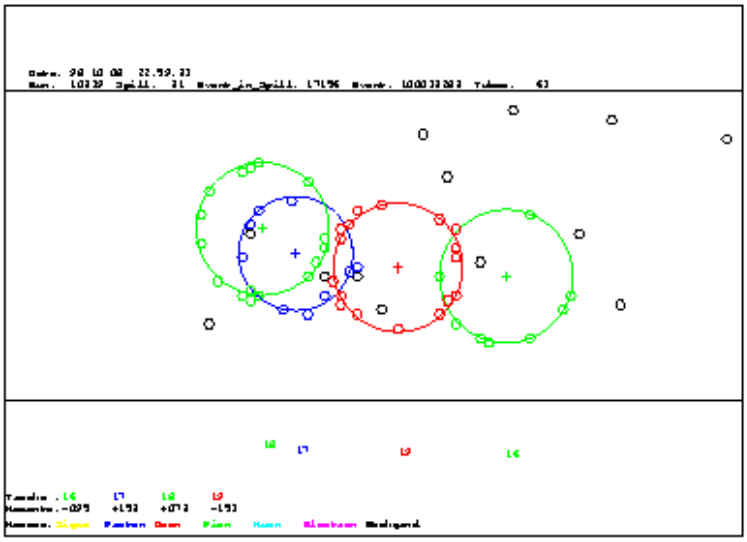

SELEX 11

Figure 13: A Single RICH Event Display

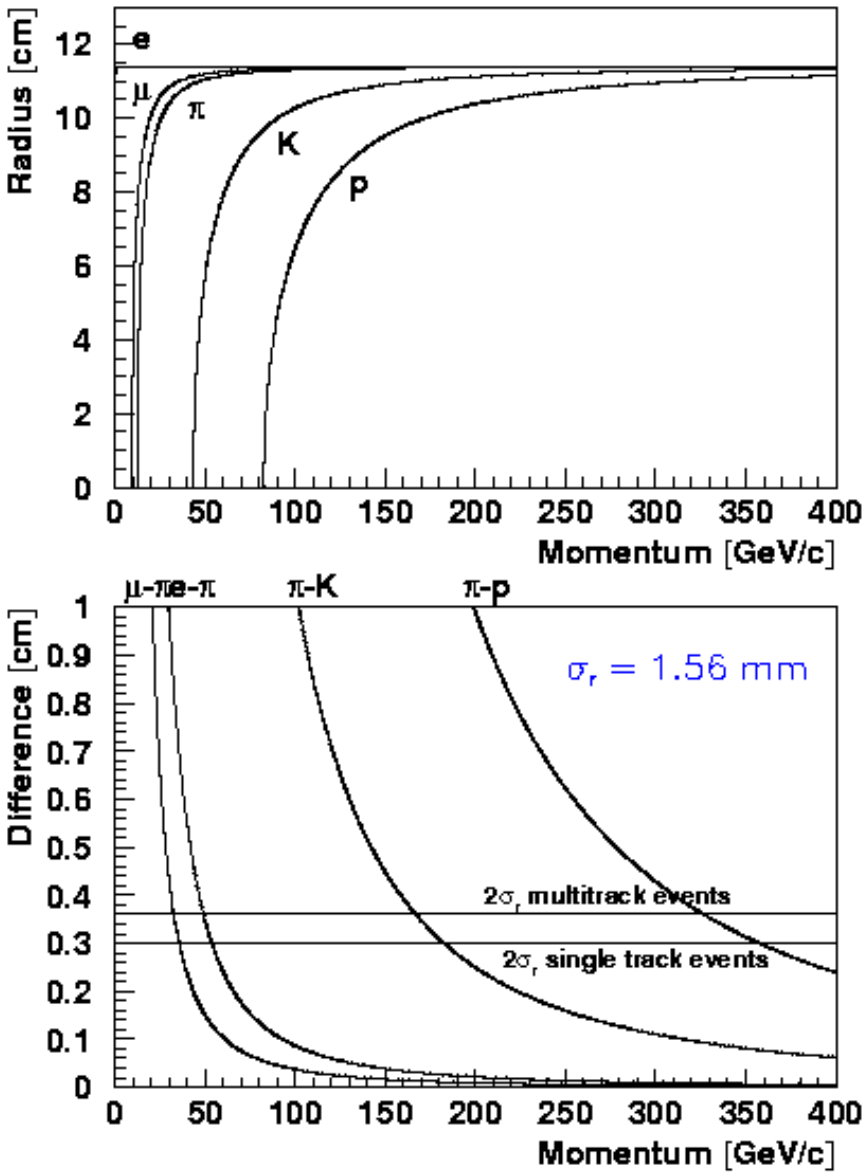

Figure 14: RICH Ring Radius and Difference Versus Momentum

CHAPTER III
THE TRIGGER, DATA ACQUISITION AND OFFLINE ANALYSIS

The trigger system in SELEX consisted of three hardware, (HW) and one software trigger levels. The main function of hardware trigger was to reduce the background to a reasonable level combined with high acceptance for charm decays. The hardware trigger reduced input event rate by a factor about 10, and also minimized dead time due to events readout. The software trigger on the other hand reduced the data by a factor of 8 more while having only a small effect on the charm signal. Using an software trigger was unique to the SELEX and it was made possible by the fast data acquisition system. The software trigger was used to enhance the charm signal relative to background. For our study, however, trigger introduced a bias so it was not used. The SELEX data acquisition system was able to manage large data streams which permitted event selection mainly by software, and making the trigger more intelligent and flexible. We will discuss the trigger and data acquisition system in the following sections.

3.1 The Trigger System

A large variety of arrival times of detector response to the trigger circuit and a high data rate of SELEX experiment required a multi level trigger system. This structure of the trigger also fits multilevel synchronization of hardware triggers with external environment such as the silicon strip detector, the front end electronics and the data acquisition system.

SELEX had 3 levels of hardware triggers (T_0, T_1, T_2) and one level of software

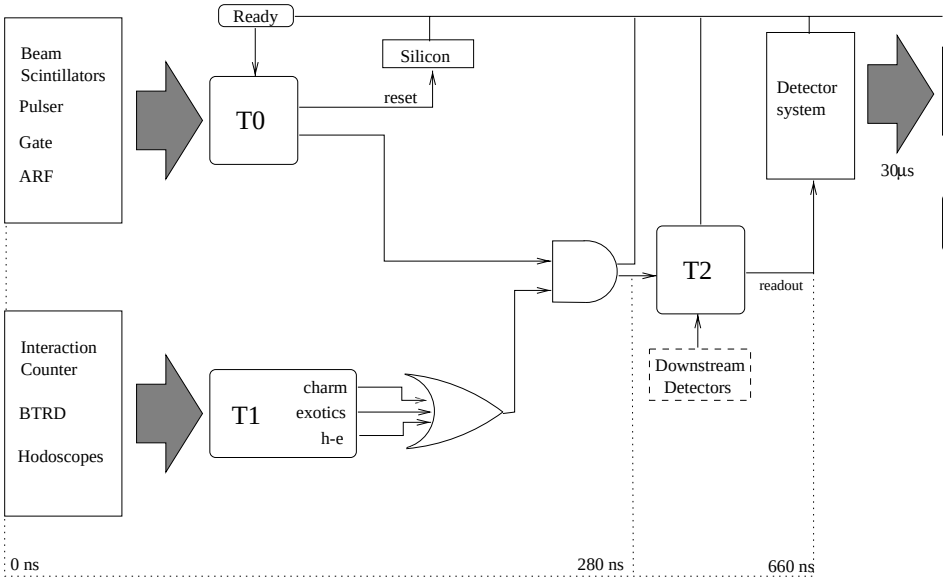

Figure 15: The Schematics of SELEX Trigger System

trigger which interfaced with the hardware trigger via the data acquisition system. The trigger was based on information from detectors in the beam, vertex and M2 region as shown in Figure 15.

The initial trigger level T_0 defined a valid incident beam particle. The beam transition radiation detector made the separation of the mesons and baryons, but not until T_1 time. The triggers expected low multiplicity and high momentum tracks after the second magnet M_2. This information came at T_1 time and then the T_2 was formed by a coincidence of T_0, T_1, and some signals from slower detectors like the downstream electron transition radiation detectors and the scintillator hodoscopes H_1 and H_2. A valid T_2 trigger sent a signal to the data acquisition system to start readout process of the all the detectors. Once the data acquisition started the readout, the software trigger selected events that made a full vertex reconstruction of the beam track and all tracks in the M2 spectrometer (high momentum tracks) to test the hypothesis that

they all came from a single primary vertex. The events pass the requirements of the software trigger written-out to the local disk for the further offline analysis. Table 3 shows the trigger primitives.

Trigger Level	Detector	Trigger Primitive
T_0		
	Beam Gate	Accelerator
	Accelerator RF	Synchronization
	$S_1 S_2 S_3$	(Prescaled) Beam
	Interaction Counter	Post–target multiplicity: I_1, I_2, I_3, I_{Mult}
	Computer generated triggers	Test / Calibration
T_1		
	Beam TRD	Beam Type π^-/Σ^-
	Primakoff Horoscope	1 charged product; not beam
	Scintillating Hodoscopes $H_1 H_2$ and hodoscope Matrix	Number of fast tracks after M_2
T_2		Downstream ...
	Scintillator	... Λ
	Downstream TRD	... e

Table 3: The Trigger Primitives

3.1.1 The Hardware Trigger Levels

The T_0 operated with information from the beam scintillator interaction counters to identify beam particle and interaction in one of the charm targets. The T_0 is defined as $T_0 = S1\ \overline{VH1}\ S2\ \overline{VH2}\ S4\ V5$. Here $S1, S2, S3$ are the beam definitions, $VH1, VH2, V3$ are the beam halo Vetos Figure 2 The $S2 > 1$ and $S3 > 1$ wereused

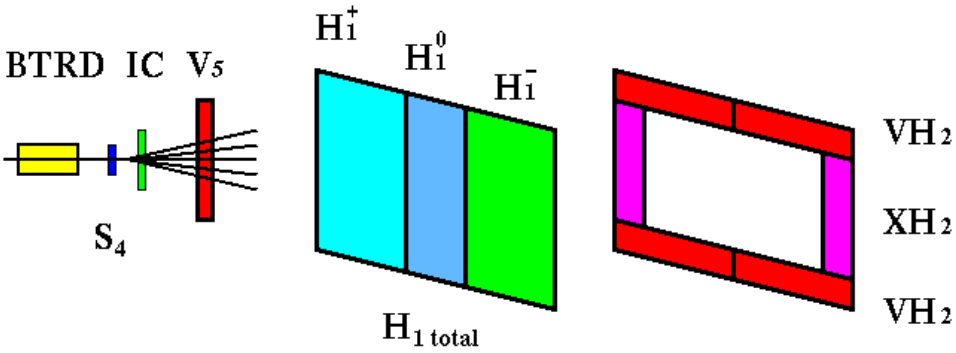

Figure 16: The Detectors Used in T_1 Trigger Levels

to kill upstream beam interactions and $V5 > 1$ was required for minimum interaction. T_0 also counted beam particles to provide a clear for the silicon detectors when too many beam particles came through without interaction. If such an event found a T_0 formed and it started a T_1 decision circuits and provided synchronization for the next stages.

The T_1 logic required a valid T_0 tag, the beam particle identification from the beam transition radiation detector and information from detectors near M2, i.e., the scintillator hodoscopes (Figure 16). The scintillator hodoscopes H_1 and H_2 consisted of a programmable matrix of scintillator. There were used to discriminate hits of stiff tracks originating in the near target region. It was possible to count the positive and negative tracks separately. Hodoscopes H_1 and H_2 had elements of varying width, with fine segmentation in the near beam region and wide elements on the far edge. To prove that a track comes from the upstream region and has proper momentum it was sufficient to check that the H_1 and H_2 elements that fired belong to the valid area. There were extra hits in each hodoscope and combinatorial effects were possible, but extensive Monte Carlo studies showed that the number of the ghost tracks found by the matrix was low [34]. A positive T_1 decision formed according the these

requirements started a T_2 trigger.

The T_2 level required additional information from detectors in the downstream region and applied selection cuts on information coming from these detectors. If successful, the readout of the detectors was initiated. Once the detector systems were readout, the online software filter analyzed the event before saving the data to tape.

3.1.2 The Software Trigger

One of the innovations of the SELEX experiment was the online filter. This was a program which ran between the beam spills and processed data to reject events that did not have evidence for a secondary vertex.

First, the filter program reconstructed tracks in the downstream tracking detectors (mainly M2 PWCs). Only tracks with momenta greater than 15 GeV/c could make it through the magnets to reach these chambers. After that a beam track was reconstructed , the tracks from the downstream tracking detectors were extrapolated back to the vertex silicon, using beam track information as a guidance to the approximate primary vertex location. A special fast reconstruction program searched for track segments in the vertex silicon, using the downstream track extrapolations as an initial starting parameters and looking for hits in searching windows around them. The sizes of searching windows were calculated based on the resolutions of the detectors and the effects of multiple scattering. Because only relatively large momentum tracks (> 15 GeV) were extrapolated back to the vertex silicon multiple scattering errors were kept under control. The beam track and the secondary tracks reconstructed in the vertex silicon and downstream chambers were fitted to a primary vertex. If the fit had an acceptable χ^2 and used all tracks, the event was rejected, on the other hand, if one or more tracks did not point to the common vertex, the event was kept and written to the tapes.

3.1.3 Trigger Synchronization

The trigger was synchronized with the beam. Each level took a tag from a positive decision at the previous level and asserted the busy. This occurred from T_0 to T_2 until either a negative decision was reached or T_2 gave a positive decision reading the detector data into data acquisition system. When either occurred, the level completed and terminated its processes and reset it's gate generator passing the clear back to the previous level until the T_0 gate reset, ready for the next spill. In the case of T0, a tag came from the beam gate signaling when the beam was on or off spill. The level became busy and held the busy until its processes had finished and a level decision had been reached. If a negative decision was reached then the gate reset after the level had finished its tasks and the clear was passed back to the previous level, or in the case of T_0 the busy was released ready for the next event. For a positive level decision the busy was passed on to the next level and the process was repeated until either a negative decision was reached at one of the levels or until a positive decision was formed at the T_2 level and the detector data was read into data acquisition system. In this case a busy was also held by the detector systems being read to data acquisition system. Upon completion T_2 reset and passed the clear to T_1 and eventually to T_0 as in the case of a reset from a negative decision. Synchronization between trigger levels was achieved by a synchronization signal confirming the logic was ready.

3.1.4 The Trigger Types

There were five basic types of trigger, namely; Interaction, Beam, Gpulser, Lpulser and Random.

The interaction trigger was the standard trigger setup used to trigger on interactions in the charm target. It was used with the spectrometer magnets on and the

charm target in the beam.

The beam trigger was used to find beam particles as they passed through the beam and vertex spectrometers. This type of trigger was primarily for used calibration purposes such as alignment of the detectors with the target out of the beam and all 3 analyzing magnets turned-off. This trigger proved to be free of biases and we used it for the study of particle production ratios with three analyzing magnets turned on and target in them beam. Only events satisfying this trigger were used in the analysis (see Section 4.1)

The Gpulser, Lpulser and Random triggers could be used regardless of whether beam was present or not. A pulse generator was used to generate artificial trigger pulses. It was generated through the system at a fixed/random frequency This provided triggers asynchronous to the beam particles to search for noise within the SELEX detector.

3.2 The Data Acquisition System

The SELEX data acquisition system was developed in close collaboration with other experiments and the Fermilab Computing Division as part of DART project [39]. A schematic layout of the system is shown in figure 17. All front end electronics with about 105,000 channels is situated in the experimental pit, the end is shown left of the dashed line in Figure 17. The data collected in ten parallel streams and transported via fiber optic data links, over some 100 m, and stored in VME dual ported memories. We collected 100,000 events with 650 MByte of data over the twenty second spill.

During the 1 minute cycle time of the Tevatron the data was transfered via a fast VME to VME crate interconnect to two SGI Challenge L with 22 processors total, with a total computing power of 2500 MIPs. The data was distributed to 20 filter

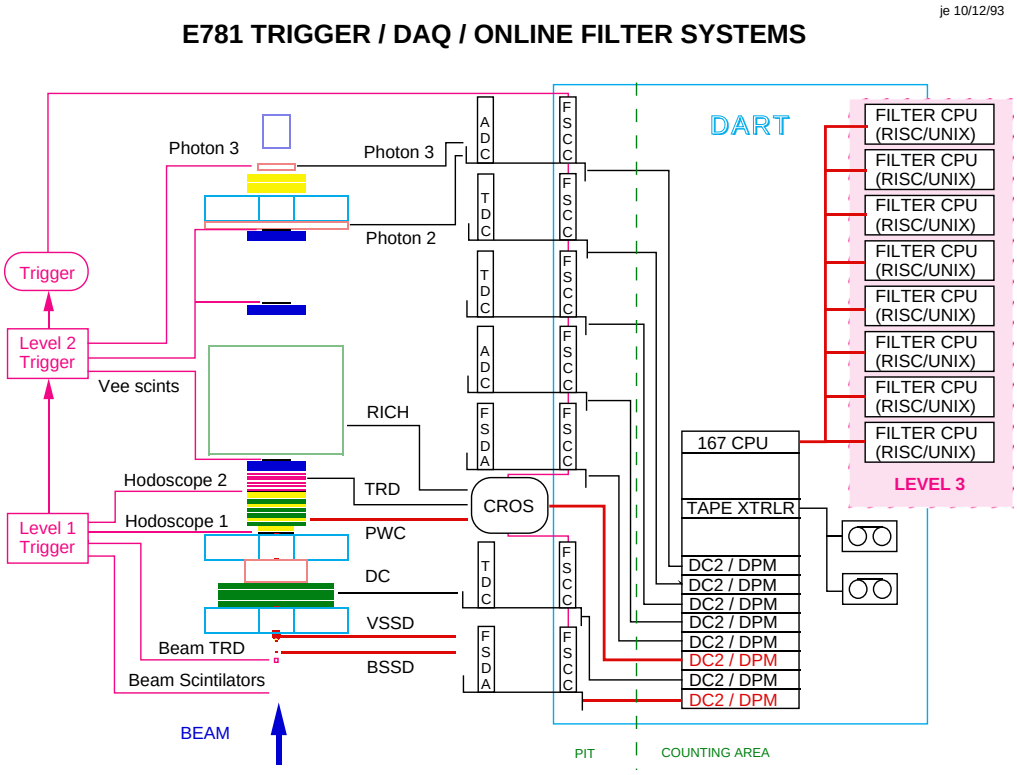

Figure 17: Schematic View of the SELEX Data Acquisition System

jobs using the DART Data Flow Manager (DFM). After a positive decision of the level three filter job the events were written to disk files, from where they were copied a- to 8 mm exabyte tapes. The total rate to disk/tape was about 1500 KByte/sec.

3.3 The Off-line Data Processing

The SOAP (SELEX Off-line Analysis Program) was a combination of analysis packages used to process the data collected by SELEX. These analysis packages were

- UNPACK to load raw data in common blocks
- TRACKING to find all the tracks
- VERTEX to find the primary and secondary vertices
- PARTID to find combined particle identification of a track
- RECON to reconstruct the decays
- USER to perform a specific analysis of data

The raw data was first unpacked into common blocks with the UNPACK package. The raw data contained some important event descriptions such as run number, spill number, pointers to detector, and hit positions in that detector's planes.

Once the data was unpacked into common blocks, TRACKING packages engaged and each spectrometer searched hits for patterns corresponding to straight lines track segments in space. This was done by using a set of predefined initial plane list and combinations as shown in the example in Table 4. These combinations specify which detectors can be used, which detectors were required to be used and track segment constraints such as the minimum number of detector planes used in finding a track segment for that combination. In addition, other requirements for the track such as position and angle constraints, could be specified.

```
comb: bm_comb1
      planelist:  bm_ssd_ 1x1y1u2x2y3x3y3u
      planeinit:  bm_ssd_1y bm_ssd_3y bm_ssd_1x bm_ssd_3u
!     cut names   xl   xh   txl   txh   yl  yh   tyl   tyh  xs  ytgt  chi2  npl
      cuts:       0.,  0.,-.0012,.0012, 0., 0.,-.0012,.0012,0.0, 0.2,   4.0,  7
*end
!
comb: vx_comb1
      planelist:  vx_ssd_ 1x1y1u1v2x2y2u2v
      planelist:  vx_msd_ 1x1y1u1v2x2y2u2v3x3u3v4x
      planeinit:  vx_ssd_1u vx_ssd_1v vx_msd_2x vx_msd_2y
!     cut names   xl   xh   txl   txh   yl  yh   tyl   tyh   xs  ytgt chi2  npl
      cuts:       0.,  0.,-.025, .025,  0., 0.,-.025, .025,    ,    ,  5.0, 12
*end
comb: vx_comb2
      planeinit:  vx_ssd_2x vx_ssd_2y vx_msd_3u vx_msd_3v
!     cut names   xl   xh   txl   txh   yl  yh   tyl   tyh   xs  ytgt  chi2 npl
      cuts:       0.,  0.,-.100, .100,  0., 0.,-.100, .100,    ,     , 20.0, 10
*end
comb: m1_lasd2a
      planeinit:  m1_dsd_1x m1_dsd_2x m1_ssd_1v m1_ssd_2u
!     cut names   xl  xh   txl  txh  yl  yh  tyl   tyh  xs  ytgt chi2  npl nhit
      cuts:      -5., 5.,-.025,.025,-5., 5.,-.023,.023,  0., 0., 22.5,  5, 900
*end
comb: m2_14_10
      planelist:  m2_pwc_ 1x2x4x6x7x 3
      planelist:  m2_pwc_ 1y2y4y6y7y 3
      planelist:  m2_pwc_ 3u3v5u5v   3
      planeinit:  m2_pwc_1y m2_pwc_6y m2_pwc_1x m2_pwc_6x
!     cut names   xl  xh txl txh  yl  yh tyl tyh  xs ytgt chi2 npl nhit ptx p f
      cuts:       0., 0., 0., 0., 0., 0., 0., 0., 0., 0., 1.0, 14, 0, 0., 0., 3
*end
link   prog bmdown
link   copy bm                      ! convert beam tseg into track
link   prog m2down
link   copy m2                      ! copy M2 segments
!
tracking  silmatch   target         ! choose target for primary interaction
tracking  pnt_seg                   ! KDN routine
!tracking  dc_segment a2b2c2         ! find segments in dc spectrometers
tracking  fit                       ! momentum fit all fittable tracks
!tracking  tr_crack    kink          ! LD 5/27/99 separate from track_user
!tracking  tr_kink     kink          ! LD 5/27/99 separate from track_user
tracking lasd_add                   ! add lasd hits to m1/m2 tsegs (RMB code)
tracking trk_chk1                   ! error checking/verbose
tracking trk_chk0                   ! error checking/quiet
```

Table 4: A Sample Initial Plane List File

After the segments were found, the track segments from the different spectrometers were then combined to form tracks according the track segment file which specified the algorithms used and the order of processing in forming tracks from the track segments. The use of control files allowed for the largest versatility with the ease of use in finding the best algorithm needed for finding different types of tracks.

Once the track segments and tracks have been found, the VERTEX package is activated. The VERTEX package first extrapolates all the tracks having a VSSD segment to the seed vertex position. This includes multiple Coulomb scattering effects from the interaction counters. Next, the primary vertex assignments are tested for all the tracks and the χ^2 of the fit and miss-distance to the beam track is calculated. If the vertex fit χ^2 is too large then the tracks with the largest χ^2 is removed from the vertex. When all the tracks are found in an event the PARTID package was activated. PARTID package got all the information from the beam (and electron transition radiation detectors where used), the ring imaging Cherenkov counter and the photon detector (when used). Then for each track in that event a combined particle identification word added the track information and RECON package was called. RECON used a pre-defined list of particles and their decay modes as shown in Table 5 looped over the track list and tried all the possible combinations of tracks to reconstruct particles. Then USER specific packages called for specific analysis purposes. The event selection for a specific analysis was done at this level.

The individual packages were controlled by a user defined file. Each package has a group of switches defined and cuts to control how it is executed. A sample control file can be seen in Table 6. Within this file, different packages could be turned on or off.

```
#recdf      0     0 fill anal v01.20 04-Mar-1998 16:32 psc
  id  name       from pr q  pid   ls_min ls_max mass_min mass_max   out
!
! Strange states
   1  kshort      v2  2  0  i-i+       5.  800.   0.470  0.530  $100008
   2  lambda      v2  2  0  p+i-       5.  800.   1.090  1.140  $200008
   3  alambda     v2  2  0  p-i+       5.  800.   1.090  1.140  $200008
   4  phi         c   2  0  k+k1-      0.    0.   0.995  1.045  $400000
   4  phi         c   2  0  k2+k-      0.    0.   0.995  1.045  $400000
   5  psi_ee      c   2  0  e+e-       0.    0.   0.200  5.000  $000008
  10  k0          v2  2  0  i+i-      20.  800.   0.470  0.530  $000000
  12  l0          v2  2  0  p+i-      20.  800.   1.090  1.140  $000000
  14  phi_det     v2  2  0  k+k1-      5.  800.   0.995  1.045  $000008
  14  phi_det     v2  2  0  k2+k-      5.  800.   0.995  1.045  $000008
  31  kshort_1    x1  2  0  i-i+       5.  800.   0.470  0.530  $100008
  32  lambda_1    x1  2  0  p+i-       5.  800.   1.090  1.140  $200008
  33  alambda_1   x1  2  0  p-i+       5.  800.   1.090  1.140  $200008
  44  phi_det_1   x1  2  0  k+k1-      5.  800.   0.995  1.045  $000008
  44  phi_det_1   x1  2  0  k2+k-      5.  800.   0.995  1.045  $000008
!
! Partial states
  52  i2i         v2  3 +1  i-i+i+     0.  800.   0.400  1.300  $002000
  61  ki          v2  2  0  k-i+       5.  800.   0.600  1.700  $002002
  62  k-2i        v2  3 +1  k-i+i+     5.  800.   0.750  1.500  $002002
  63  k3i         v2  4  0  k-i-i+i+   0.  800.   0.900  1.700  $002000
  64  k+2i        v2  3 -1  k+i-i-     5.  800.   0.750  1.500  $002002
  71  kki         v2  3 -1  k-k-i+     5.  800.   1.100  1.600  $002002
  72  kk2i        v2  4  0  k-k-i+i+   0.  800.   1.200  1.700  $002000
  86  pii         v2  3 +1  p+i+i-     0.  800.   1.200  1.700  $002000
!
recpid     0     0 fill anal   v03.00 May 06 2001  12:00 suat
name system cut   pmin pmax mdistmin mdistmax ptmin ptmax spectro logic
 e   etrd  e>0.5    0. 120.  0.       0.      0.    0.    m2      none
 i   none  none     0.   0.  0.       0.      0.    0.    any     none
 k   rich  k/i>=1   0.   0.  0.       0.      0.    0.    m2      none
 p   none  none     0.   0.  0.       0.      0.    0.    m2      none
 e1  etrd  e>0.5    0. 120.  0.0020   0.0500  0.300 2.000 vxm2    none
 k1  none  none     0.   0.  0.       0.      0.    0.    m2      none
 k2  none  none     0.   0.  0.       0.      0.    0.    any     none
 k3  none  none     0.   0.  0.       0.      0.    0.    m2mc    none
 p1  none  none   100. 600.  0.       0.      0.    0.    any     none
 p2  none  none     0.   0.  0.       0.      0.    0.    m1m2    none
*end
```

Table 5: A Sample RECON Package Table

```
noexec   filter
execute  unpack
set  on  unpack    adc cros rmh svx fers ! hist
execute  tracking
set  on  tracking  segment link fit0 silmatch silm3d guided fit ! hist
set  on  tracking  vx_radial m1_guide vx_lasd tr_seg2 tr_user ! tr_subset
set  on  tracking  m1_share            ! m1pwc s-y hit share
set  cut tracking  segment         0   ! all spectrometers on in track_segment
set  cut tracking  ptm1       0.7371   ! use fixed spectrometer pt_kicks
set  cut tracking  ptm2       0.8285   ! use fixed spectrometer pt_kicks
set  cut tracking  trajectory parabolic ! parabolic trajectory as a default
prog     tracking  1mrun.tseg
set  cut tracking  tag_win       0.01 ! cut for hsdcollect bm_HST window in cm
set  cut tracking  evt_tim       7.9  ! event time cut
exec     photon
set  on  photon    full m1_pht m2_pht m3_pht
set  cut photon    min_count  4.        ! pass11 5.
set  cut photon    min_energy 1.5       ! pass11 2.
exec     partid
set  on  partid rich btr etr ! etr_track  btr_hist
set  on  partid ric_lambda ric_phi
exec     vertex
set  on  vertex vtx2   err2 secint   prim  sec
set  cut vertex prong            5
set  cut vertex vtxd           4.0
set  cut vertex vtx2           9.0
set  off vertex secint
exec     recon
set  on  recon  ntuple hist
set  cut recon  tgt_rec       0.05
set  cut recon  pscale        1.0000  ! pass11_11_v1
set  cut recon  cand_cpri     5.0
exec     user
set  on  user   hist !  DBG
set  cut user   report        2000
in   ds_defaults.cmd
disk in  reset
in  disk.files
ana 0
exit
```

Table 6: A Sample SOAP Control File

```
exec files.kumac.bm

nt/cut  $10  (tgt.ge.6.and.tgt.le.10).and.tpid.gt.0.
nt/cut  $41 pidbm.gt.0.and.btr.lt.4
nt/cut  $43 mod(int(tpid/1000.),10).ge.mod(int(tpid/100.),10)
nt/cut  $44 mod(int(tpid/1000.),10).ge.mod(int(tpid/10.),10)
nt/cut  $45 mod(int(tpid/100.),10).ge.mod(int(tpid/10.),10)
1d      10 '[p]^+!  p'  32 0. 320.
2d      21 'p?t! vs x?F!  [p]^+!' 50 0 0.5 50 0 2.5
nt/proj 10 210.p.for $2.and.pz>15.
nt/proj 11 210.p.for $2.and.pz<-15.
div 10 11 1 ! ! e; hi/copy 1 12 '[p]^+!/ [p]^-! vs p'; hi/del 1
nt/proj 13 210.p.for $3.and.pz>30.
nt/proj 14 210.p.for $3.and.pz<-30.
div 13 14 1 ! ! e; hi/copy 1 15 'K^+!/ K^-! vs p'; hi/del 1
nt/proj 16 210.p.for $4.and.pz>50.
nt/proj 17 210.p.for $4.and.pz<-50
div 16 17 1 ! ! e; hi/copy 1 18 'p&^-!/ p vs p'; hi/del 1
nt/proj 21 210.pt%xf $2.and.pz>15.
nt/proj 22 210.pt%xf $2.and.pz<-15.
div     21 22 1 ! ! e; hi/co   1  23 'p?t! vs x?F!  [p]^+! / [p]^-!' ; hi/del 1
prox    21; proy 21; hi/proj 21
prox    22; proy 22; hi/proj 22
hi/co   21.prox 24 'x?F!  [p]^+!'
hi/co   22.prox 25 'x?F!  [p]^-!'
```

Table 7: A Sample KUMAC File Used for Analysis

The output of SOAP was stored in the format compatible with the Physics Analysis Workstation (PAW) software. This software is used to make specific cuts, observe corrections, and histogram the results. This was be done in two different ways: calling a user routine written in Fortran or using kumac file which instructs PAW software to perform specific actions or the combination of both ways to perform a user specific actions on data outputs. An example kumac files is shown in Table 7.

CHAPTER IV

DATA COLLECTION AND ANALYSIS

In this chapter we will describe the data sample used for the charged particle production ratios, the steps of the data analysis, the correction applied the final data sample, and the systematic error analysis. Then we will present the results.

4.1 The Data Collection

The main goal of this study is to find the production ratios of charged particles with minimum trigger bias. For this reason we have analyzed only so called "Beam Trigger" runs. The beam trigger was made using three beam scintillator counters (S1, S2 and S3) and three veto scintillator counters (VH1, VH2 and VH3) with the following logical combination : $S1\ \overline{VH1}\ S2\ \overline{VH2}S3\ \overline{VH3}$ where the veto scintillator counters restricted the beam to $2 \times 2\ cm^2$ size. This combination assured that all of the beam particles that fire the trigger go through all the planes of the beam spectrometer. This provided a uniform acceptance for the positive and negative tracks since there was no other requirements on the beam trigger such as number of tracks in M2 spectrometer or positive multiplicity on the M2 scintillating hodoscopes. The raw data sample included set of negative beam trigger runs for negative (Σ^-/π^-) beam particles and another set of runs for positive (p/π^+) beam particles.

The raw data sample used for the charge particle production ratios was analyzed using the SELEX Offline Analysis Package (SOAP) which handled the event unpacking, track and vertex reconstruction, and particle identification. The total of

400 beam trigger runs were analyzed, and after all the cuts were applied, a total of 512 K events from negative runs and 150 K events from positive runs made it to the final data sample. Starting from 100%, applying the cuts reduced the data sample to a 5% expected for a target with 4.2% of an interacting length.

4.2 The Analysis Steps

The analysis was done in three stages. The first stage was the longest one since it involved reading all the raw data files from tapes and transferring them to the local disks to analyze. This stage was called "strip" stage. It was the first pass over the complete raw data sample and was done with minimum set of requirements to reduce the amount of data to be handled by the second stage of the analysis. An event passed this stage if it met the all of the following conditions:

- The correct trigger bit was set,
- The event could be unpacked without errors,
- The beam, vertex and M2 spectrometers had a minimum number of hits,
  - beam silicon: at least 7 hits needed for one single track
  - vertex silicon: at least 20 hits for two tracks
  - M2 PWC: at list 25 hits for the two tracks
- There were at least two M2 tracks or the M1-M2 track,
- At least one beam track could be constructed.

The first stage reduced the data sample 90% . The reduced data sample was re-analyzed in the the second stage.

The purpose of the second stage was to extract the observed number of charged particles (π, K, p). At this stage, stripped raw data files were re-analyzed with the following requirements: Loop over all beam track segments found in the beam spectrometer and select the correct beam track segment, i.e. the one that had hits on the HSD stations, thus assuring that the beam segment is in time with the trigger. This was done a follows: The beam track was extrapolated back to the z position of the beam hardware scattering trigger (HST) silicon planes. If there was a hit on one of the HST planes within an acceptance window the hit got assigned to the beam segment. Then a re-fitter routine is called to re-fit the beam segment taking into account the additional hit information from the HST planes. If such an event found than following information about event written out to ntuples which is one way to store the data for further analysis with PAW software.

- run number to separate positive and negative runs,
- number of tracks per event and charm target assignment,
- x and y position and three component of beam track momentum with χ^2 of the momentum fit,
- x an y position of the charged tracks and 3 components of their momentum,
- particle identification information for both beam and secondary tracks

Figure 18, 19 and 20 show the histograms of ntuple variables stored for further analysis. For the beam tracks x, y and z component of the momentum with momentum fit χ^2 and, x and y slopes are stored (Figure 18). For the secondary tracks again three components of the momentum with momentum fit χ^2 and x and y slopes were stored (Figure 19). Figure 20 shows the variables stored in ntuples for beam and

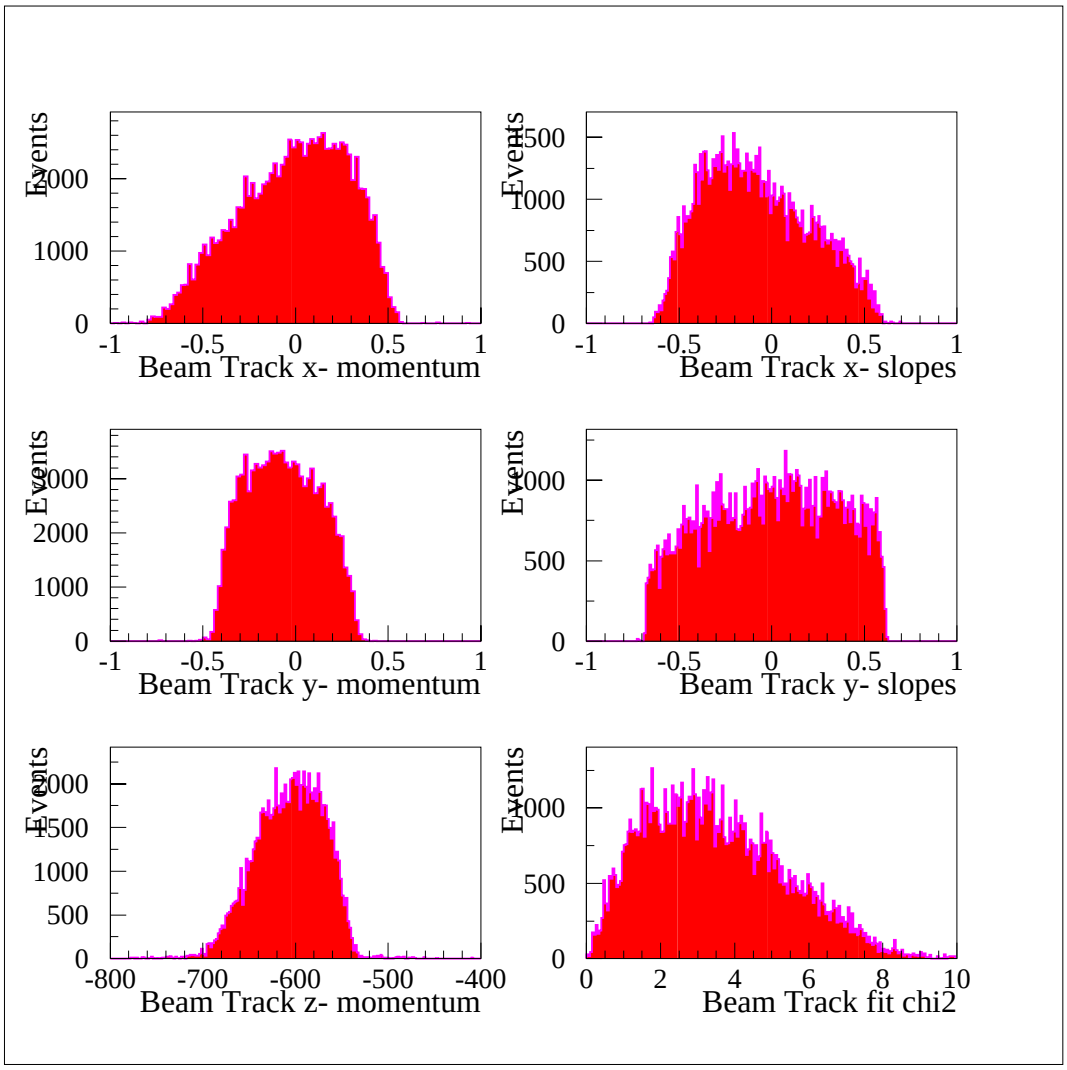

Figure 18: Stored Beam Track Ntuple Variables

secondary tracks particle identification information, track type and assigned primary targets.

The third stage of the analysis involved applying the particle identification corrections to find the true number of charged particles from the measured charged particles. This step involved producing a particle identification matrix and solving

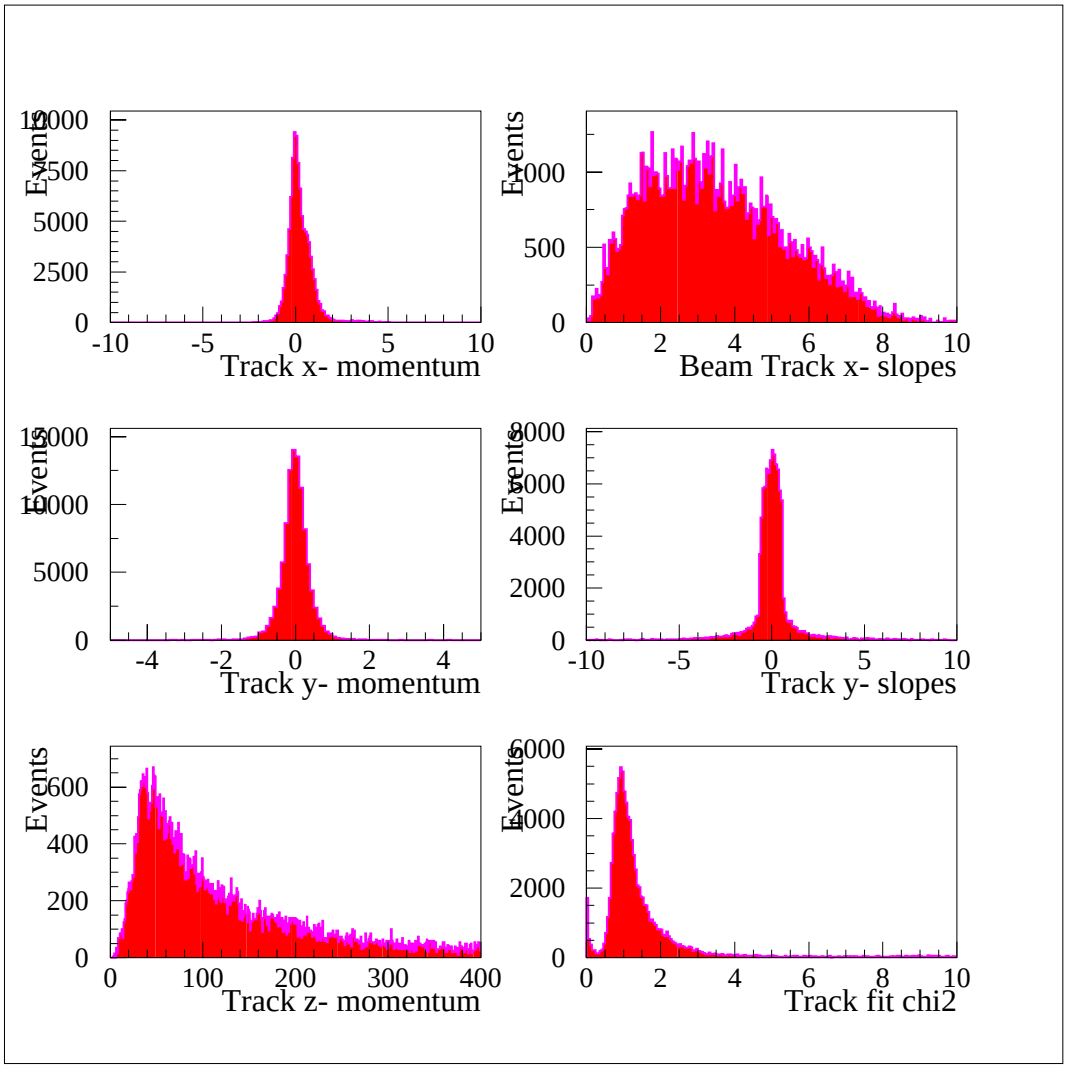

Figure 19: Stored Secondary Track Ntuple Variables

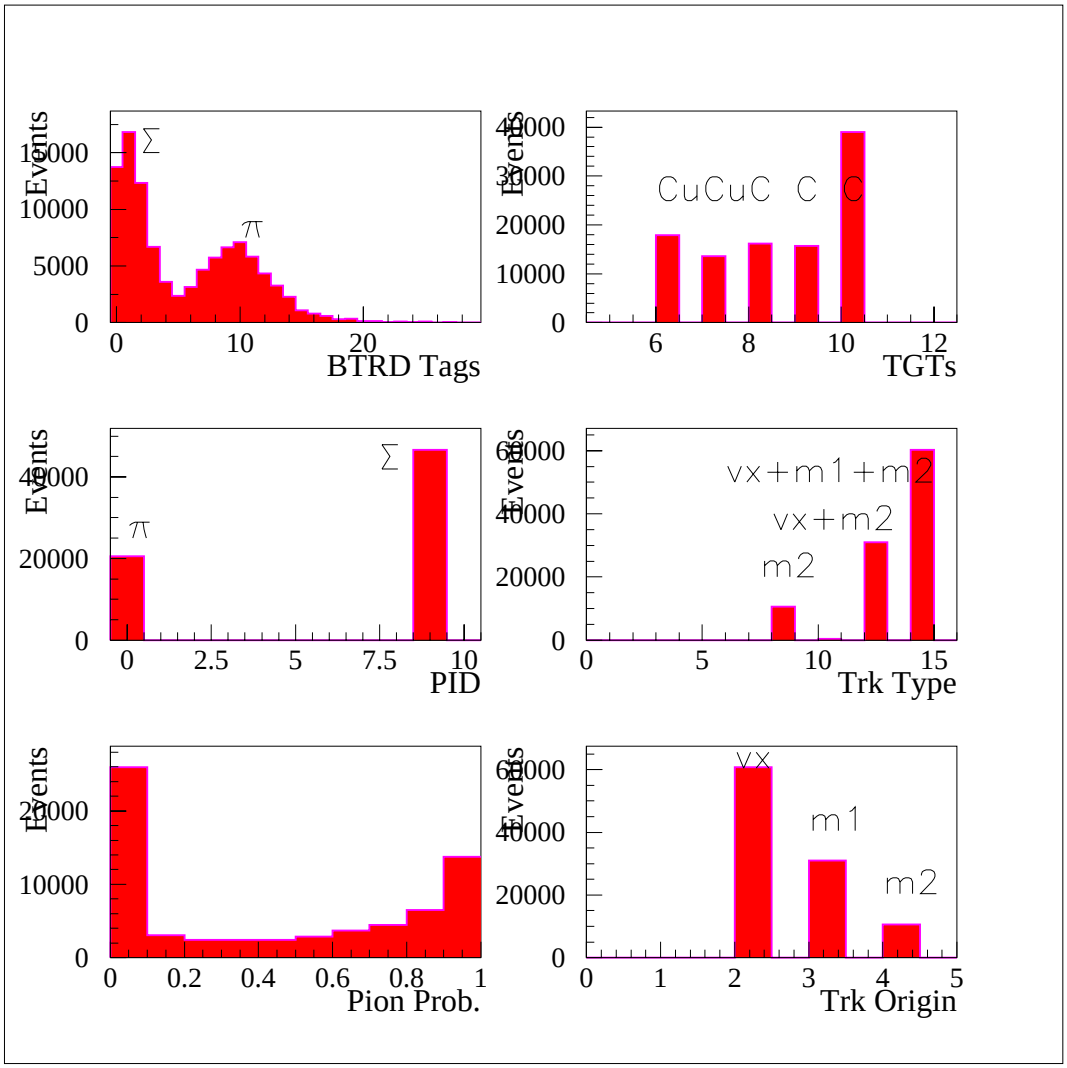

Figure 20: Stored Particle Identification and Track Type Ntuple Variables

the linear equation to get the true charged particle spectra. For this, we have analyzed total of 10 M interactions with modified the particle identification definitions. Since we were looking for the particle identification efficiencies of the RICH we had to calibrate the process by using the 2 prong decays without using RICH identification information. This process is explained in section 4.3.1.

We also check for acceptance differences for positive and negative tracks to make sure that our data was not charge biased. For this we used the same data sample we used for the particle identification corrections with modified RECON construction definitions. This process is explained in section 4.3.2

We also investigated the particle decay and target sizes as corrections to the charged particle production ratios. The details are explained in section 4.3.3 and section 4.3.4 .

4.3 The Correction to Data Sample and Error Analysis

The corrections mentioned above were applied to final data sample and explained in the following sections. The biggest error to the particle production ratios came from the unfolding the particle identification efficiencies of the ring imaging Cherenkov counter.

4.3.1 Particle Identification Corrections

One of the most important corrections to the charge particle production ratios come from particle identification efficiencies. The ring imaging Cherenkov counter (RICH) was used as the primary detector to identify the π, K and p. However, the RICH is not 100% accurate; it could identify a π as π or misidentify it as a K or p. Similarly, it could identify a K as K or mis-identify the K as a π or p; also it could identify a p as p or misidentify p as a K or π. To find the true number of π, K

and p from the observed (identified) number of π, K and p required unfolding these mis-identifications by the ring imaging Cherenkov counter. The steps for unfolding these (mis-)identifications as follows: First using the reconstruction software package (RECON) with modified reconstruction Table 8, we constructed $K_s \rightarrow \pi^+\pi^-, \Lambda \rightarrow p\pi^-$, and $\Phi \rightarrow K^+K^-$ without using any particle identification information from the RICH.

```
recdf      0     0 fill anal v03.00 May 06 2001  12:00 suat ! K/pi ratio recon list
!
  id  name       from pr q  pid   ls_min ls_max mass_min mass_max   out ! frac [%]
! Strange states
   1 kshort       v2  2  0  i-i+       0.    0.   0.470  0.530  $100001 ! 01 1.41
   2 lambda       v2  2  0  p+i-       0.    0.   1.090  1.140  $200001 ! 02 0.33
   3 alambda      v2  2  0  p-i+       0.    0.   1.090  1.140  $200001 ! 03 0.07
   4 phi           c  2  0  k+k1-      0.    0.   0.995  1.045  $400001 ! 04 8.21
   5 phi           c  2  0  k1+k-      0.    0.   0.995  1.045  $400001 ! 05 4.36
*end

*recpid     0     0 fill anal   v03.00 May 06 2001  12:00 suat ! K/pi ratio recon list
name system cut   pmin pmax mdistmin mdistmax ptmin ptmax spectro logic
 i   none  none     0.   0.  0.       0.      0.    0.    any     none ! not non-pi if in rich
 k   rich  k/i>=1   0.   0.  0.       0.      0.    0.    m2      none ! default Kaon
 p   none  none     0.   0.  0.       0.      0.    0.    m2      none ! default proton
 k1  none  none     0.   0.  0.       0.      0.    0.    m2      none ! any track
*end
```

Table 8: The Modified Reconstruction (RECON) List

The RECON package simply took 2 opposite charged tracks coming from same vertex, then calculated the masses using track information. The masses produced without using the RICH identification information is shown in Figure 21.

Afterward, we went back and asked RICH to identify these particles on an event by event basis. For example, in case of $\Lambda^0 \rightarrow p\pi^-$, we know that first track should be a p and the second track should be a π. If the RICH identified the first track as a proton this gave the efficiency of correctly identifying a proton as a proton ϵ_p^p, but if

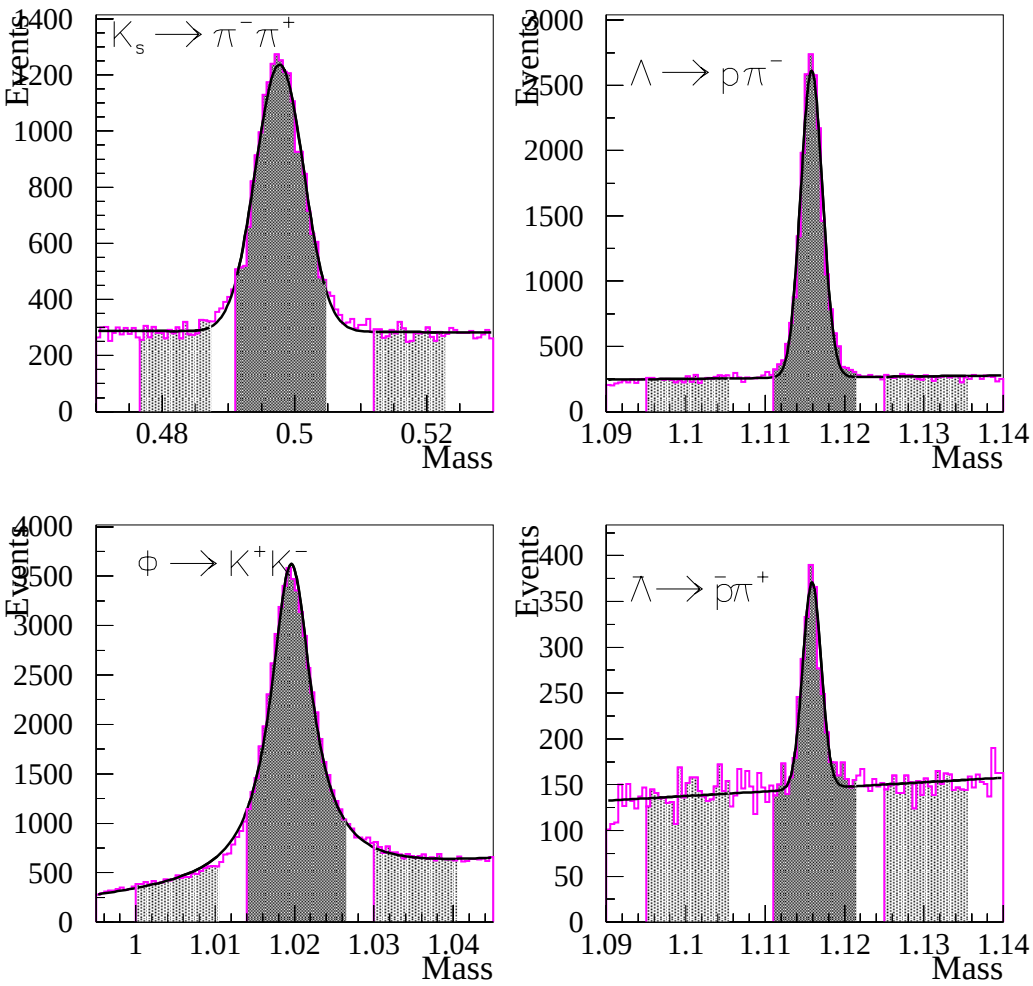

Figure 21: RECON Constructed Masses Without RICH Identification

the RICH identified the first track as a kaon it gave the inefficiency of misidentifying the proton as a kaon ϵ_p^K or if the RICH identified the first track as a pion it gave the inefficiency of misidentifying a proton as a pion ϵ_p^π.

In the Figure 22, the left top histogram shows the constructed Λ mass by RECON without using the particle identification information from the RICH detector. To calculate the efficiency of identifying the proton as a proton first we apply the side-band subtraction technique to the mass signal using the shaded areas. This assured that the momentum projection of the events in this side band subtracted mass plot would not be effected by background events. Then the other histograms were produced projecting the momentum of the side band subtracted Λ events into one of the three histogram by using the RICH particle identification information as described above. After filling the histograms, we fitted each momentum versus efficiency histogram with a polynomial function. For example, in the case of the Λ following functions for efficiencies were found:

$\epsilon_p^p(p) = 0.90149 + 0.20285E-022 \times p - 0.13392E-04 \times p^2 + 0.19473E-07 \times p^3$ for identifying a proton as proton,

$\epsilon_p^K(p) = -0.21496E-02 + 0.18245E-03 \times p - 0.17765E-05 \times p^2 + 0.76057E-08 \times p^3$ for identifying a kaon as proton and,

$\epsilon_p^\pi(p) = 0.22750 - 0.86997E-02 \times p + 0.11678E-03 \times p^2 - 0.66852E-06 \times p^3 + 0.16957E-08 \times p^4 - 0.15351E-11 \times p^5$ for identifying a pion as proton. Thus for a given momentum value it was possible to use the fit functions to get the efficiency or inefficiency for (mis-)identifying a proton. The summation of these three functions should be equal or less than unity. Thus we had to propagate the error on this summation to particle production ratio measurements. This error was the most significant error in our analysis. Propagation of the error was calculated to be less than

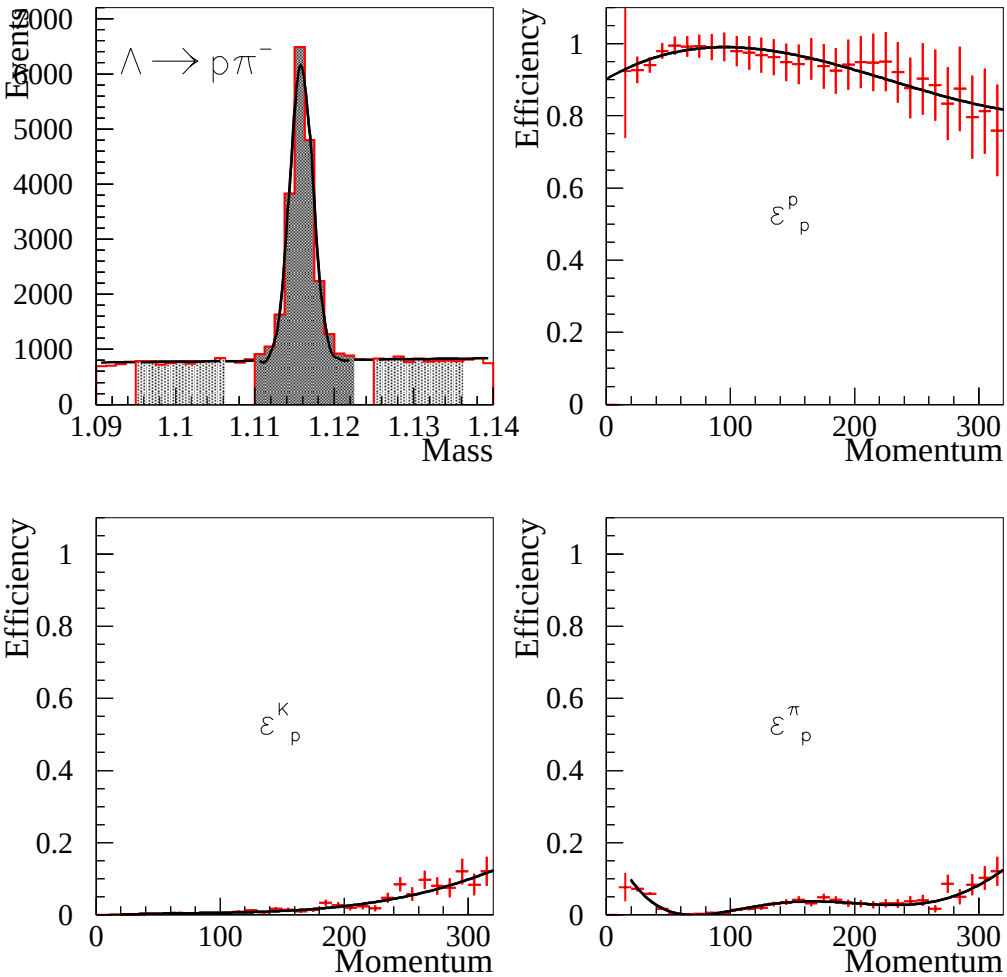

Figure 22: RICH Particle Identification for $\Lambda^0 \to p\pi^-$

10% for all the secondary particles momentum range. The same analysis technique was applied to $K_s \rightarrow \pi^+\pi^-$ to find the efficiency of correctly identifying the pion as a pion ϵ_π^π, the efficiency of misidentifying the pion as a kaon ϵ_π^K, and the efficiency of misidentifying the pion as a proton ϵ_π^p (Figure 23). Similarly, we used $\Phi \rightarrow K^+K-$ to find the efficiency of misidentifying the kaon as a pion ϵ_K^π, the efficiency of correctly identifying a kaon as a kaon ϵ_K^K, and the efficiency of misidentifying the kaon as a pion ϵ_K^π (Figure 24).

These efficiencies translated into a 3×3 particle identification efficiency matrix. From the measured charged particles spectra I_π, I_K and I_p of identified particles we obtained true number S_π, S_K and S_p of charged particle by solving the system of equations:

$$\begin{pmatrix} I_\pi \\ I_K \\ I_p \end{pmatrix} = \begin{pmatrix} \epsilon_\pi^\pi & \epsilon_\pi^K & \epsilon_\pi^p \\ \epsilon_K^\pi & \epsilon_K^K & \epsilon_K^p \\ \epsilon_p^\pi & \epsilon_p^K & \epsilon_p^p \end{pmatrix} \begin{pmatrix} S_\pi \\ S_K \\ S_p \end{pmatrix}$$

4.3.2 Acceptance Corrections

Another kind of correction we had to make when measuring the charged particle production ratios was to correct for the charge asymmetry of the apparatus for positive and negative tracks. To do this we have reconstructed $\Phi \rightarrow KK$ using RECON package in two different ways. First we identified a K^- and search for a positive second track coming from same vertex as K^- that made a $\Phi \rightarrow K^-(any)^+$. Second, we identified a K^+ and search for a negative second track that coming from the same vertex that made the Φ with the hypothesis $\Phi \rightarrow K^+(any)^-$. If the acceptance of the apparatus was charge symmetric then the number of constructed Φ's would be equal for the both ways of reconstruction. Figure 25 shows the reconstructed masses

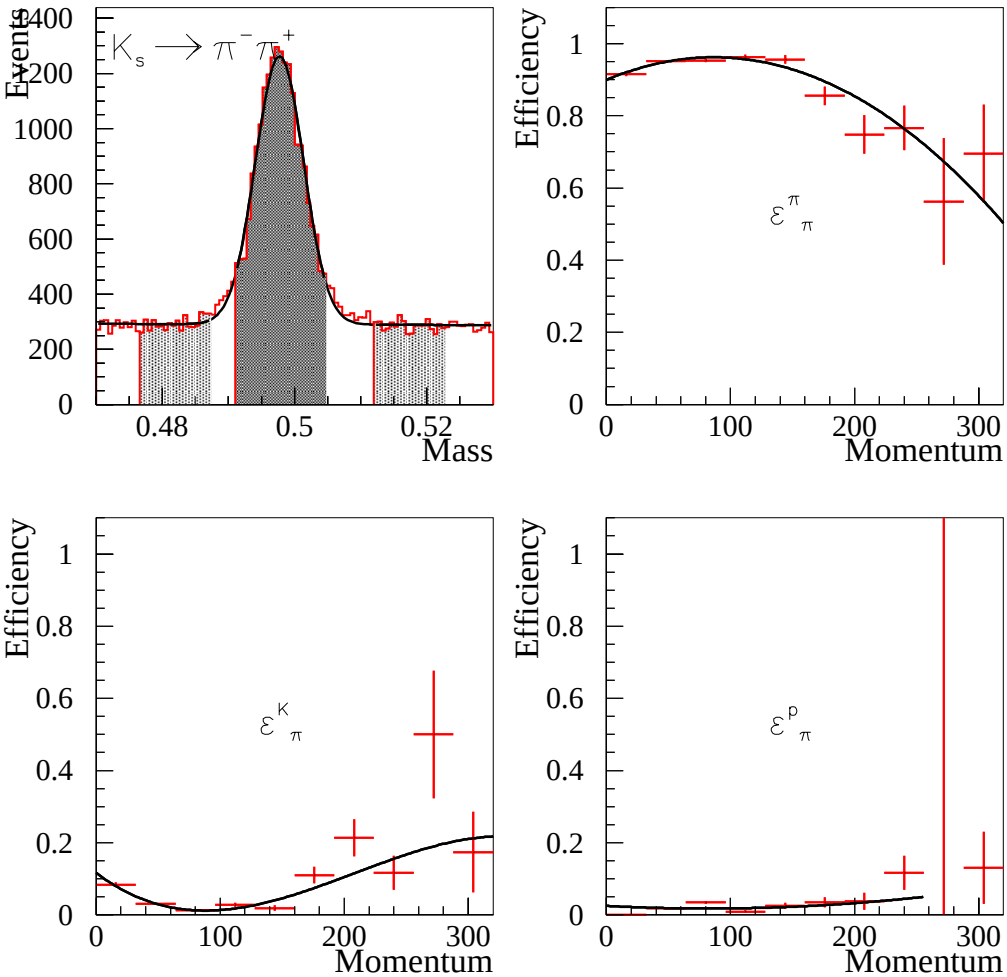

Figure 23: RICH Particle Identification for $K_s \to \pi^+\pi^-$

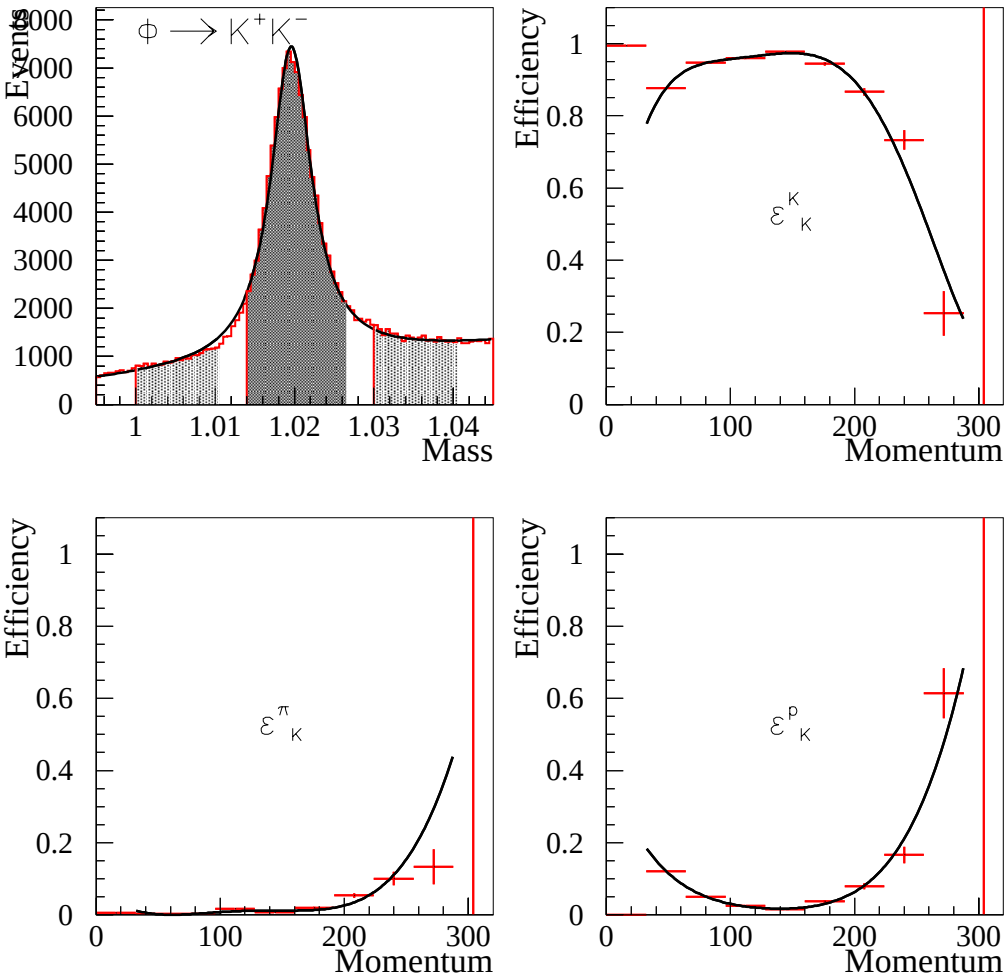

Figure 24: RICH Particle Identification for $\Phi \to K^+K^-$

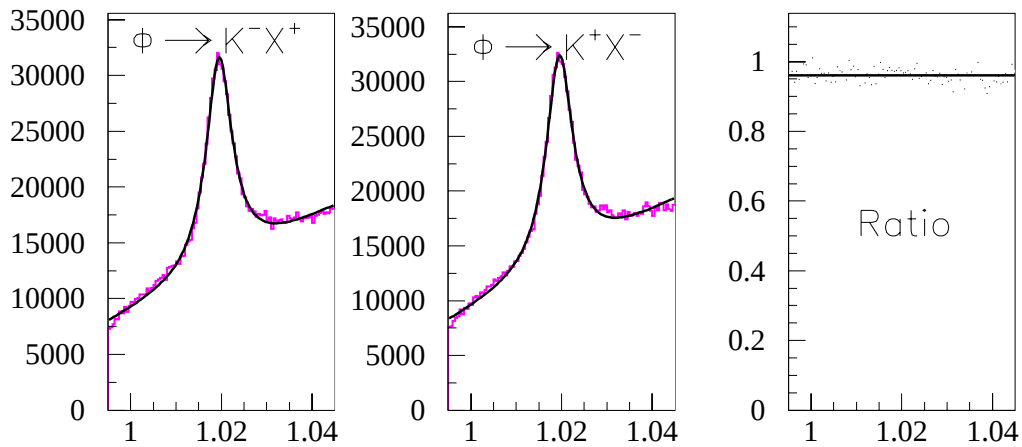

Figure 25: Acceptance Correction for Positive and Negative Tracks

with the two method and the ratio of the two methods which shows that SELEX was symmetric for oppositely charged tracks.

4.3.3 Corrections for the Particle Decays

Since pions and kaons were tagged by the ring imaging Cherenkov counter, an accurate determination of the decay corrections was relevant for precise measurement of the K/π production ratio where other sources of systematic errors are strongly reduced. The γ factor of the π and K with an average momentum of range of 30-100GeV/c could be found in the following way:

$$\gamma_\pi \approx \frac{p}{m_\pi c} \approx 107 - 1792$$

and

$$\gamma_K \approx \frac{p}{m_K c} \approx 61 - 506.$$

The mean distance that these π and K traveled before they decayed were accordingly

$$l_\pi = \gamma_\pi c\tau \approx 900 - 14000m$$

and

$$l_K = \gamma_K c\tau \approx 200 - 2000m$$

These decay lengths were much further than the acceptance of the ring imaging Cherenkov counter so that there was no need to make any corrections for the particle decay.

4.3.4 Corrections for the Target Size

SELEX experiment had 5 segmented targets each with less then 1% interaction length. Thus, corrections for target size and shape were irrelevant for the SELEX experiment. The particle production ratios were not corrected for the target shape or the target size. However, the particle production yield for individual targets had to be checked also. As shown in Figure 7 the yields for the individual target were comparable within experimental errors. There was no correction applied for the individual target yields.

4.4 Systematic Error Analysis

Imposing analysis cuts may introduce a systematic error into measured charged particle production ratios. This happens if there is a systematic dependence of the charged particle production ratios on the variables used in the cut. If the charged particle production ratios for the rejected events and for the events used in the measurement are the same, imposing the analysis cuts will not effect the measured values. There were several cuts applied which could be a source of the systematic errors.

4.4.1 Systematic Error in the Efficiency and Acceptance Correction

The difference of reconstruction efficiencies between negative and positive tracks was estimated to be less than 2%, since we apply the cuts equally for the both positive and negative tracks. This systematic error was negligible.

4.4.2 Systematic Error in Momentum Determination

An other source of the systematic error was the determination of the beam track and secondary tracks momentum. In the analysis of the particle production ratiothe beam momentum was measured on an event by event basis and x_F and p_t^2 were calculated using the measured momentum values. The precision of determining the beam momentum was less than 1%. Since the error in particle (mis-)identification error was much bigger than this error, the systematic error of momentum determination was negligible.

4.4.3 Systematic Error in Beam Particle Identification

The separation of the Σ, π and proton was made according to the activated number of planes in beam transition radiation detector. For example for Σ and p the number of activated planes in beam transition radiation detector was set to be less than 4 and for π was more than 6. The contamination for positive and negative beam trigger runs were calculated and given in the Table 9. The systematic error coming form the identification of the beam particles was again small and negligible.

Beam	Baryon Fraction from BTRD	Ξ^- fraction	Σ^- fraction	Σ^+ fraction
Σ^-	49.92%	1.14%	48.78%	-
p	94.56%	-	-	2.87%

Table 9: The Contamination of the Beam Particles

4.4.4 Systematic Error in Binning

The last source of the systematic error investigated was the binning scheme used on the data. Initially, the bin size was determined by optimizing the data size in each bin. Then, the bin sizes were separately, systematically varied and the change in particle production ratios were observed. For variables which the particle production ratios showed a dependence (x_F and p_t^2) the binning scheme was determined by the desire to have the statistical errors for each bin to be roughly equivalent. The systematic error coming from the binning in x_F and p_t^2 was calculated to be less than 5% depending over the momentum range. Thus 10 bins in x_F distribution and 10 bins in p_t^2 distribution were chosen to present the results of particle production ratios.

4.5 Charged Particle Ratios for Σ^-, π^- and p Beams

In this section we will present the charged particle production ratios for three different beam particles versus momentum, Feyman x_F and transverse momentum squared (p_t^2) . For all the production ratios versus momentum plots the momentum ranges from 0 to 200 GeV which correspond to $x_F \approx 0.3$. In this section there are a set of plots for each type of beam particles.

Figures 26, 27, 28 and 29 are the charged particle ratios for various distributions of the Σ^- beam; Figures 30, 31, 32 and 33 are the charged particle ratios for

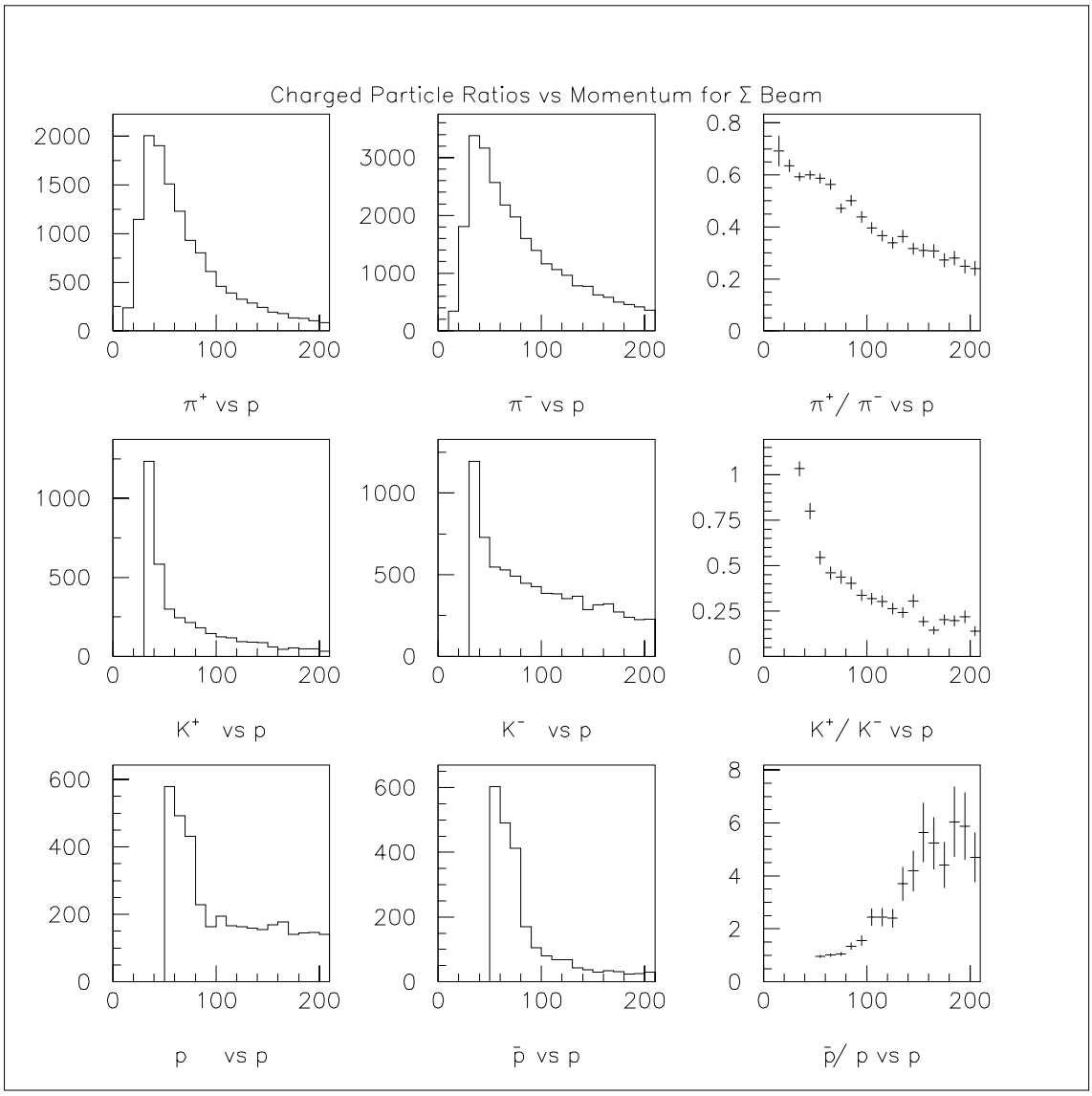

Figure 26: π^+/π^-, K^+/K^- and $\overline{p}/p$ Ratios Versus Momentum for Σ^- Beam

similar distributions of the π^- beam and Figures 34, 35, 36 and 37 are the charged particle ratios for similar distributions of the proton beam.

Figure 26 shows the distribution of π^+/π^-, K^+/K^- and $\overline{p}/p$ versus momentum of the Σ^- Beam. In the rightmost column of histograms are the ratios of two histograms to the left in each case.

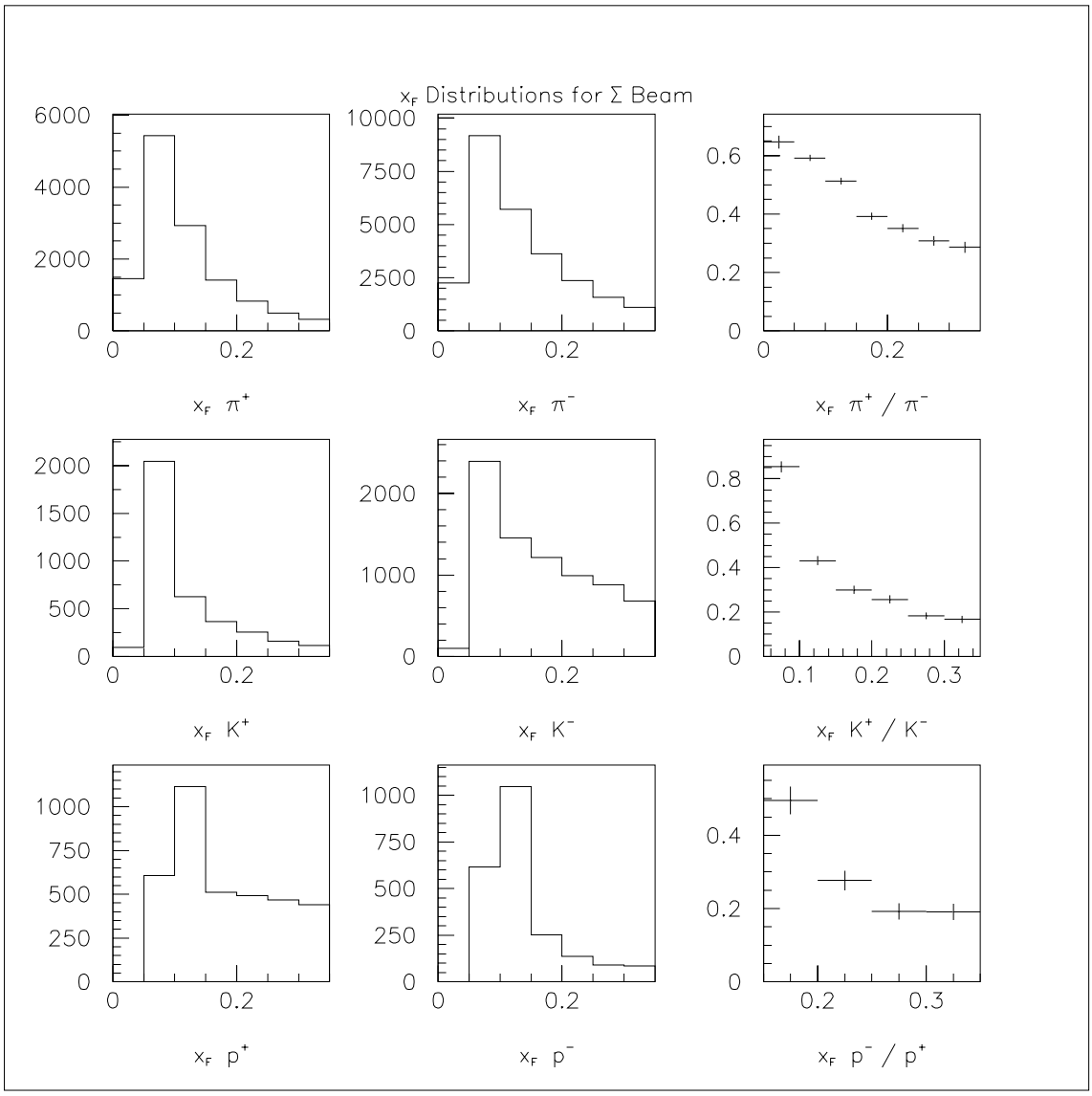

Figure 27: π^+/π^-, K^+/K^- and $\overline{p}/p$ Ratios Versus x_F for Σ^- Beam

Figure 27 shows the x_F distribution of π^+/π^-, K^+/K^- and and $\overline{p}/p$ for the Σ^- beam. The first three entries at the top from left to right are the x_F distributions of π^+ and π^- and the ratio of the two histograms. The corresponding x_F distributions for K and p are also shown. The important graphs are the ratios as the normalization of the individual graphs to the left are unknown.

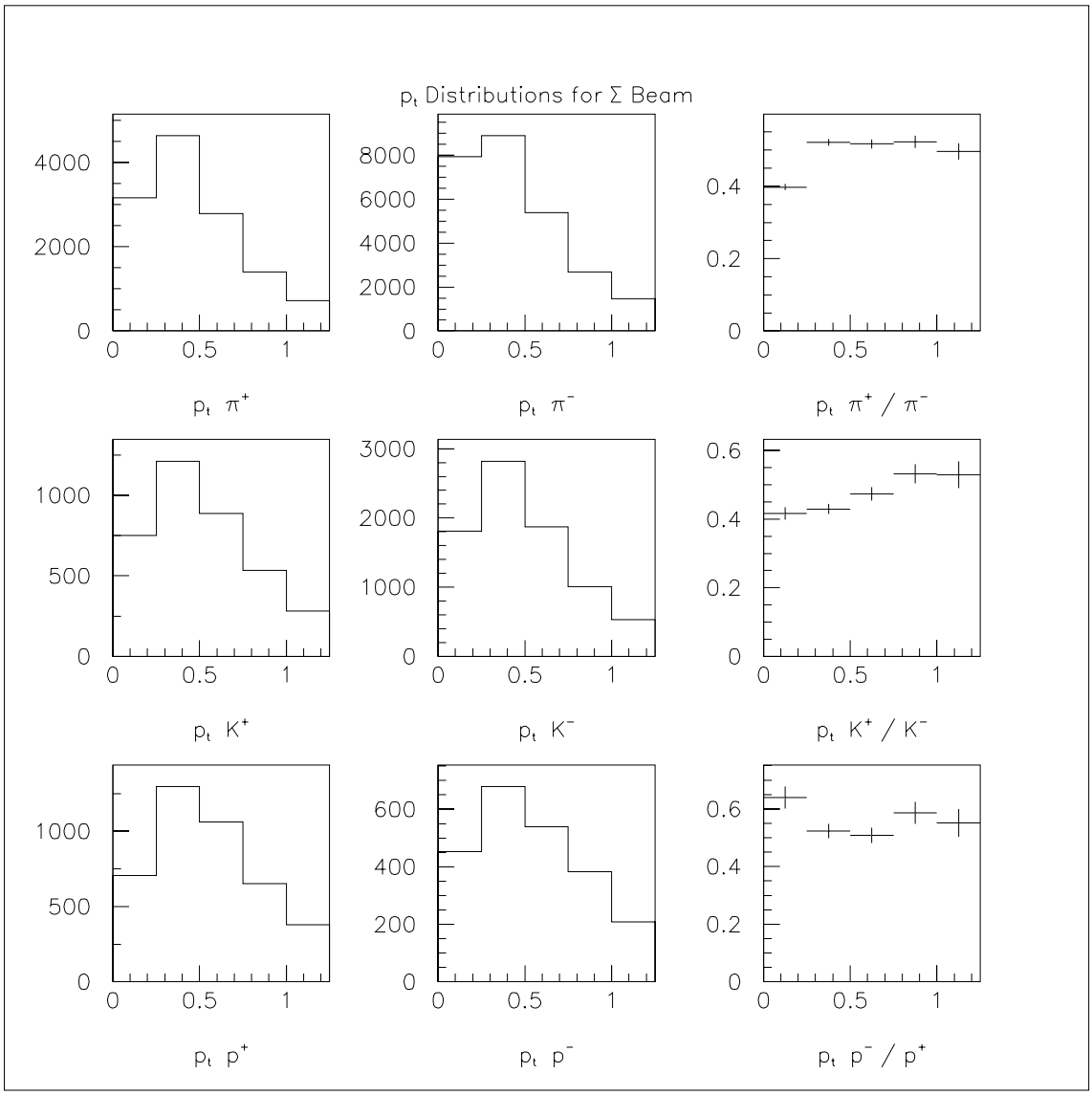

Figure 28: π^+/π^-, K^+/K^- and $\overline{p}/p$ Ratios Versus p_t^2 for Σ^- Beam

Figure 28 shows the p_t^2 distribution of π^+/π^-, K^+/K^- and and $\overline{p}/p$ for the Σ^- beam.

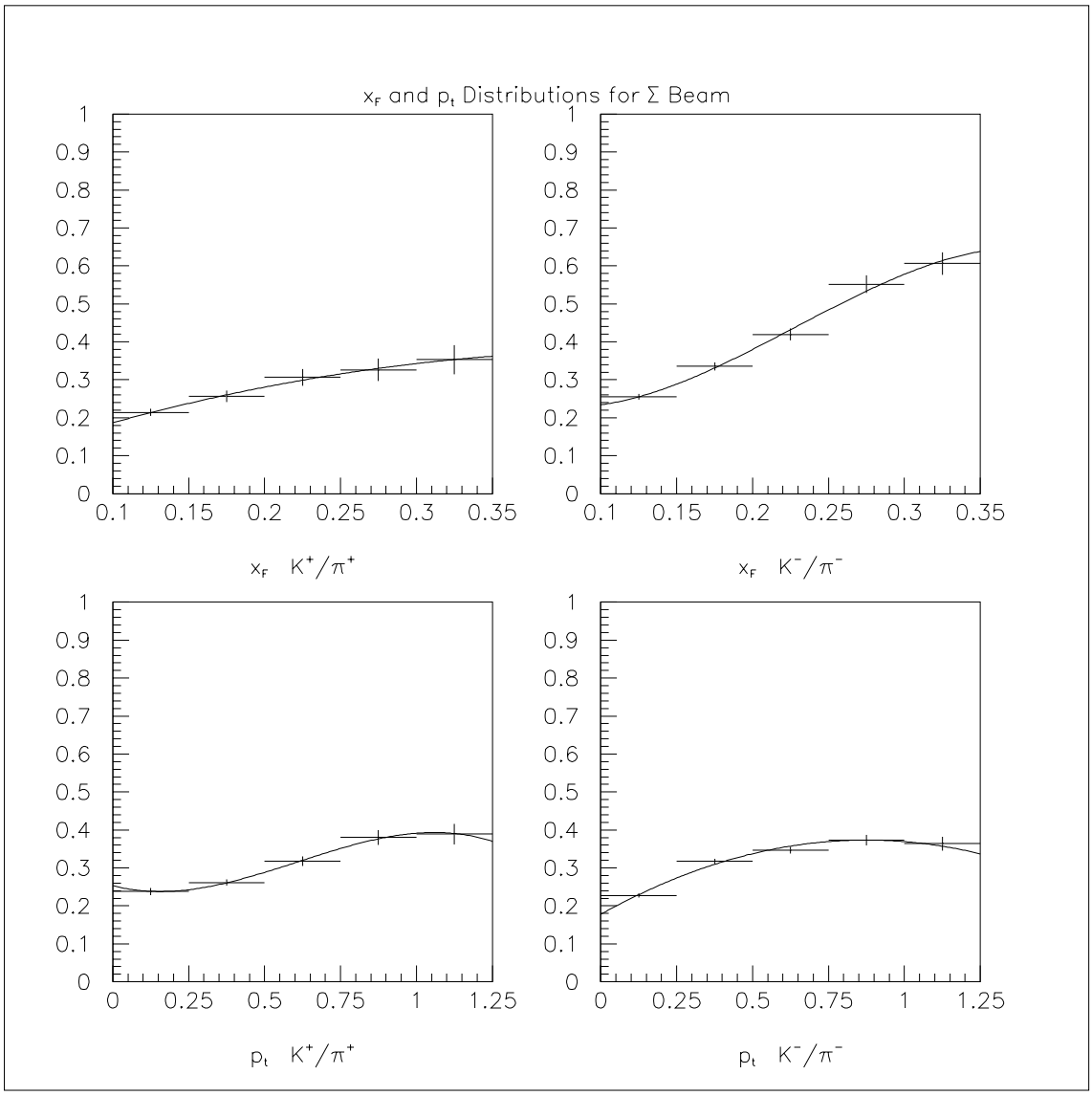

Figure 29: $K^{\pm}/\pi^{\pm}$ Versus x_F and p_t^2 for Σ^- Beam

The top two histograms in Figure 29 are the x_F distribution of $K^{\pm}/\pi^{\pm}$ and the bottom two are the p_t^2 distribution of the same production ratios for the Σ^- beam.

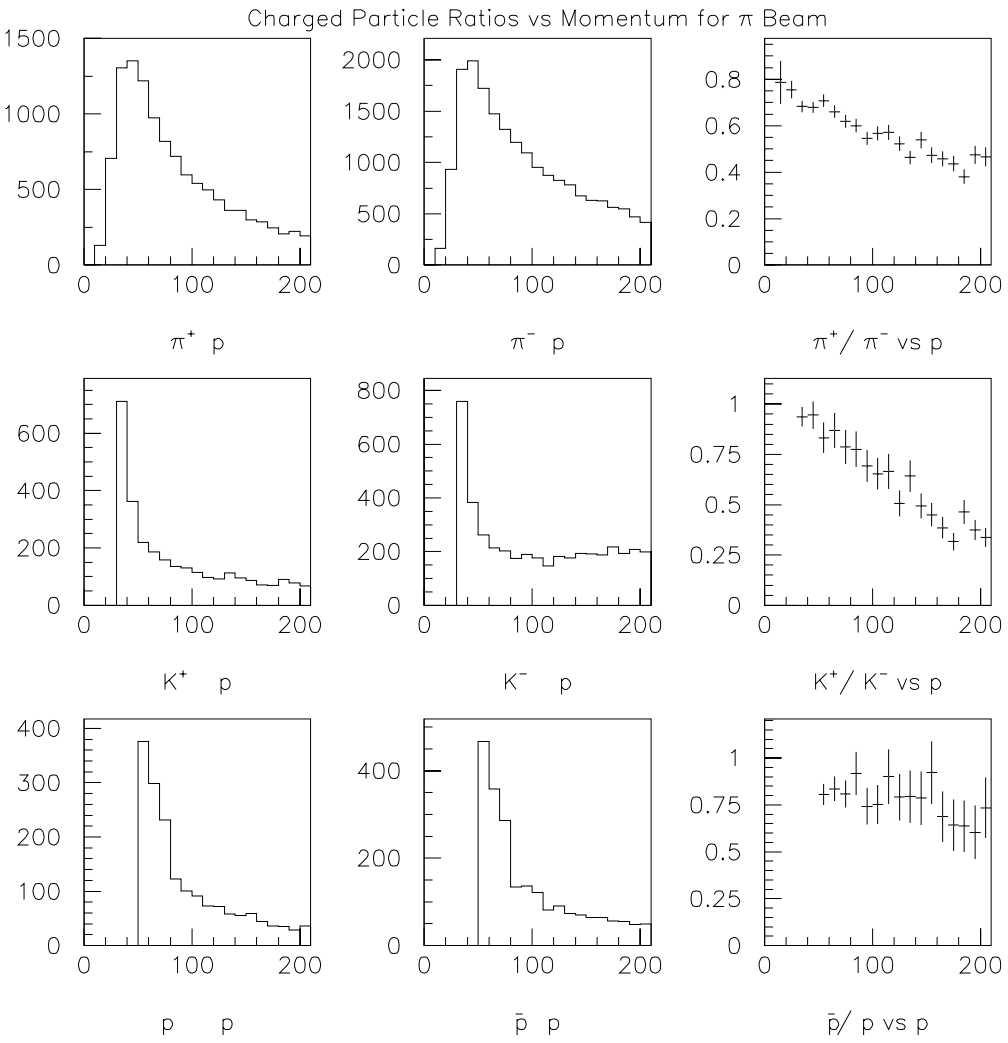

Figure 30: π^+/π^-, K^+/K^- and $\overline{p}/p$ Ratios Versus Momentum for π^- Beam

Figure 30 show the momentum distribution of π^+/π^-, K^+/K^- and $\overline{p}/p$ for the π^- Beam. The first three entries at the top from left to right are the momentum distributions of π^+ and π^-, and the ratio of the two histograms. The same type of histograms for the momentum distributions for K and p are also shown.

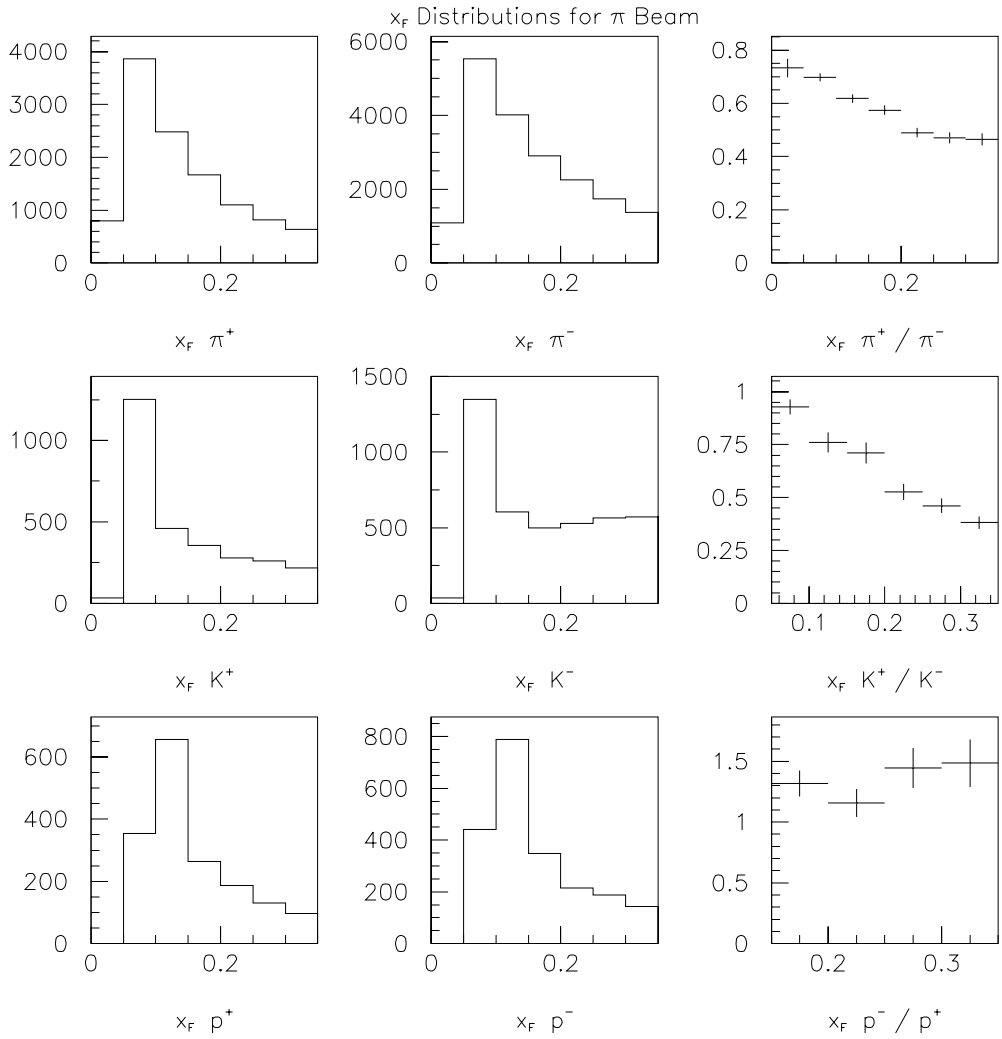

Figure 31: π^+/π^-, K^+/K^- and $\overline{p}/p$ Ratios Versus x_F for π^- Beam

Figure 31 shows the x_F distribution of π^+/π^-, K^+/K^- and and $\overline{p}/p$. The first three entries at the top from left to right are the x_F distributions of π^+ and π^- and the ratio of the two histograms. The lower two rows of the histogram present similar results for K and p.

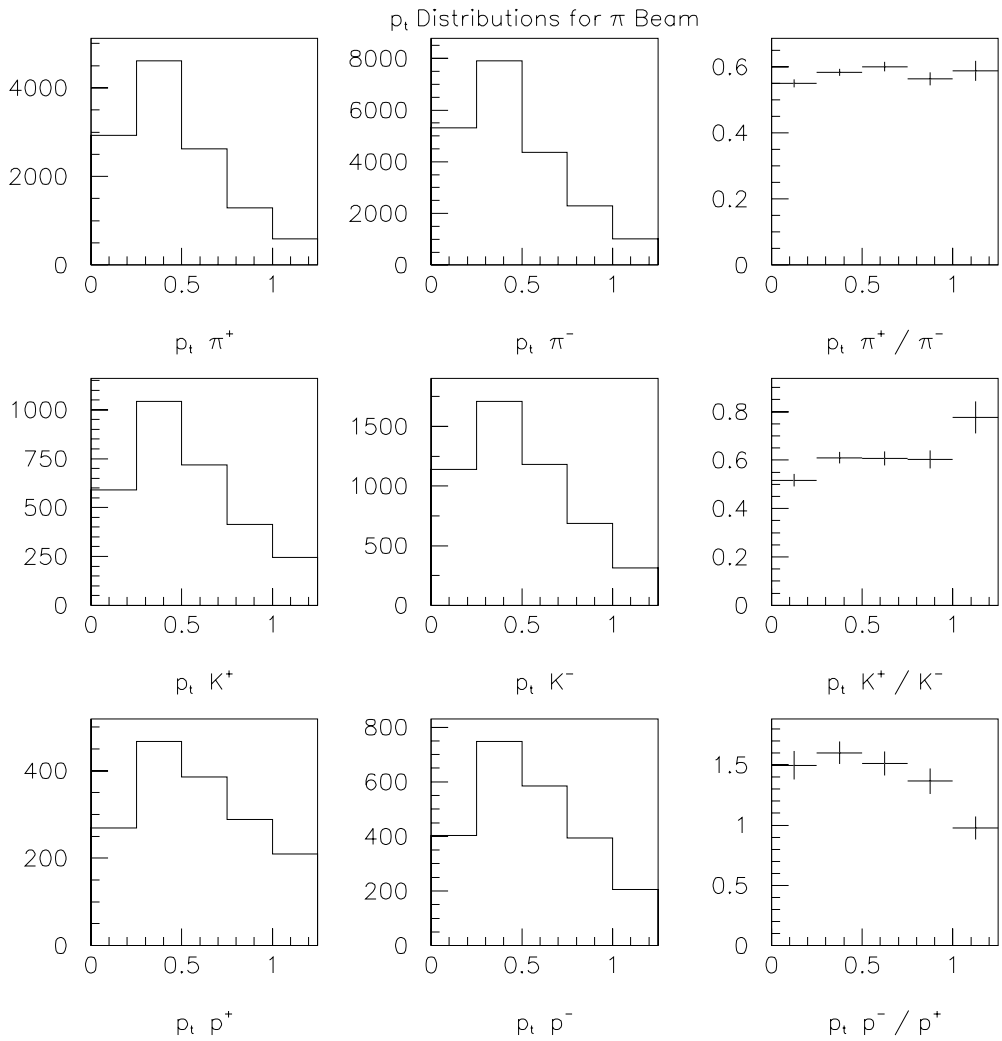

Figure 32: π^+/π^-, K^+/K^- and $\overline{p}/p$ Ratios Versus p_t^2 for π^- Beam

Figure 32 shows the p_t^2 distribution of π^+/π^-, K^+/K^- and and $\overline{p}/p$ for the π^- beam.

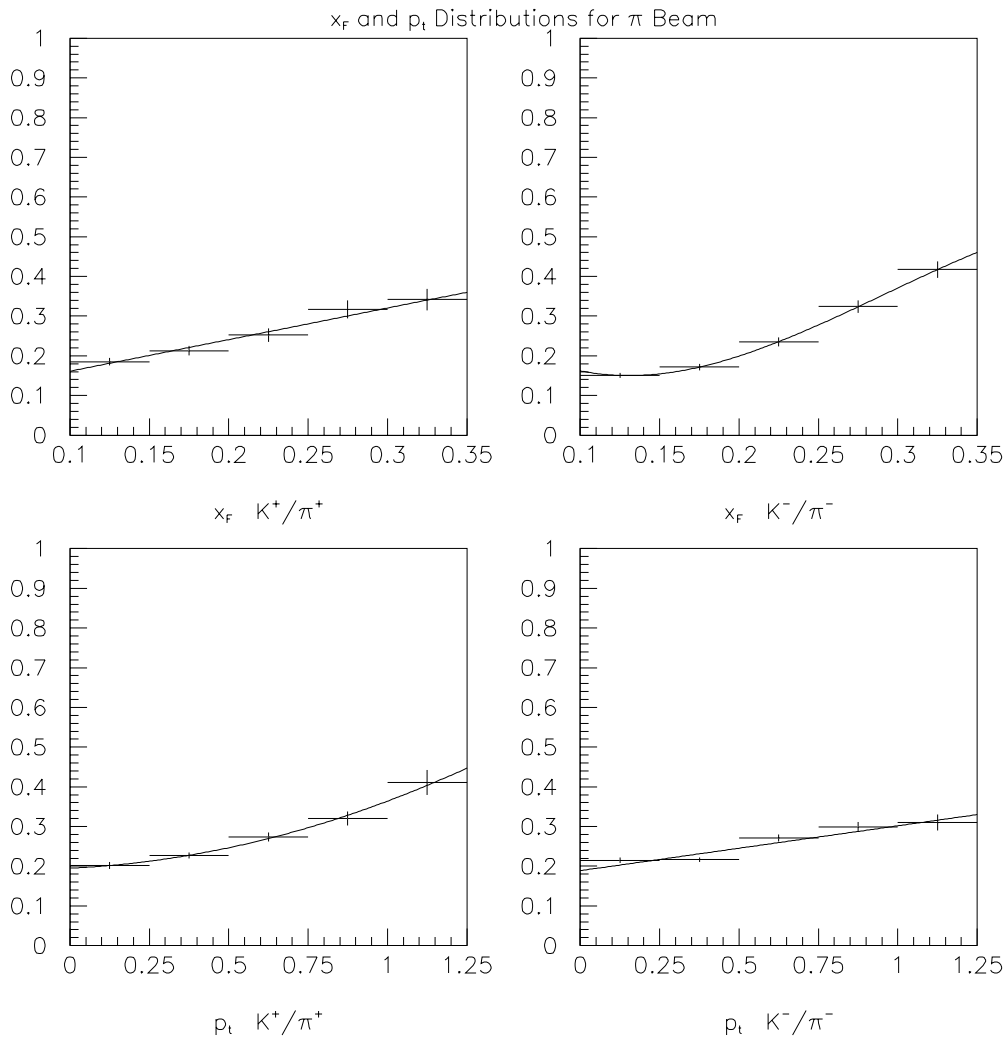

Figure 33: $K^{\pm}/\pi^{\pm}$ Versus x_F and p_t^2 for π^- Beam

The top two histograms in Figure 33 are the x_F distribution of $K^{\pm}/\pi^{\pm}$ and the bottom two are the p_t^2 distribution of the same production ratios for the π^- beam.

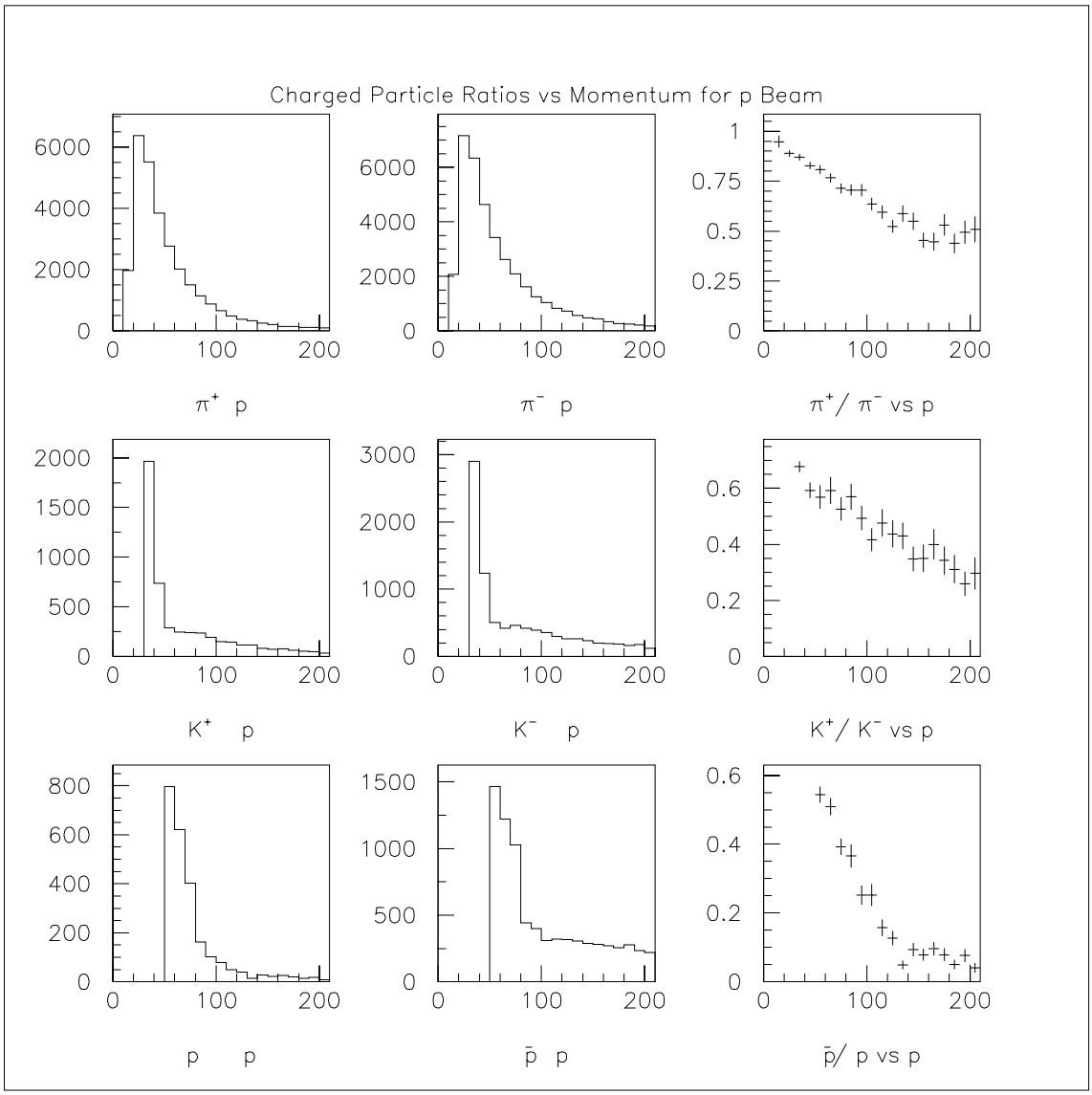

Figure 34: π^+/π^-, K^+/K^- and $\overline{p}/p$ Ratios Versus Momentum for p Beam

Figure 34 shows the momentum distribution of π^+/π^-, K^+/K^- and $\overline{p}/p$ for the proton beam.

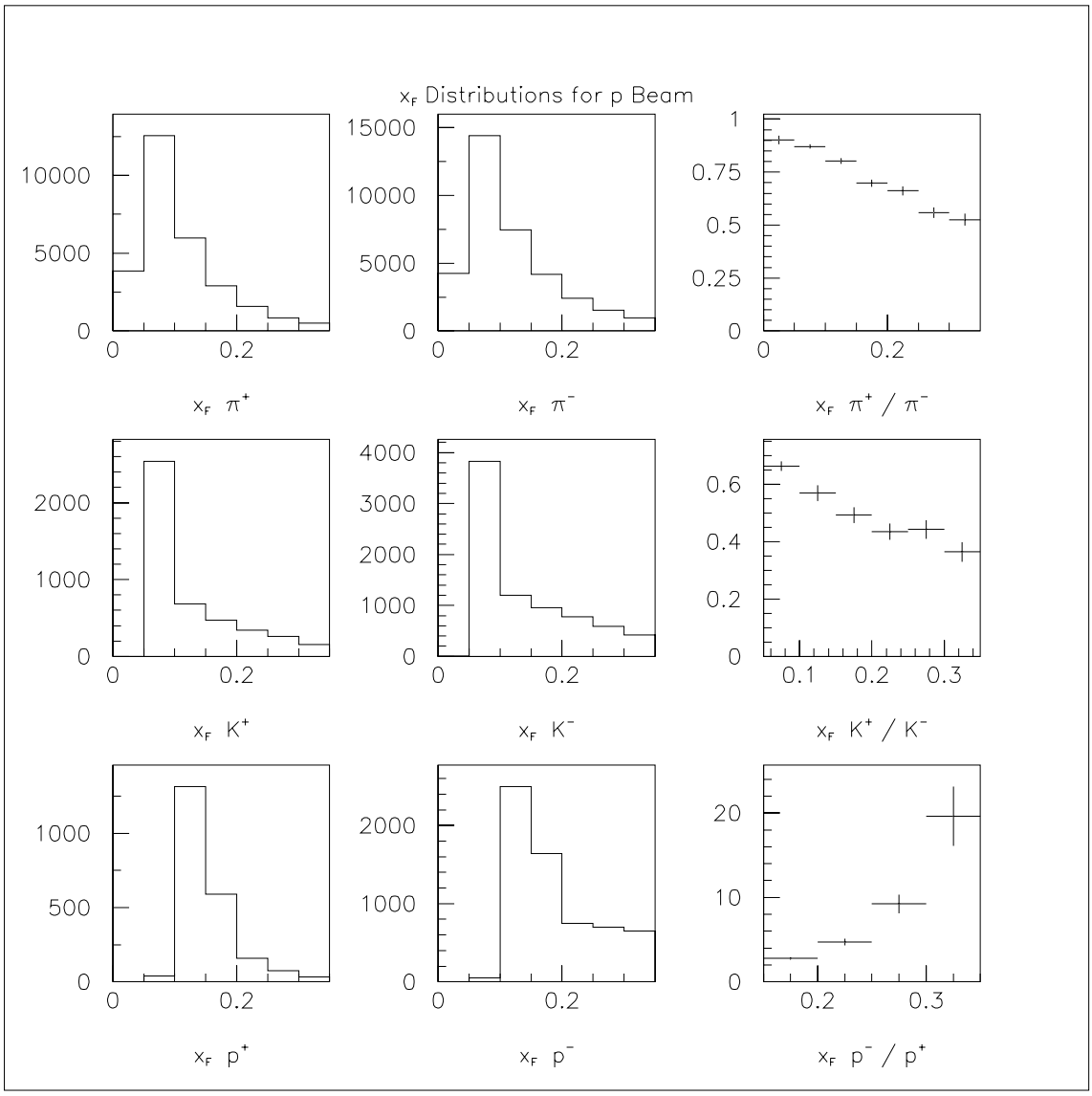

Figure 35: π^+/π^-, K^+/K^- and $\overline{p}/p$ Ratios Versus x_F for p Beam

Figure 35 shows the x_F distribution of π^+/π^-, K^+/K^- and and $\overline{p}/p$ fot the proton beam. The first three entreries at top from left to right are the x_F distributions of π^+ and π^- and the ratio of the two histograms.

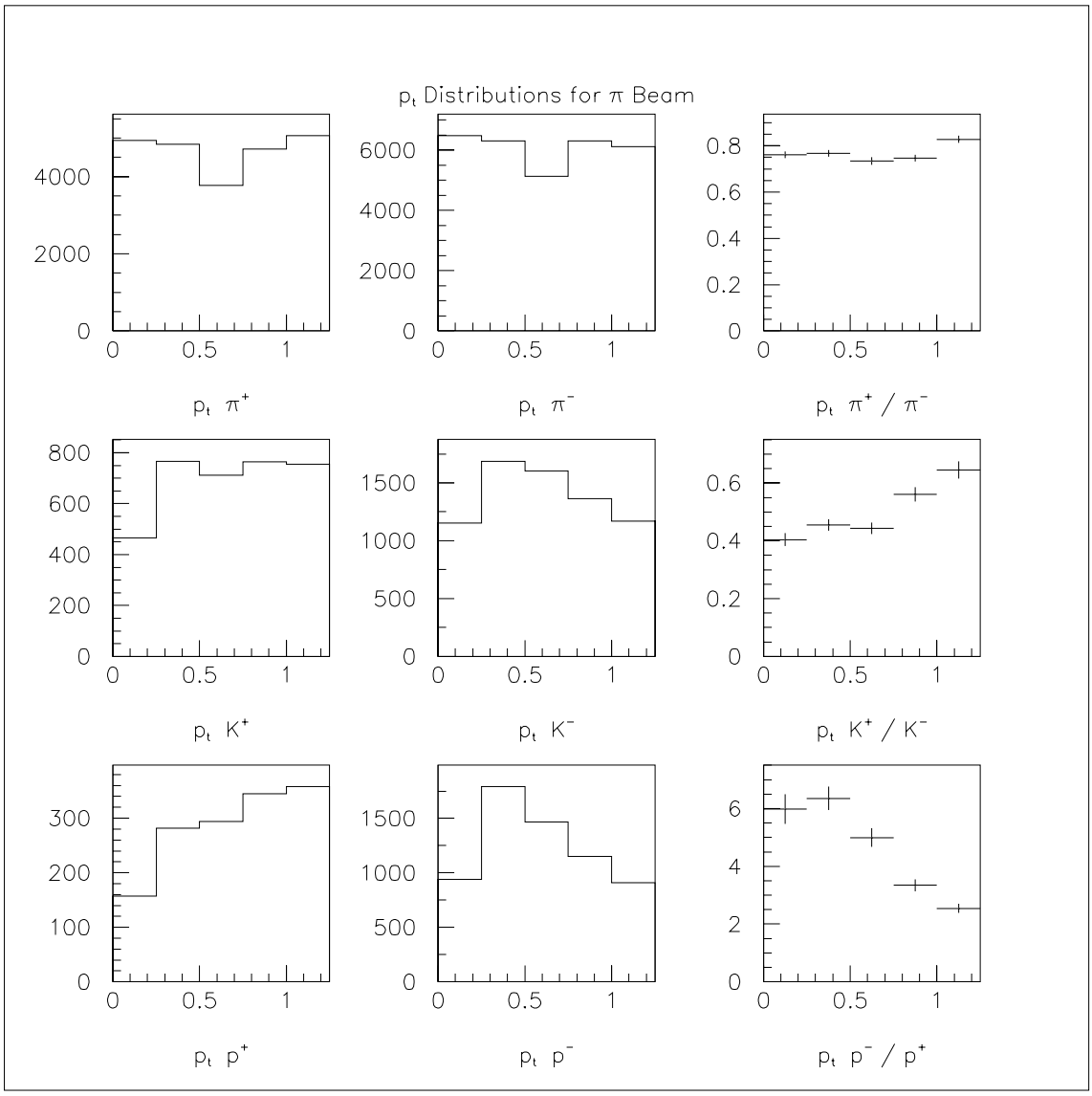

Figure 36: π^+/π^-, K^+/K^- and $\overline{p}/p$ Ratios Versus p_t^2 for p Beam

Figure 36 shows the p_t^2 distribution of π^+/π^-, K^+/K^- and and $\overline{p}/p$ for the proton beam. The first three entries at top from left to right are the p_t^2 distributions of π^+, the p_t^2 distributions of π^- and the ratio of this to histograms.

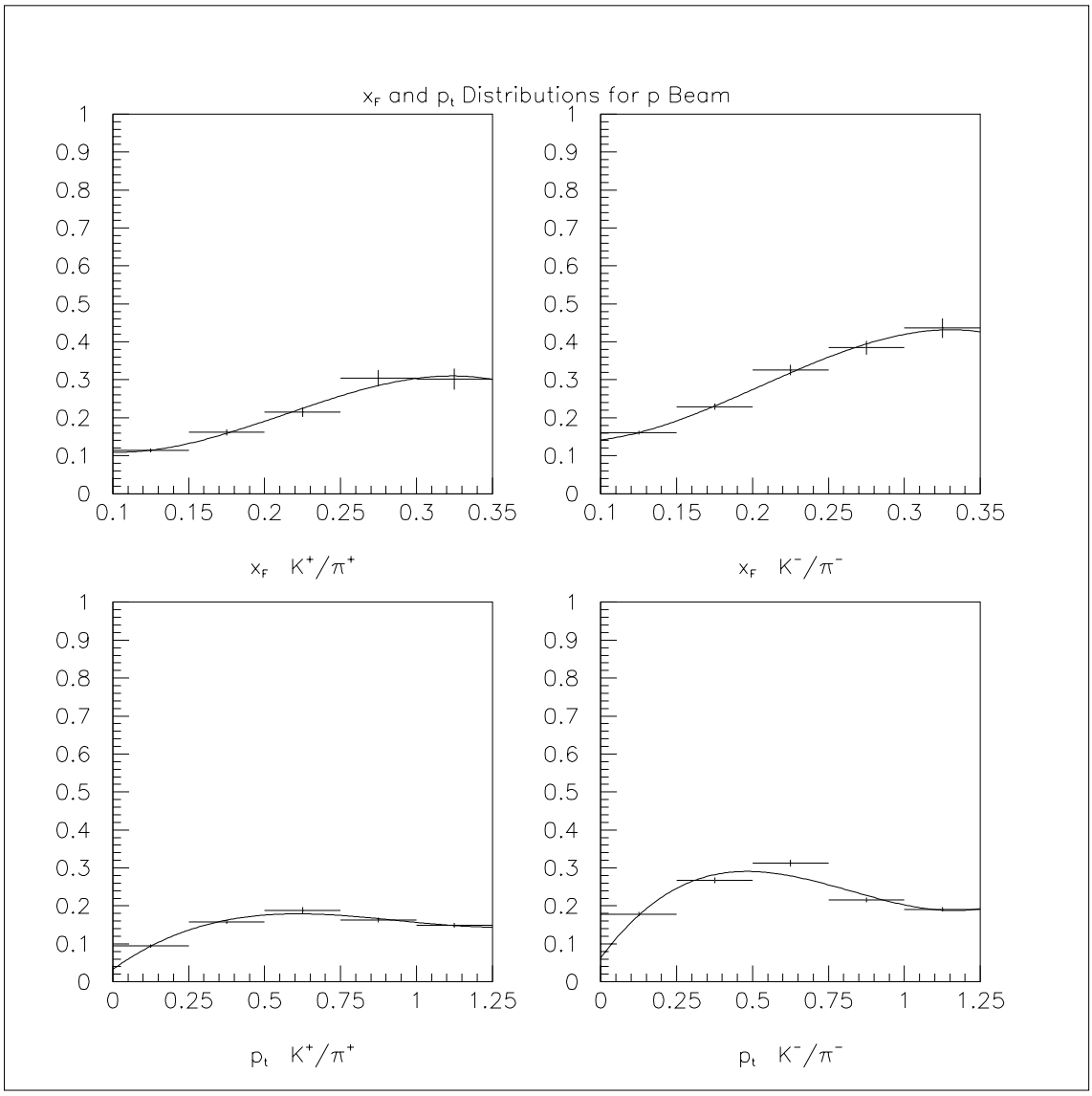

Figure 37: $K^{\pm}/\pi^{\pm}$ Versus x_F and p_t^2 for p Beam

The top two histograms in Figure 37 are the x_F distribution of $K^{\pm}/\pi^{\pm}$ and the bottom two are the p_t^2 distribution of the same production ratios for the proton beam.

CHAPTER V

CONCLUSION

We measured the charged particle production ratios using the SELEX apparatus as a function of the secondary beam particle momentum, x_F and p_t^2. The Feyman-x was defined as fraction of the beam momentum carried off by the secondary particles:

$$x_F = \frac{p}{p_{beam}}$$

and the transverse momentum squared is defined as the summation of the momentum components

$$p_t^2 = p_x^2 + p_y^2.$$

The unique setup of SELEX allow us to measure the charged particle production ratios using the three different kinds of beam particles Σ, π and proton on two types of targets, carbon and copper.

The results were presented in the previous chapter for all three different beam particles separately. In this chapter we will discuss these results.

The first motivation for the charged particle production ratio measurement was to reduce the uncertainty in the the neutrino beam flux calculation. The present uncertainty in the K/π production ratio is one of the dominant sources of the systematic errors in $\nu_e \rightarrow \nu_\mu$ oscillation searches. Below 60 GeV/c this ratio has not been measured and the predictions of the available models of particle production in proton-Be interactions do not agree better that 15% [4]. Previous experiments have measured this ratio in different momentum ranges. Table 10 shows the comparison

of the momentum range of the K/π production ratio of previous experiments to our experiment.

Experiment	p_b (GeV/c)	Target	p (GeV/c)	p_t^2 (MeV/C)
Atherton [5]	400	Be	$60 \leq p \leq 300$	$0 \leq p_t^2 \leq 500$
SPY [4]	450	Be	$7 \leq p \leq 135$	$0 \leq p_t^2 \leq 600$
SELEX	549	C, Cu	$15 \leq p \leq 200$	$0 \leq p_t^2 \leq 1000$

Table 10: Comparison of Experiments

The momentum of the proton beam used in the Atherton [5] and The Secondary Particle Yield (SPY) [3, 4] experiments were comparable, 400GeV/c and 450 GeV/c, respectively, but SELEX had higher beam momentum than both experiments (549 GeV/c). The measurement by Atherton [5] was performed with a proton beam impinging on a series of Be targets with sizes $160 \times 2 \times 40 - 500$mm. The SPY [3, 4] measurements were limited to data collected with a Be target were applied for the differential π/K re-absorption or the decays of the short lived particles within the target, nor the contribution from the secondary interactions. Since SELEX had 5 segmented charm targets that each had less then 1% interaction length which meant that corrections for the target sizes were not necessary. The secondary particle momentum range for SELEX experiment was comparable to the both experiments. The K/π production ratio for the SELEX for proton beam is shown in Figure 37. The overall shape of the momentum spectra for charged particle production ratios agree with the the results by Atherton [5] and SPY experiment [3, 4] in the overlapping region. Our results add the world data sample of the charged particle production ratio measurements. The measurements for the proton beam was with higher beam

momentum but similar secondary beam momentum range.

The second motivation for the charged particle production ratio measurements was to investigate production differences with different beam particles. Since SELEX had the three different beam particles in the same experimental setup, these measurements would not be biased by the apparatus setup or measurement differences. That makes our results a very important addition to the world data sample.

Figure 38 shows the comparison of the π^+/π^- and K^+/K^- production ratios for Σ^- (solid lines) and π^- (dashed lines) beams. Figure 39 shows the comparison of the π^+/π^- and K^+/K^- production ratios for Σ^- (solid lines) and p (dashed lines) beams. Both production ratios show a similar trend in x_F. The summary of the results are tabulated in Table 11, Table 12 and Table 13. Table 11 shows the comparison of charged π^+/π^-, Table 12 shows the comparison of charged K^+/K^- ,and Table 13 shows the comparison of charged $\overline{p}/p$ production ratios for the Σ, π and proton beam particles.

	Incoming	Beam	Particles
x_F	Σ	π	p
0.05	0.646 ± 0.021	0.732 ± 0.034	0.899 ± 0.019
0.10	0.591 ± 0.010	0.698 ± 0.014	0.871 ± 0.009
0.15	0.513 ± 0.011	0.618 ± 0.015	0.834 ± 0.009
0.20	0.391 ± 0.012	0.574 ± 0.017	0.773 ± 0.010
0.25	0.351 ± 0.014	0.490 ± 0.017	0.751 ± 0.012
0.30	0.308 ± 0.015	0.470 ± 0.019	0.691 ± 0.013

Table 11: Comparison of π^+/π^- Ratios for Different Beam Particles

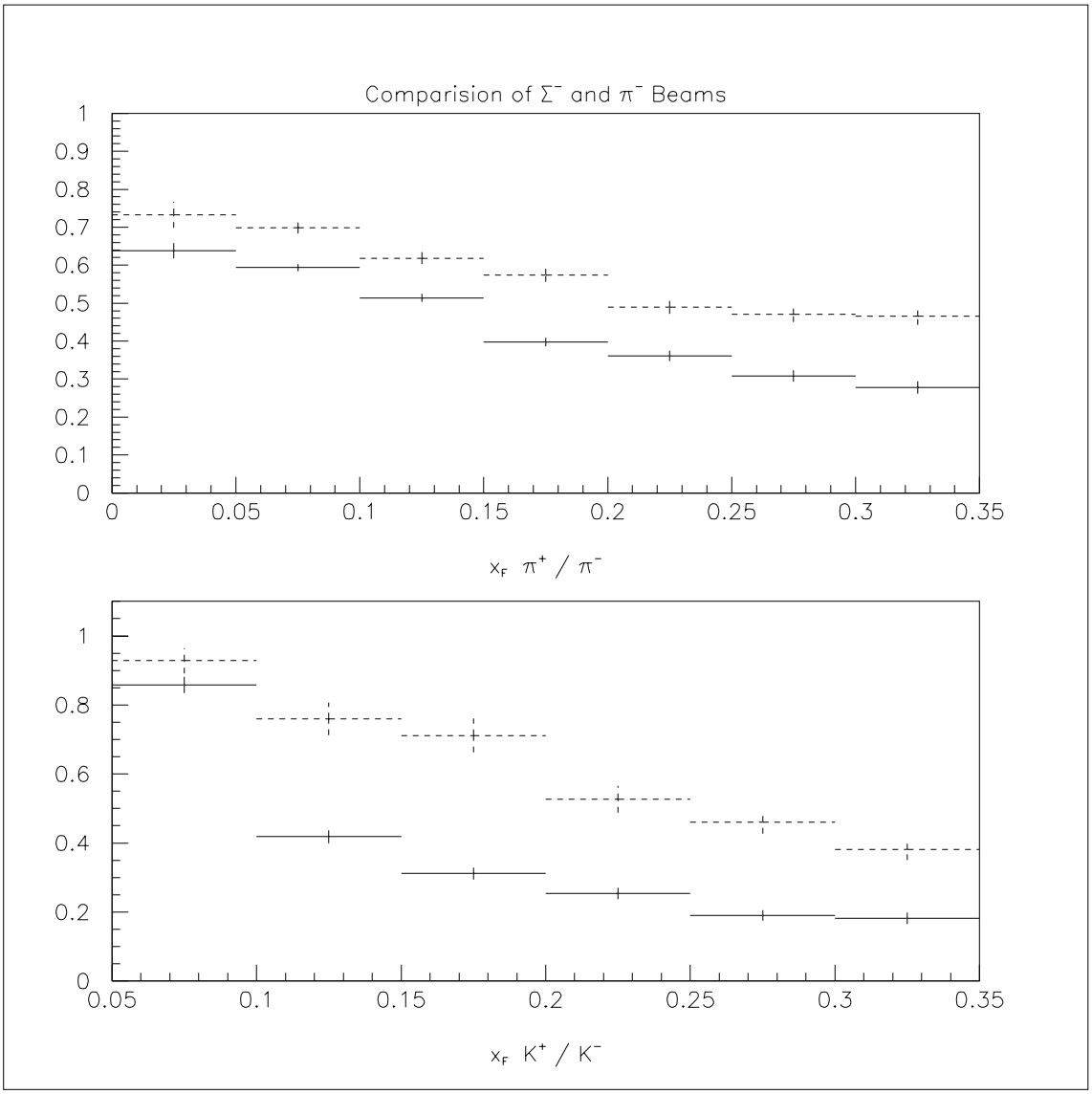

Figure 38: Comparison of Σ^- and π^- Beams

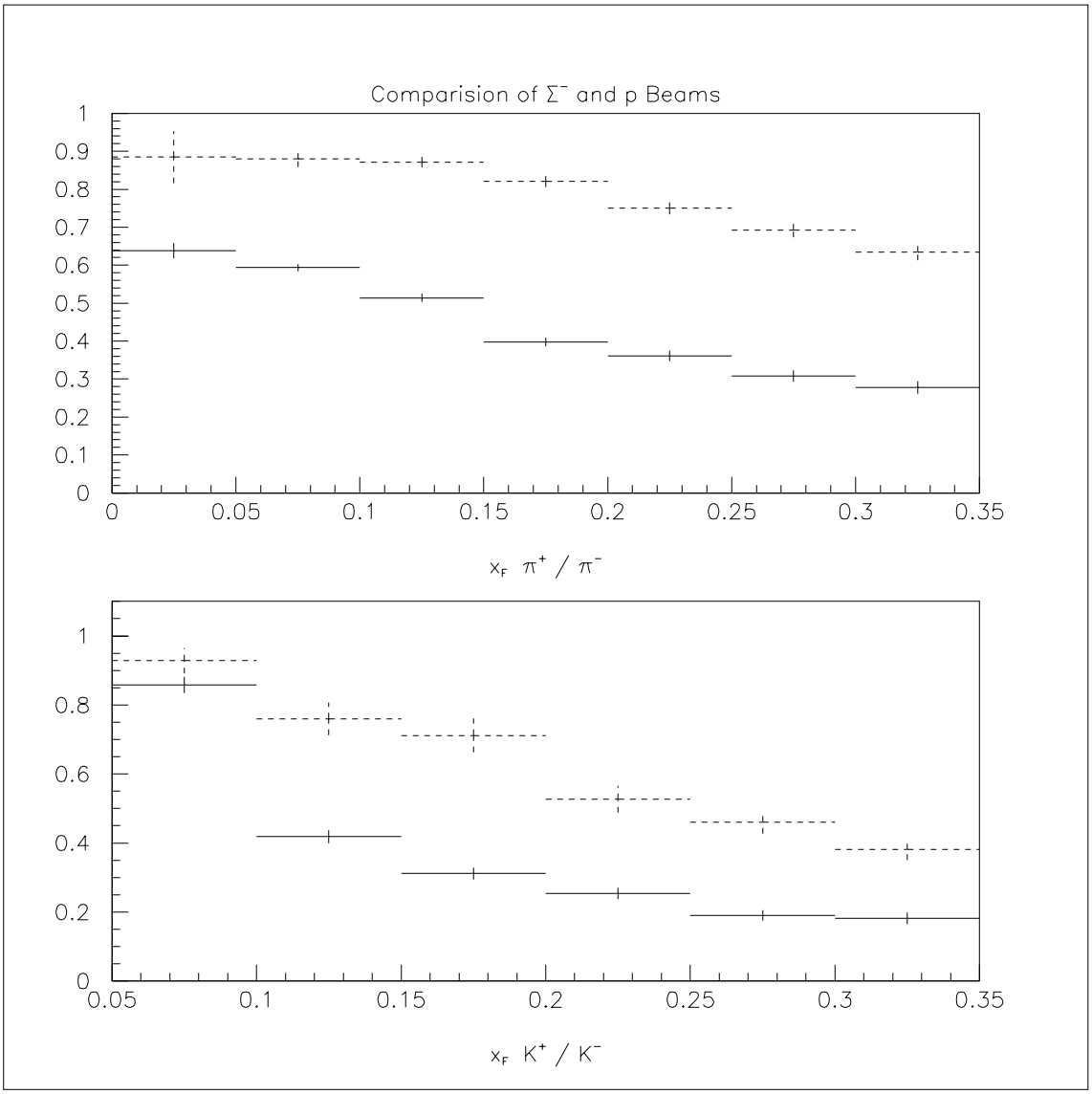

Figure 39: Comparison of Σ^- and p Beams

	Incoming	Beam	Particles
x_F	Σ	π	p
0.05	0.948 ± 0.137	0.918 ± 0.218	0.333 ± 0.384
0.10	0.853 ± 0.025	0.928 ± 0.036	0.758 ± 0.012
0.15	0.430 ± 0.020	0.759 ± 0.047	0.767 ± 0.012
0.20	0.299 ± 0.017	0.711 ± 0.049	0.728 ± 0.014
0.25	0.256 ± 0.018	0.526 ± 0.038	0.662 ± 0.020
0.30	0.182 ± 0.015	0.460 ± 0.034	0.665 ± 0.020

Table 12: Comparison of K^+/K^- Ratios for Different Beam Particles

	Incoming	Beam	Particles
x_F	Σ	π	p
0.05	0 ± 0	0 ± 0	0 ± 0
0.10	1.016 ± 0.058	1.245 ± 0.088	1.325 ± 0.277
0.15	0.939 ± 0.040	1.202 ± 0.063	1.820 ± 0.052
0.20	0.495 ± 0.038	1.318 ± 0.107	1.898 ± 0.047
0.25	0.276 ± 0.026	1.155 ± 0.115	1.840 ± 0.043
0.30	0.192 ± 0.022	1.446 ± 0.164	2.227 ± 0.071

Table 13: Comparison of $\overline{p}/p$ Ratios for Different Beam Particles

Also we investigated the clues for the leading particle effect in the particle production ratios. The production of a particle that has one quark or anti-quark in common with the beam particle is expected to be enhanced at high momentum. The π^+/π^- production ratio in Figure 40 (bottom left) shows a decrease with higher x_F. The Σ^- (sdd) beam enhances the π^- $(\overline{u}d)$ production over π^+ $(u\overline{d})$ because it shares the d quark with the π^-. The same kind of behavior is also true for K^+/K^- production ratio since Σ^- shares a s quark with K^- but none with K^+. Similarly both the π^+/π^- and K^+/K^- production ratios decrease with higher x_F with π^- incoming beam (Figure 41). The dashed lines are for π^-, the solid lines for Σ^- beam. The dashed lines are for π^-, the solid lines for Σ^- beam.

The third motivation was the A-Dependence of the charged particle production ratios. Figure 42 show the the comparison of the π^+/π^- and K^+/K^- production ratios for C (solid lines) and Cu (dashed lines) targets. There is no significant difference, therefore no A dependence in production ratios.

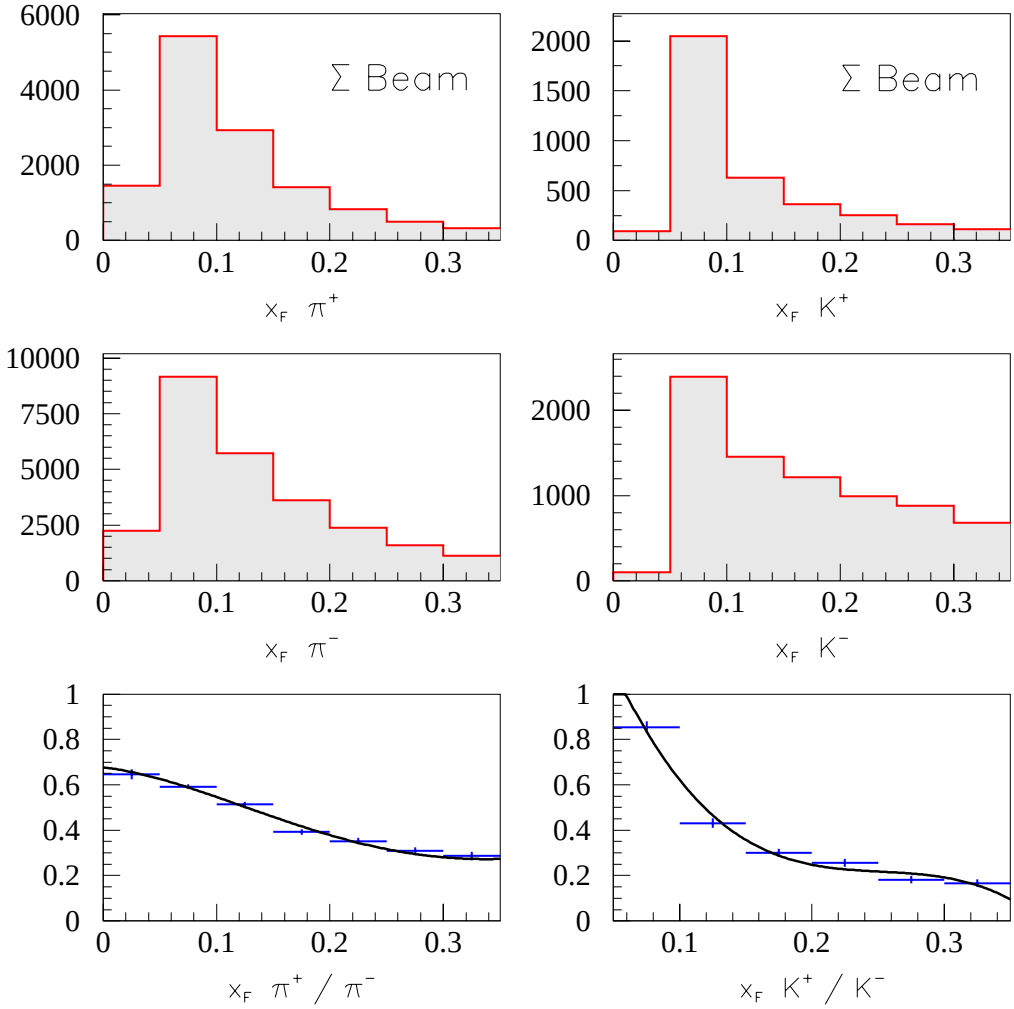

Figure 40: π^+/π^- and K^+/K^- Ratios versus x_F for Σ^- Beam

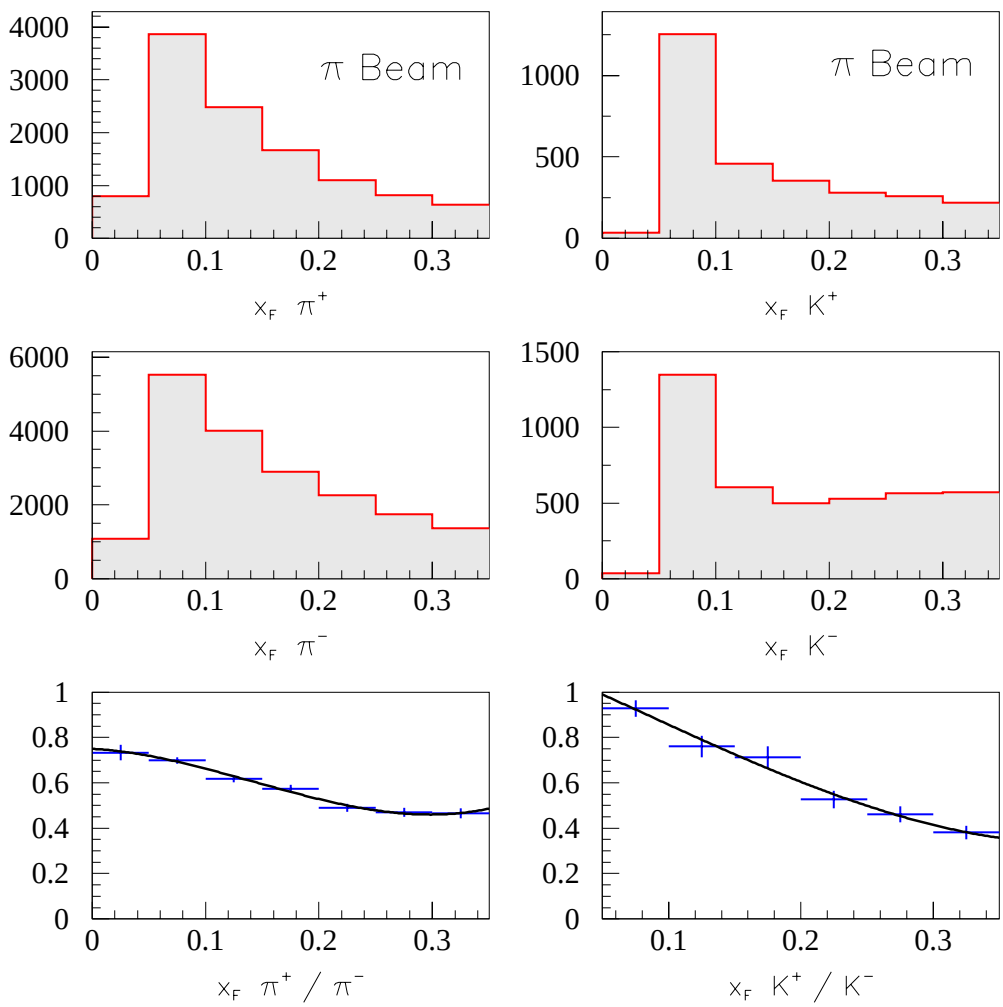

Figure 41: π^+/π^- and K^+/K^- Ratios versus x_F for π^- Beam

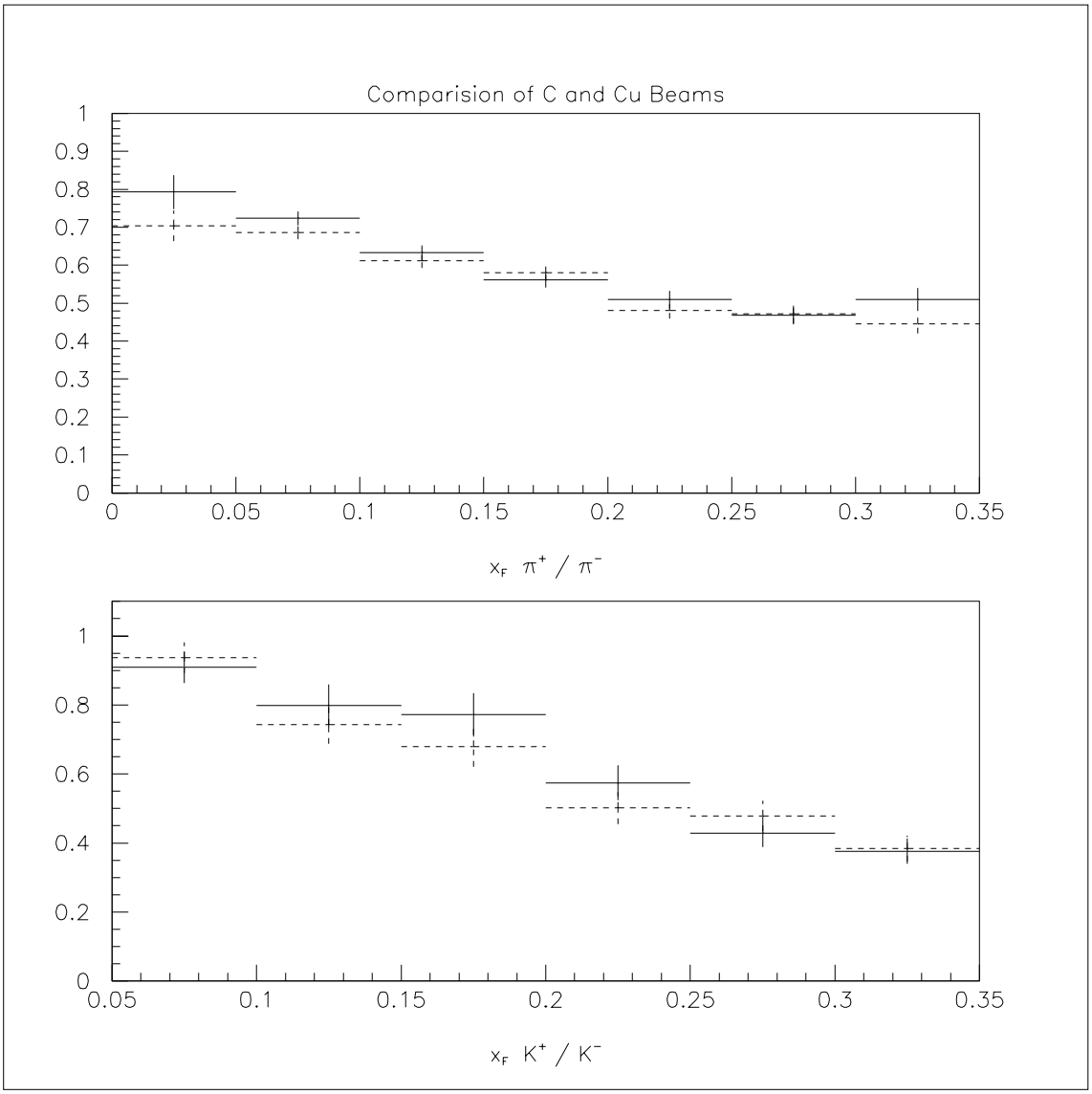

Figure 42: Comparison of C and Cu Targets

APPENDIX A

THE M1 AND M3 MULTI-WIRE PROPORTIONAL CHAMBERS

While the main objective of thsi thesis is to describe the analysis of data and the results, it is also necessary for an experimentalist to contribute to hardware construction and maintanace. I wish to desribe in this appendix my contribution to this effort. There were three large multi-wire proportional chambers installed downstream of the M1 magnet as part of the M1 spectrometer and also three smaller and different type of chambers located downstream of the M3 magnet as part of the M3 spectrometer. These chambers were a contribution of the Iowa-Trieste Group to the SELEX experiment. We will give a detail explanation of these chamber systems in this apendix starting from M1 multi-wire proprtional chambers, continuing with M3 multi-wire proprtional chamber, and the readout system and finally efficiencies these chambers.

1.1 The M1 Multi-Wire Proportional Chambers (M1WPC)

The outside dimension of each chamber was $2390 \times 2390 mm^2$ and the inside dimension was $2000 \times\ 2000\ mm^2$. Each chamber consisted of 11 stesalit frames and the frames were 6 ± 0.054 mm thick as shown in Figure 43. The cathode planes were built by stretching plastic foils over these Stesalit frames. The foils were coated on both sides with graphite. The graphite coating of the planes was applied by twice spraying the planes with Acheson 502 paint concentrated with 50 % methy-butyl ketone. The tension of the foil was set to about 50 kg/m. The conductive external

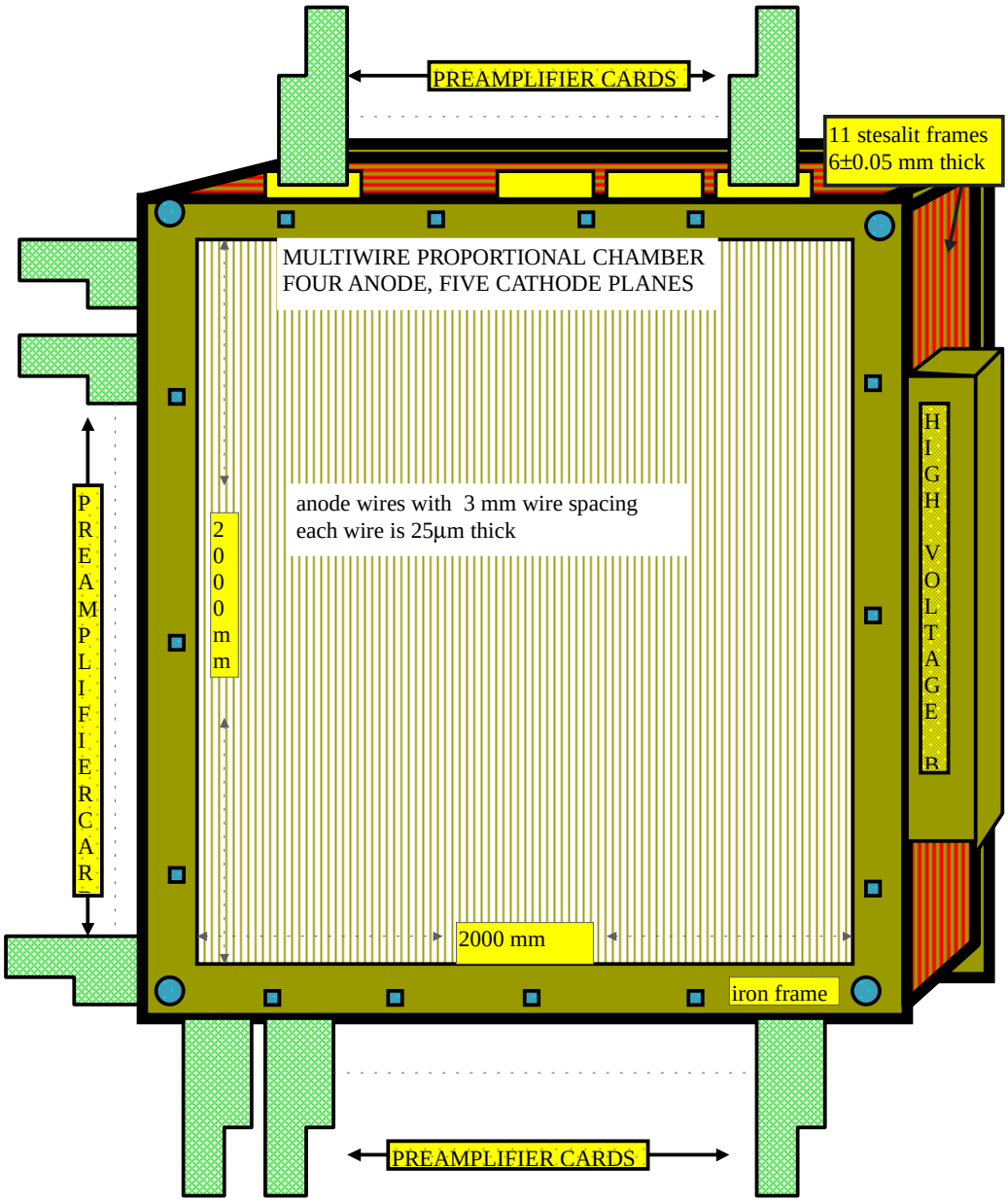

Figure 43: The Schematics View the MWPC

sides of the first and the last cathode foils remove electrostatic charges accumulated on the surface. Each chamber was equipped with a beam killer region in the center of the cathode plane. The beam killer region allows the high intensity beam to pass through the chamber without damaging it. However, for SELEX this region in the MWPCs was painted over with the conducting paint mentioned above since the beam intensity is not expected to be that high. The wires were 25 mm thick and are soldered on printed boards with a precision of 0.1 mm and a tension of 70±5 g. There were three guard wires with diameters of 50, 75, and 100 mm, located at the edges. There were four different anode plane orientations (X, Y, V and U) in each MWPC as shown in Figure 44 vertical, horizontal and oblique planes at an angle of $\pm 28.070^o$ with respect to the vertical direction. These angles were chosen because their sine and cosine values are rational numbers (8/17 and 15/17). The separation between two anode wire planes was 12 ± 0.05 mm. Each chamber has two zig-zag shaped Mylar strips (garlands), 5 mm wide, located between the cathode foils and the anode wires (Figure 45). They reduce the free wire length to a third of the total that was measured to be about 0.7 m for this kind of chamber. In case of an unbalanced electrostatic force the garlands suppressed the bending of the cathode foils. The garlands were 0.3mm thick and they were attached to a supporting nylon wire at three points. The nylon wires were connected at both ends to the stesalit frames with a tension of 1 kg. There were also insulated field wires, 0.9 mm diameter, stretched along the garlands in the 1 mm space between the garlands and the anode wires. These field wires were used to restore the local chamber efficiency reduced by the garlands. In SELEX, these wires were set to 1500 V. Iron frames were used to hold the 11 staselit frames and the cathode-anode planes together. The reason for choosing the iron frame was that the thermal expansion coefficients of iron and Stesalit are nearly the same. The

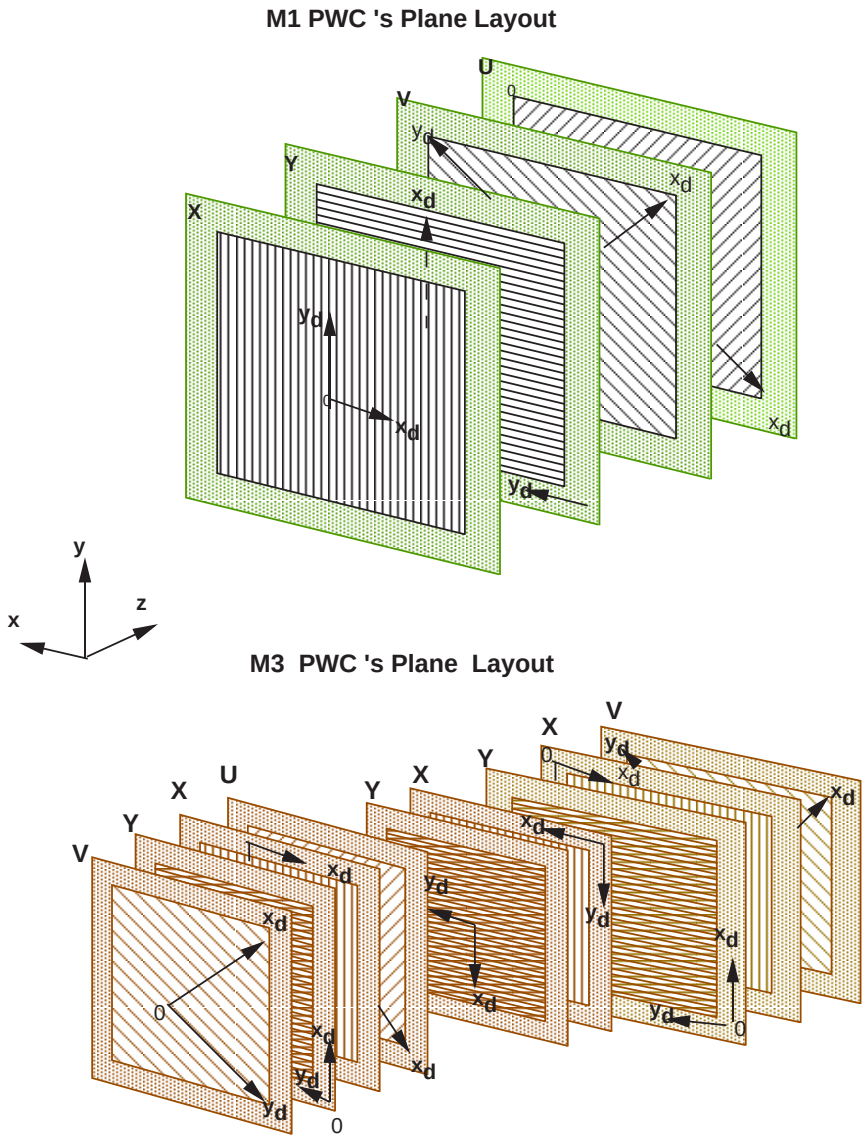

Figure 44: The Plane Orientation of M1PWC and M3PWCs Planes.

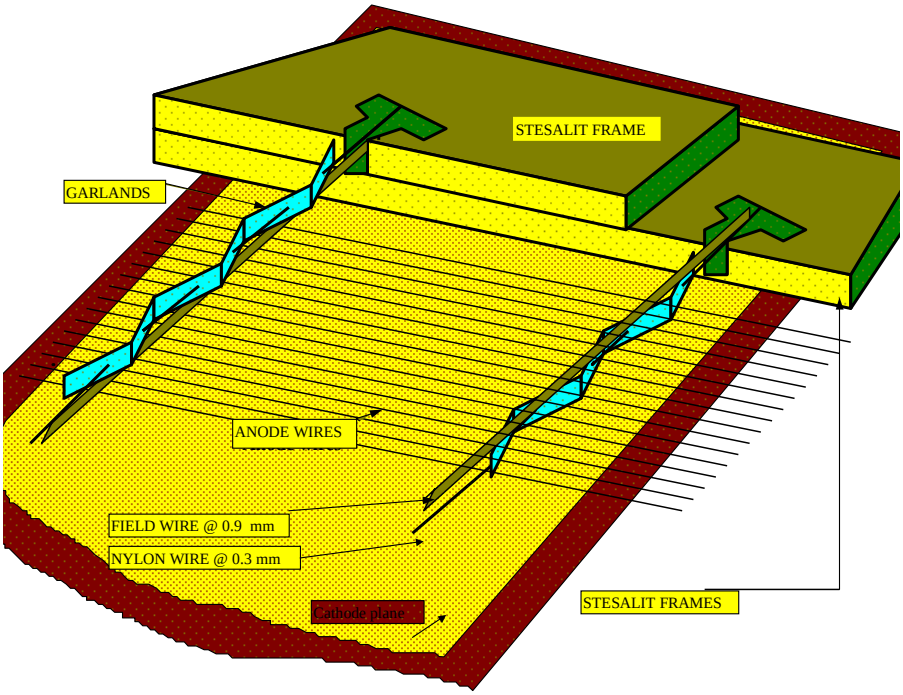

Figure 45: The Mylar Ctrips(garlands) in Multiwire Proportional Chamber.

MWPCs were assembled with pins and screws through the frames. The gas tightness was secured by O-rings placed in grooves in the chamber frames. There were four gas inlets and outlets distributed along two opposite sides of the frame to provide a uniform gas flow.

1.2 The M3 Multi-Wire Proportional Chambers (M3WPC)

There were three types of multi-wire proportional chambers located in the downstream after the M3 magnet in SELEX. These so-called "Lambda Chambers" were smaller than the M1PWCs mentioned above. The first chamber consisted of four planes (V, Y, X and U). The second one had only two planes (Y and X) and the third one had three planes (Y, X, and V). One significant difference between these chambers and the large chambers was that they had wire cathode planes with transparent windows as opposed to having a graphite surface plane with opaque covers.

The first Lambda chamber (M3PWC1): The size of the first Lambda chamber was 64x64 cm^2 (internally) and each plane had 320 wires with a 2 mm wire spacing. There were two wire cathode planes for each anode plane and there was a gap, 8mm, between the two cathode planes. The slanted planes were installed at an angle of $\pm$ 28.070 with respect to the vertical similar to the M1PWCs. The distance between V-Y and X-U was 52 $\pm$ 0.05 mm, while between Y-X planes it was 14 $\pm$ 0.05 mm.

The second Lambda chamber (M3PWC2): The second chamber was the same as the first one except it has two planes: X and Y, with a 24 $\pm$ 0.05 mm separation. The wire spacing is the same as for the first Lambda chamber.

The third Lambda chamber (M3PWC3): The third Lambda chamber was quite different in comparison to the first and second Lambda chambers. The internal dimensions of this chamber were 115x89 cm^2. It had three planes: Y, X and V with

a 2mm wire spacing. The first plane consisted of 448 wires, the second one had 576 wires and third one had 672 wires. The plane separation is 12 ± 0.05 mm.

1.3 The Electronics for the M1PWCs and M3PWCs

The electronics setup for the chambers can be discussed in three parts: preamplifier cards, the readout system, and the readout control logic.

The signals from each wire are usually too weak to be transferred to the readout system directly. Preamplifiers were used to amplify the weak signals from the detector and to drive them through the twisted cables that connect the preamplifiers with the readout system. Because of the low signal levels the noise might be significant and also additional noise may be picked up. In order to reduce or keep the noise level to a minimum the preamplifiers needed to be mounted as close to the detector as possible. Each preamplifier card contained 32 individual amplifiers with a differential gain of 7 ± 1 for each channel. Preamplifier cards were supplied with -5.2 V.

The RMH2 (Receiver-Memory Hybrid) readout system, developed at CERN, was used for the purpose of processing the PWC signals, encoding the resulting hit pattern, and transferring the encoded data to the main data acquisition system. Each RMH crate contained 22 RMH modules, 1 Crate Controller (CC), 1 Crate Encoder (CE). The overall RMH system is read out with 1 system Encoder (SE), Branch Receiver (BR), and Interface (IF).

The RMH modules discriminated the received detector signals and strobed them into memory. The signals from the individual wires amplified by the preamplifier cards installed on the chambers came to the RMH modules via a special 32 pair twisted cable. The length of this cable was chosen so as to delay the chamber signals to allow enough time for the trigger to be formed. In SELEX the cable length was 80 m which

delayed the chamber signals by 400 ns. Each RMH module had inputs and outputs on the front panel and on the back. The front panel inputs consisted of 32 wire signal inputs, a flag switch to indicate the beginning of a different detector in a specific unit, one fast strobe (NIM lemo connector) and a threshold control which could be adjusted through a front panel trimpot in the Crate Controller (CC) unit. The threshold level measured at the monitor posts could be from -1.4 V to -5.2 V corresponding to -5mV to -25 mV in the signal. The threshold had to be set to such a voltage that all valid signals would be accepted and noise rejected. The outputs included a monitor giving real time signals for each channel that had a nonzero input. The Rear connector inputs consisted of a fast strobe (crate), a read, a reset, and a threshold control. The RMH modules were located in a special RMH crate that contained at most 22 RMH modules, and each crate had a crate encoder (CE). Up to 16 CEs could be connected to the branch highway. All the CEs communicated with a system encoder (SE) which was mounted in a regular CAMAC crate. In SELEX, there were total of 20 crates for M1 and M3 chamber readout.

The Crate Controller contained the threshold adjustment, an overall monitor output and a fast reset input to reset all RMH modules in the crate. All modules could be strobed in parallel via the Crate Controller (CC) strobe input.

The main purpose of the Crate Encoder was to receive the data pattern from the RMH modules and to encode this data pattern into a 16-bit data word, including the relevant information about the station number of the specific RMH module and the crate address. The crate address was set with a screw driver by selecting the appropriate number in the switch in the front panel of the CE. The data from the RMH modules were logically divided into lower and upper halves (channels 0 - 15 and channels 16 - 31). Only modules and halves containing data were addressed.

The System Encoder (SE) was housed in a CAMAC crate. It was used to control the data pattern from the crate encoder modules. It started the readout via the start read signal that came from an external device such as the CAMAC interface. The system encoder received branch data in strobed mode and formed for each piece of data a 16 -bit binary coded word. The output data flow was controlled via double handshake mode and end of read (EOR) signal indicates the completion of an event.

The Branch Receiver (BR) was used to extend the addressing capability of the RMH system. More than one (up to 18) Branch Receiver could be connected.

The regular CAMAC interface was designed to communicate with the System Encoder via the internal output bus and to perform block transfer operations via repeat, pause, or stop mode. There is an interface that was specially designed to communicate with a DYC unit in the SELEX DAQ system, called a DYC interface. It is located inside the same CAMAC crate as that for SE and BR units.

This module buffered the data from the RMH and reformatted the 16 bit-word data into 32 bit-word data. It accepted data and control signals from the RMH modules, latched four front panel input bits (event id), attached a leading word count to the RMH data (4096 long word) and transmited a header longword (word count and front panel bits) that is 512 deep.

There were two trigger level signals that were used for the data processing, T1 and T2. T1 produced a strobe signal that was sent to all the Crate Controllers to start latching the data into the memory (Figure 46).

The trigger logic system also sent a signal (T2) which was redefined as REQ. This was sent to the DYC 3b for starting up the data processing. The T2 signal did not come for every event because the existence of a T2 signal by definition indicates a valid event type. Upon receiving the REQ signal, the DYC 3b sended a read-enable

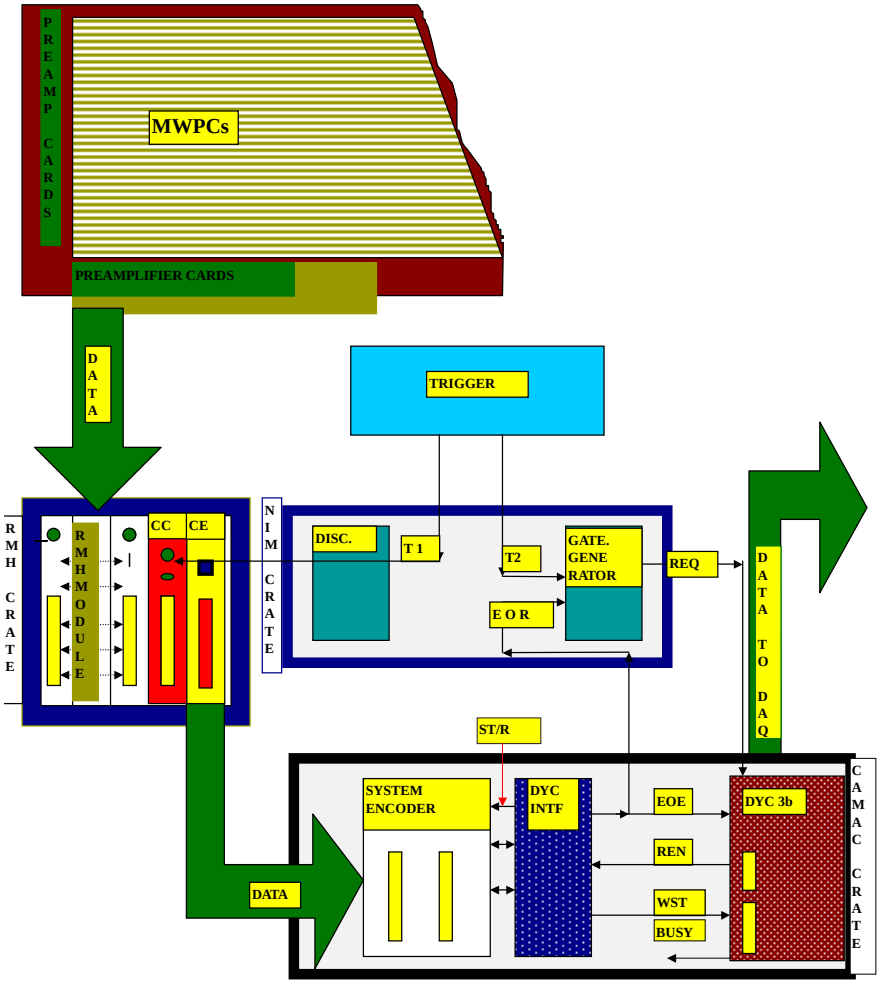

Figure 46: The Block Diagram of the PWC Readout System

(REN) signal to the DYC Interface. Then DYC Interface set the busy on so that there would be no additional T1 and T2 signals coming. This BUSY signal was sent to the trigger logic system to be included in the general trigger. When the System Encoder(SE) received the start-read (ST/R) signal through the DYC interface, it started transferring the data encoded by individual Crate Encoders in each crate. SE and DYC Interface were connected internally. In addition to turning on the BUSY signal, the SE also sended a Write Strobe (WST) signal to the DYC 3b after receiving the REN signal. Then DYC 3b readed one data word. This process continued until all data words in the RMH system were transferred to the DYC 3b buffer memory. When the data transfer was completed DYC interface sended an end-of-read (EOR) signal to turn off the REQ signal latched by a gate-and-delay generator. At the same time it also sended an end-of-event(EOE) signal to the DYC 3b. When the DYC 3b received the EOE signal, it turned off the REN signal to the DYC interface which caused the BUSY signal to go off. This signaled the completion of the readout cycle of the RMH system to the main trigger.

1.4 Efficiency of the M1PWC and M3PWC

There were several aspects that affect the efficiency of the chambers, such as the gas mixture, high voltage, the threshold setting, and the gate width on the readout electronics that selected the correct signals.

In SELEX experiment M1 multiwire proportional chambers were operated at a HV value of 3.0 kV with a 24.0 % Isobutane and 0.15 % Freon concentration. On the other hand, the M3 multi-wire proportional (Lambda) chambers were operated at 4.3 kV (2 mm wire spacing) with a 22 % Isobutane and 0.3 % Freon concentration.

The threshold setting was very important in optimizing the operation of the

chambers. In M1 multi-wire proportional chambers, the thresholds were set to - 1.4 V. On M3PWCs the threshold setting is -1.6 V.

The main idea for the RMH system was to put all the hit information into the memory simultaneously since all the signals come in at the same time and to read out the information stored in the memory sequentially. The signals from the hit wires amplified by the preamplifiers were transferred to the RMH modules by twisted pair cables. The data input of the RMH modules were activated by a strobe signal. In SELEX, the strobe gate was adjusted to be 210 ns wide for M1PWCs and 400 ns for M3PWCs. This was a time window sufficient for collecting the data from the chambers. This gate had to be wide enough to accept all the signals from the chambers and short enough to reject the signals considered to be noise.

The efficiency studies were done by two different methods: using a radiactive source and using the beam trigger runs. Using a radiavtive source, such as A Sr90 source, the chamber efficiency was calculated by locating the chamber between two beam-defining scintillation counters and using the coincidence between the counters as a trigger. The number of signals in coincidence with this trigger divided by the number of triggers yields the efficiency. Figure 47 show the efficiency plateau cureves versus high voltage for M1 PWC for differnt gas mixtures.

The π^- from the hyperon beam were used to calculate M1 and M3 PWC efficencies as the second method. In this method, all the π the tracks segments were either interpolated or extrapolated to a specific chamber plane position and hits in the M1 orM3 PWC were collected in the trajectory of that track segment. The efficiency was then calculated taking the the ratio of the number of tracks that were accompanied with a nearby hit to the total number of tracks used.

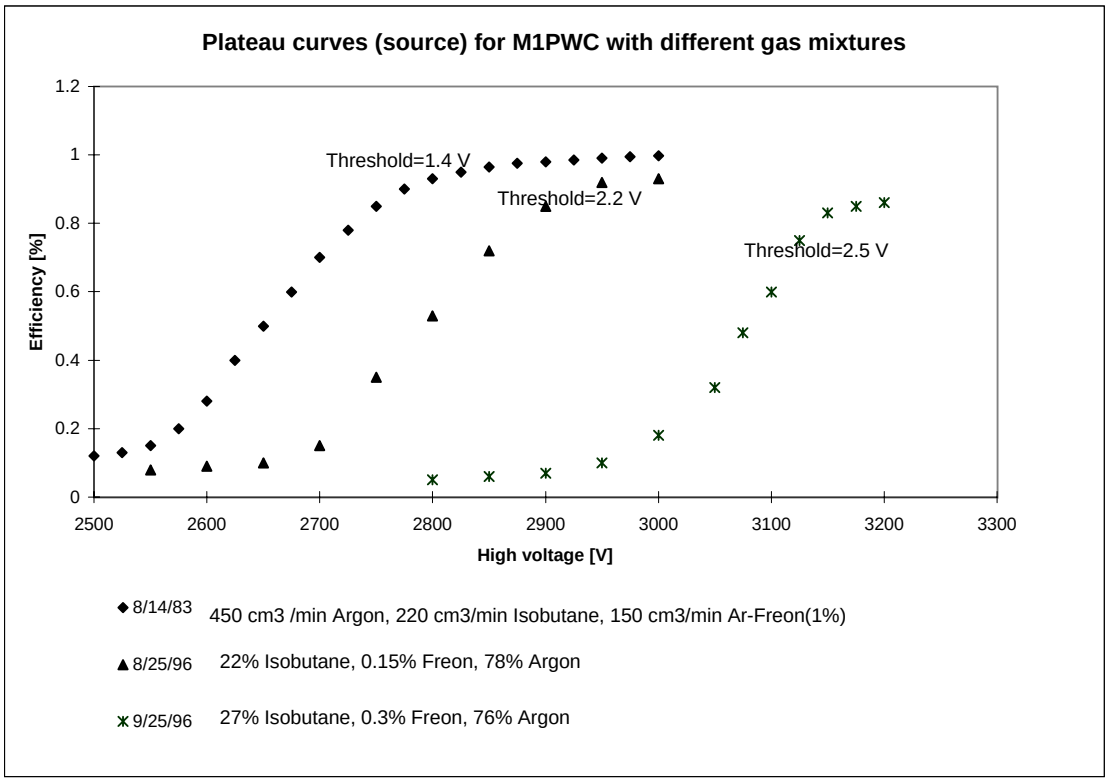

Figure 47: Plateau Curves Obtained With a Sr^{90} Source for M1PWC

The SELEX Collaboration

G.P. Thomas
Ball State University, Muncie, IN 47306, U.S.A.

E. Gülmez
Bogazici University, Bebek 80815 Istanbul, Turkey

R. Edelstein, S.Y. Jun, A.I. Kulyavtsev[1], A. Kushnirenko, D. Mao[1], P. Mathew[2], M. Mattson, M. Procario[3], J. Russ, J. You[4]
Carnegie-Mellon University, Pittsburgh, PA 15213, U.S.A.

A.M.F. Endler
Centro Brasileiro de Pesquisas Físicas, Rio de Janeiro, Brazil

P.S. Cooper, J. Kilmer, S. Kwan, J. Lach, E. Ramberg, D. Skow, L. Stutte
Fermilab, Batavia, IL 60510, U.S.A.

V.P. Kubarovsky, V.F. Kurshetsov, A.P. Kozhevnikov, L.G. Landsberg, V.V. Molchanov, S.B. Nurushev, S.V. Petrenko, A.N. Vasiliev, D.V. Vavilov, V.A. Victorov
Institute for High Energy Physics, Protvino, Russia

Li Yunshan, Mao Chensheng, Zhao Wenheng, He Kangling, Zheng Shuchen, Mao Zhenlin
Institute of High Energy Physics, Beijing, P.R. China

M.Y. Balatz[5], G.V. Davidenko, A.G. Dolgolenko, G.B. Dzyubenko, A.V. Evdokimov, M.A. Kubantsev, I. Larin, V. Matveev, A.P. Nilov, V.A. Prutskoi, A.I. Sitnikov, V.S. Verebryusov, V.E. Vishnyakov
Institute of Theoretical and Experimental Physics, Moscow, Russia

U. Dersch[6], I. Eschrich[7], I. Konorov[8], H. Krüger[9], J. Simon[10], K. Vorwalter[11]
Max-Planck-Institut für Kernphysik, 69117 Heidelberg, Germany

I.S. Filimonov[5], E.M. Leikin, A.V. Nemitkin, V.I. Rud
Moscow State University, Moscow, Russia

A.G. Atamantchouk[5], G. Alkhazov, N.F. Bondar, V.L. Golovtsov, V.T. Kim, L.M. Kochenda, A.G. Krivshich, N.P. Kuropatkin, V.P. Maleev, P.V. Neoustroev, B.V. Razmyslovich, V. Stepanov, M. Svoiski, N.K. Terentyev[12], L.N. Uvarov, A.A. Vorobyov
Petersburg Nuclear Physics Institute, St. Petersburg, Russia

I. Giller, M.A. Moinester, A. Ocherashvili, V. Steiner
Tel Aviv University, 69978 Ramat Aviv, Israel

J. Engelfried[4], A. Morelos
Universidad Autónoma de San Luis Potosí, San Luis Potosí, Mexico

M. Luksys
Universidade Federal da Paraíba, Paraíba, Brazil

V.J. Smith
University of Bristol, Bristol BS8 1TL, United Kingdom

M. Kaya, E. McCliment, K.D. Nelson[13], C. Newsom, Y. Onel, E. Ozel, S. Ozkorucuklu, P. Pogodin
University of Iowa, Iowa City, IA 52242, U.S.A.

L.J. Dauwe
University of Michigan-Flint, Flint, MI 48502, U.S.A.

M. Gaspero, M. Iori
University of Rome "La Sapienza" and INFN, Rome, Italy

L. Emediato, C.O. Escobar[14], F.G. Garcia[4], P. Gouffon, T. Lungov[15], M. Srivastava, R. Zukanovich-Funchal
University of São Paulo, São Paulo, Brazil

A. Lamberto, A. Penzo, G.F. Rappazzo, P. Schiavon
University of Trieste and INFN, Trieste, Italy

REFERENCES

[1] P. Mathew and J. Russ, *SELEX Internal Report*, **H-Note 795** (1994).

[2] D. E. Groom *et al.*, *Eur. Phys. J.***C15**(2000) 1.

[3] G. Ambrosini *et al.* [NA56/SPY Collaboration], Eur. Phys. J. C **10**, 605 (1999).

[4] G. Ambrosini *et al.* [SPY Collaboration], Phys. Lett. B **420**, 225 (1998).

[5] H. W. Atherton *et al.*, CERN-80-07.

[6] B. Andersson, G. Gustafson and C. Peterson, Phys. Lett. B **69**, 221 (1977) [Erratum-ibid. **72B**, 503 (1977)].

[7] K. P. Das and R. C. Hwa, Phys. Lett. B **68**, 459 (1977) [Erratum-ibid. **73B**, 504 (1977)].

[8] L. G. Pondrom, Phys. Rept. **122**, 57 (1985).

[9] F. Dittus *et al.* [NA52 (NEWMASS) Collaboration], Nucl. Phys. A **590**, 347C (1995).

[10] J. Russ *et al.*, Proposal P781, Fermi Lab, 1987.

[11] F. L. Fabri *et al.*, [FOCUS Collaboration], hep-ex/0011044.

[12] J.Russ *et al.*, International Conferance on High Energ Phyiscs (ICHEP 2000), Osaka, Japan, 27 Jul.- 2 Aug. 2000.

[13] F. Garcia, Ph.D. Thesis, University of Sao Paulo, Sao Paulo, Brazil, 2000.

[14] A. Kushnirenko *et al.*, [SELEX Collaboration], Phys. Rev. Lett. **86**, 5243 (2001).

[15] G. Bellini, I. BIlgi, and P. J. Dornan, *Phys. Rept.* **289**(1997) 1.

[16] S. Y. Jun *et al.*, [SELEX Collaboration], Phys. Rev. Lett. **84**, 1857 (2000).

[17] U. Dersch *et al.*, [SELEX Collaboration], Nucl. Phys. B **579**, 277 (2000).

[18] I. Eschrich *et al.* [SELEX Collaboration], hep-ex/0106053.

[19] K. Vorwalter, Ph.D. Thesis, Max-Planck Institut fur Kernphysik, 1998.

[20] I. Eschrich *et al.*, [SELEX Collaboration], hep-ex/9812019.

[21] H. Krueger, Ph.D. Thesis, Max-Planck Institut fur Kernphysik, 1999.

[22] P. Pogodin, Ph.D. Thesis, University of Iowa, 1999.

[23] K. D. Nelson , Ph.D. Thesis, University of Iowa, 1999.

[24] J. Lach, *et al.*, *SELEX Internal Report*, **H-Note 808** (1999).

[25] J. Lach *et al.*, *SELEX Internal Report*, **H-Note 819** (1999).

[26] V. Maleev, N. Bondar, A. Krivshich, S. Patrichev and N.T erentyev, *SELEX Internal Report*, **H-Note 747** (1995).

[27] K. Nelson, C. Newsom *SELEX Internal Report*, **H-Note 771** (1995).

[28] A. Atamantchuk *et al.*, *Nucl. Instr. and Meth.* **A425**(1999)529.

[29] N.Terentyev, *SELEX Internal Report*, **H-Note 745** (1995).

[30] A.Kushnirenko, M.Mattson, J.Russ *SELEX Internal Report*, **H-Note 756** (1995); P.Mathew and J.Russ, **H-Note 794** (1997).

[31] E. Gulmez, A. Penzo, Y. Onel, *SELEX Internal Report*, **H-Note 757**(1996).

[32] P.Pogodin *et al SELEX Internal Report*, **H-Note 788** (1997).

[33] S. Konigsman, S. Masciocchi, K. Vorwalter, *SELEX Internal Report*, **H-Note 661** (1994).

[34] G. Dirkes, U. Dersch, I. Eschrich, H. Krueger, J. Simon, K. Vorwalter, *SELEX Internal Report*, **H-Note 818** (1998).

[35] V. Maleev *et al.*, *SELEX Internal Report*, **H-Note 747** (1997).

[36] T. Lungov, L. Emediato, *SELEX Internal Report*, **H-Note 779** (1997).

[37] J. Engelfried *et al.*, *Nucl. Instr. and Meth.* **A433**(1999) 149.

[38] J. Engelfried *et al.*, *Nucl. Instr. and Meth.* **A431**(1999) 53.

[39] R. Pordes et al., FERMILAB-CONF-94-103. Proceedings of the Conference on Computing in High Energy Physics '94, San Francisco, CA., 21-27 April 1994, 117.